UCSF

UC San Francisco Electronic Theses and Dissertations

Title

DMS-Guided Structural Biology Approaches to Durable Streptogramin A Antibiotics

Permalink

https://escholarship.org/uc/item/3qt7k0t7

Author

Pellegrino, Jenna

Publication Date

2022

Peer reviewed|Thesis/dissertation

DMS-Guided Structural Biology Approaches to Durable Streptogramin A Antibiotics

by
Jenna Pellegrino

DISSERTATION
Submitted in partial satisfaction of the requirements for degree of
DOCTOR OF PHILOSOPHY

in

Biophysics

in the

GRADUATE DIVISION
of the
UNIVERSITY OF CALIFORNIA, SAN FRANCISCO

Approved:

DocuSigned by:
James Fraser
EF2645E0B04B452...
_____
James Fraser
Chair

DocuSigned by:
Danica Galonic Fujimori
DocuSigned by:8D4D6...
_____
Danica Galonic Fujimori

Ian Seiple
9A81BC9BF36F4DC...
_____
Ian Seiple

_____

_____
Committee Members

Acknowledgements

More people than I can list are due thanks for my success in graduate school. I certainly want to thank my advisor, James Fraser, for his mentorship and guidance, both academically and professionally. I also extend my thanks to Ian Seiple and Qi Li, who both were instrumental to the initial take-off of my project, and to all my committee members for helping me carry that momentum forward. I thank D. John Lee, with whom I closely worked and gained experience in Cryo-EM, as well as David Bulkley and Glenn Gilbert in the EM facility for their continuous help, patience, and often company during collection. I thank Justin Biel for his instruction in model refinement during my early days. I also thank the members of the DMS crew, especially Willow Coyote-Maestas, Jennifer Michaud, Gabriella Estevam, and Christian Macdonald, for their advice, attention to detail, and assistance throughout my DMS project.

To the friends I've made during graduate school, I'm sincerely grateful to you all for helping me persevere through the difficult times, celebrating successful experiments with me, and making my experience at UCSF a good one. I also want to acknowledge all those with whom I've had the pleasure of rock climbing, which has brought me so much joy.

Most especially, I want to thank my parents for their constant support of me going to graduate school across the country and for their love and encouragement throughout this process. My visits back home have always provided me with the best recharge. This is for you, Mom and Dad. I couldn't have made it to where I am today without you. I love you!

DMS-Guided Structural Biology Approaches to Durable Streptogramin A Antibiotics

Jenna Pellegrino

Abstract

The growing prevalence of multidrug resistant pathogens is drastically diminishing our supply of effective antibiotics, in turn increasing the risk associated with bacterial infections. A contributing factor to this issue is how rapidly bacteria adapt to restore the resistant phenotype. Regardless of the strength of the antibiotic concoction, the capability of evolved resistance will always remain a lingering threat. This highlights an important question: How can we design antibiotics that are more resilient to evolved resistance? I have studied this question in the context of group A streptogramin (SA) analogs, antibiotics which bind the peptidyl transferase center (PTC) of the bacterial ribosome and are deactivated by resistance enzymes like VatA, which adds an acetyl group to the macrocycle and prevents ribosomal binding.

In Chapter 1, I explore how we can overcome VatA-mediated resistance by leveraging newly developed techniques in the Seiple lab that can create fully synthetic SA analogs with great diversity. Using a combination of cryogenic electron microscopy (Cryo-EM) and molecular biology techniques, we have developed a pipeline to optimize and identify new SA antibiotics that overcome resistance mediated by wild type VatA while not compromising ribosomal inhibition. Our iterative design strategy led us to identify several SA analogs that overcome resistance mediated by wild type VatA and show improved ribosomal binding. Our best performer, analog 47, was shown in a murine thigh model of infection to be 20X more effective at reducing the bacterial load of VatA-expressing *S. aureus* than flopristin, a comparative semisynthetic SA derivative. Crystallography shows that analog 47 reshuffles the binding site of VatA, which may explain the reduced k_{cat}/K_m of VatA at acetylating this analog compared to flopristin. Finally, energy calculations show that binding of 47 in the ribosome is of lower energy than in VatA.

Despite these encouraging results, it is important to remember that, given a selective pressure, bacteria will evolve to restore their ability to grow and proliferate without hindrance in the new environment. In our case, this means that treatment of analog 47 on wild type VatA-expressing bacteria would encourage the directed evolution of VatA variants that restore the ability to deactivate the new antibiotic. Therefore, in Chapter 2, I endeavor to explore the effects of single amino acid mutations in VatA on the survival of bacteria grown in the presence of our best SA analogs and their stepwise scaffolds using Deep Mutational Scanning (DMS) and Next-Generation Sequencing (NGS). Our results revealed several strong gain of function mutations in the C-terminal domain, a region distal to the active site. We hypothesize that mutations in this region, which shows poor sequence conservation to other related Vat enzymes, likely contribute to the stability and folding of VatA.

Both of these chapters highlight our efforts to improve the durability of SA antibiotics. As demonstrated in Chapter 1, success in improving SA antibiotics' performance can be further magnified by administering them with their binding partner: group B streptogramins (SB). When used together, SA and SB act synergistically and induce a bactericidal effect. In Chapter 3, I discuss recent work exploring the potential for these two antibiotics to perform click chemistry on the ribosome and form a covalently linked molecule.

Throughout my graduate career, I have also implemented Cryo-EM in various collaborations to study the interactions between analogs of other antibiotic classes and the *E. coli* ribosome. I highlight my contributions to these works in Chapter 4.

Table of Contents

List of Figures

Chapter III

Chapter IV

List of Tables

Chapter I

Synthetic group A streptogramin antibiotics that overcome Vat resistance

Contributing Authors

Qi Li[1,8], Jenna Pellegrino[2,8], D. John Lee[2], Arthur A. Tran[1], Hector A. Chaires[2], Ruoxi Wang[1], Jesslyn E. Park[2], Kaijie Ji[1], David Chow[1], Na Zhang[1,3], Axel F. Brilot[4], Justin T. Biel[2], Gydo van Zundert[5], Kenneth Borrelli[4], Dean Shinabarger[6], Cindy Wolfe[6], Beverly Murray[6], Matthew P. Jacobson[1], Estelle Mühle[7], Olivier Chesneau[7], James S. Fraser[2], Ian B. Seiple[1]

[1]Department of Pharmaceutical Chemistry, Cardiovascular Research Institute, University of California, San Francisco, San Francisco, CA, USA.

[2]Department of Bioengineering and Therapeutic Sciences, University of California, San Francisco, San Francisco, CA, USA.

[3]College of Life Science and Bioengineering, Beijing University of Technology, Beijing, China.

[4]Department of Biochemistry and Biophysics and Howard Hughes Medical Institute, University of California, San Francisco, San Francisco, USA.

[5]Schrodinger, New York, NY, USA.

[6]Micromyx, Kalamazoo, MI, USA.

[7]Collection de l'Institut Pasteur (CIP), Microbiology Department, Institut Pasteur, Paris, France.

[8]These authors contributed equally: Qi Li, Jenna Pellegrino

Abstract

Natural products serve as chemical blueprints for most antibiotics in clinical use. The evolutionary process by which these molecules arise is inherently accompanied by the co-evolution of resistance mechanisms that shorten the clinical lifetime of any given class of antibiotics[1]. Virginiamycin acetyltransferase (Vat) enzymes are resistance proteins that provide

protection against streptogramins[2], potent antibiotics against Gram-positive bacteria that inhibit the bacterial ribosome[3]. Owing to the challenge of selectively modifying the chemically complex, 23-membered macrocyclic scaffold of group A streptogramins, analogs that overcome the resistance conferred by Vat enzymes have not been previously developed[2]. Here we report the design, synthesis, and antibacterial evaluation of group A streptogramin antibiotics with extensive structural variability. Using cryo-electron microscopy and forcefield-based refinement, we characterize the binding of eight analogs to the bacterial ribosome at high resolution, revealing binding interactions that extend into the peptidyl tRNA-binding site and towards synergistic binders that occupy the nascent peptide exit tunnel. One of these analogs has excellent activity against several streptogramin-resistant strains of *Staphylococcus aureus*, exhibits decreased rates of acetylation in vitro, and is effective at lowering bacterial load in a mouse model of infection. Our results demonstrate that the combination of rational design and modular chemical synthesis can revitalize classes of antibiotics that are limited by naturally arising resistance mechanisms.

Introduction

Natural product antibiotics often have poor characteristics as therapeutic agents[1] and are subject to resistance mechanisms that have arisen through coevolution[4]. A primary method to improve natural antibiotics for human use is semisynthesis – that is, chemical modification of natural products obtained by biological production. This method has improved the pharmacological properties of many natural product classes but has achieved only limited success in overcoming resistance mechanisms[1]. Recently, advances in chemistry have enabled access to several antibiotic classes by fully synthetic routes that provide renewed methods to overcome resistance[5,6].

Streptogramin antibiotics comprise two structurally distinct groups (A and B)[3] (**Fig. 1.4a**) that act synergistically to achieve bactericidal activity in many organisms[7] by inhibiting the

bacterial ribosome[8]. Group A antibiotics bind to the peptidyl transferase center (PTC) and increase affinity for the group B component in the adjacent nascent peptide exit tunnel[9]. Resistance to the A component mediates high-level resistance to the combination, whereas resistance to the B component results in intermediate resistance[10]. Similar to other antibiotics that target the PTC, resistance to group A streptogramins can be mediated by the ATP-binding cassette F (ABC-F) family proteins that dislodge antibiotics[11] or by Cfr methylases that methylate A2503 of the 23S rRNA to sterically block binding[12]. A specific resistance mechanism for group A streptogramins is deactivation by virginiamycin acetyltransferases (Vats)[2]. These proteins acetylate the C14 alcohol, resulting in steric interference and disruption of a crucial hydrogen bond. The combination of *vat*(A) and *vgb*(A) genes (which deactivate the B component) is the most clinically relevant streptogramin-resistance genotype in *S. aureus* in France, where streptogramins (under the trade name Pyostacine) are used orally for skin and soft tissue infections[13,14] as well as bone and joint infections[15]. Semisynthesis has improved water solubility (for example, Synercid[16]) and increased potency (for example, NXL-103[17]), but methods to overcome resistance to the class have yet to be discovered. Fully synthetic routes to group A streptogramins have been previously developed[18–28], but these routes have not been applied to the synthesis of new analogs. Here we report optimization of our initially reported route[18] and its application to the synthesis of analogs designed to overcome streptogramin resistance.

Results

Structure-guided rational design

We hypothesized that group A streptogramins could be engineered to avoid Vat acetylation while maintaining or improving ribosomal binding (**Fig. 1.4**). We selected the natural product virginiamycin M2 (VM2) as our parent scaffold owing to its ability to be converted to more active analogs by C16 fluorination (for example, flopristin, 4)[17]. To guide analog design

3

(maintaining ribosomal activity while overcoming Vat binding), we obtained a 2.5-Å resolution cryogenic electron microscopy (Cryo-EM) structure of fully synthetic VM2 bound to the Escherichia coli 50S ribosome. Both the quality of the density, enabled by the advantageous properties of the ribosome as a Cryo-EM sample, and the model, enabled by forcefield-guided refinement[29,30], facilitated our analog design. We found that the binding determinants agreed with co-crystallographic data for other related group A streptogramins bound to bacterial[9,31,32] and archeal[33,34] ribosomes.

In the ribosome, the C3 isopropyl group on VM2 participates in hydrophobic interactions with the face of U2585 but otherwise lacks binding interactions and projects towards the tRNA P-site, which suggests that C3 modifications would be tolerated. Similarly, the C4 methyl group and the C6 proton do not appear to make binding interactions and are angled towards the group B streptogramin-binding site in the exit tunnel. By contrast, mutagenesis and crystallography of the resistance enzyme VatA identified key interactions between these groups (C3 isopropyl, C4 methyl and C6 proton) and binding site residues necessary for acetylation[2]. Structural modifications of these positions might disrupt VatA binding and overcome Vat resistance, but only one semisynthetic streptogramin with modifications at one of these locations has been reported (hydrogenation of the C5–C6 alkene)[2,35]. Broader semisynthetic modifications of these positions are restricted by the lack of functional groups for chemoselective activation.

Modular synthesis of structural analogs

To directly test the hypothesis that C3 and C4 structural modifications could overcome Vat-based antibiotic resistance, we first developed a pipeline for the synthesis of group A streptogramins with unprecedented structural diversity. Our route to group A streptogramins (for example, VM2 in **Fig. 1.1a**) comprises the convergent assembly of seven simple, individually diversifiable chemical building blocks[18]. We synthesize two halves of similar complexity, join them by amide bond coupling, and accomplish macrocyclization by means of a Stille cross-

coupling reaction. Overall, the route is seven linear steps (eleven total steps) from the starting building blocks, which facilitates rapid generation of analogs. Notably, the syntheses of the halves are highly scalable. By pooling decagram quantities of each, we can rapidly synthesize analogs with modifications on the complimentary half without repeating the entire synthesis. The route depicted in **Fig. 1.1a** features technical improvements that increase yield through both the left-half sequence (31% to 40%) and the right-half sequence (18% to 28%) compared to the previous report[18].

We were readily able to prepare 18 streptogramins by building block variation, including the natural products VM2, virginiamycin M1 (VM1), madumycin I (33) and madumycin II (34) (**Fig. 1.1b**). The template synthesis of VM2 was used directly or with trivial modifications (for example, a deprotection step) in most cases to deliver analogs in good yield (10–40% overall). For certain analogs, efficiency was affected by functional group incompatibilities with the chemistry for assembly, and a modified route was required.

The incorporation of modified building blocks represents an effective approach to access new analogs, but the diversity of our library is further enhanced by incorporating functional handles for late-stage diversification. We selected C3 for diversification owing to the substantial space for expansion from this position into the tRNA P-site in the ribosome. Replacement of isobutyraldehyde (7) with para-methoxybenzyl-protected (R)- or (S)-3-hydroxy-2-methylpropanal in the left-half sequence enabled access to C3-isopropyl-modified analogs 38 and 39 (>1 g of each prepared) (**Fig. 1.1c**). Each of these alcohol-appended streptogramins was allowed to react with 17 commercially available arylisocyanates, resulting in 34 new streptogramin analogs with arylcarbamate side chains at the C3 position (40a-q and 41a-q). The alcohols in 38 and 39 also served as effective precursors for the installation of secondary amines by oxidation or reductive amination (42–44) (**Fig. 1.1d**) and for incorporation of fluorine by treatment with diethylaminosulfur trifluoride. In addition, we installed fluorine at C16 by a four-step sequence, providing the clinical candidate flopristin (4) and several fluorinated analogs (**Fig. 1.1e**).
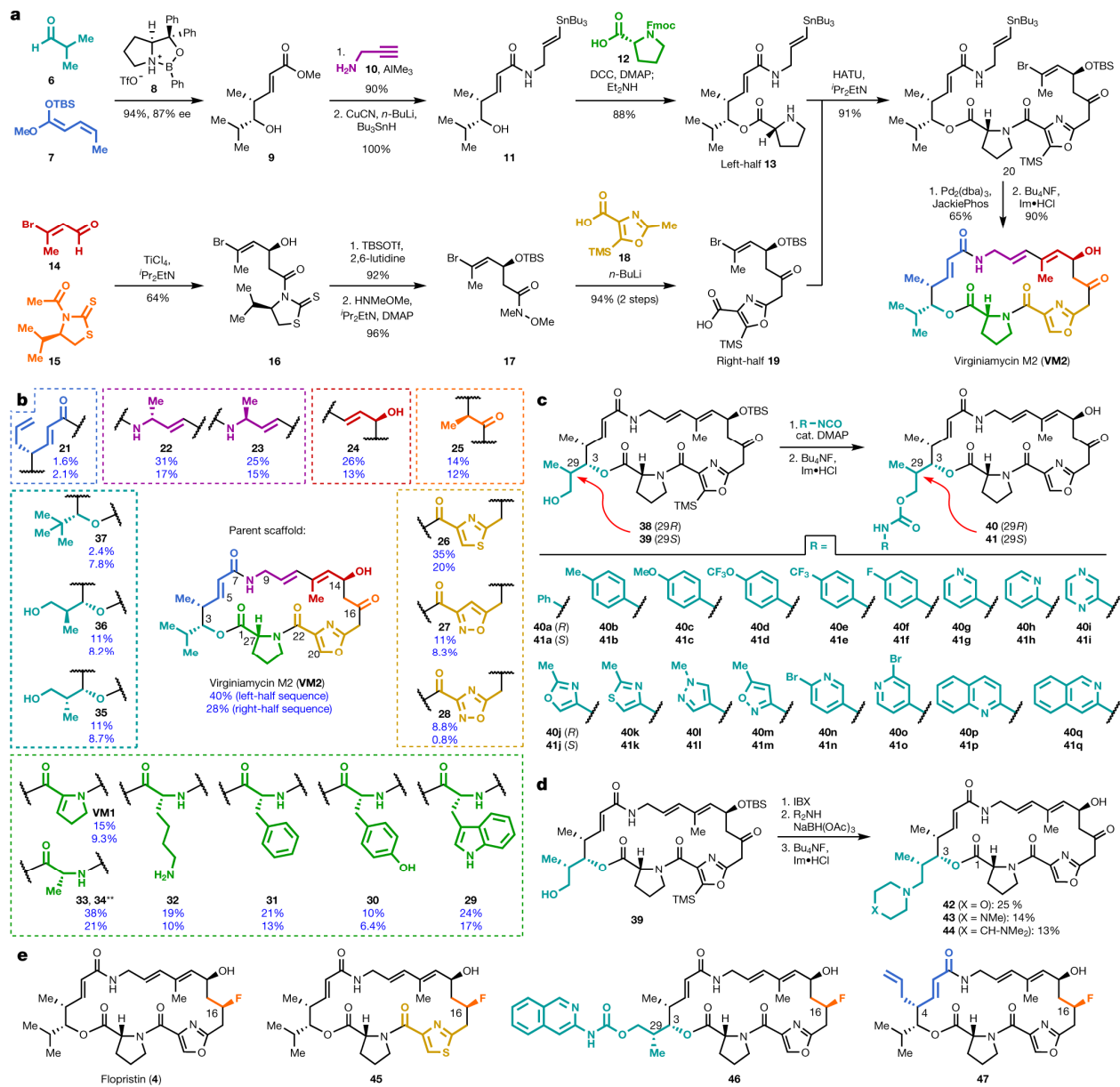
Figure 1.1. Modular synthesis enables access to more than 60 fully synthetic group A streptogramins. **(A)** Convergent route to VM2 from seven building blocks. **(B)** Eighteen group A streptogramins accessed by building block variation. The fragments displayed in the dashed boxes represent the structural variability compared to the parent scaffold (VM2). Overall yields for the synthesis of each analog for the left half sequence (top number) and for the right half sequence (bottom number) are displayed. **Instead of a ketone, madumycin II (34) contains the following substitution at C16: α-H, β-OH. **(C)** Access to 34 analogs (17 in each diastereomeric series) with C3 side-chain variability by means of carbamate formation followed by desilylation. **(D)** Synthesis of tertiary-amine-containing analogs by oxidation and reductive amination. **(E)** C16-fluorinated analogs. DCC, *N,N'*-dicyclohexylcarbodiimide; DMAP, 4-dimethylaminopyridine; HATU, hexafluorophosphate azabenzotriazole tetramethyl uronium; OTBS, O-(*tert*-butyldimethylsilyl) hydroxylamine.

In vitro and in vivo efficacy

We evaluated the activity of 62 new group A streptogramin analogs (**Fig. 1.5**), four natural products, and the first fully synthetic sample of flopristin (4) against a panel of 20 pathogens (**Fig. 1.2a, Fig. 1.6, Fig. 1.7**), including three strains with known mechanisms of streptogramin resistance (VatA and Cfr in *S. aureus*, and ABC-F in Enterococcus faecalis). We also measured in vitro ribosomal translation inhibitory activities for selected analogs (**Fig. 1.2a**, blue bars on the right). Installation of a methyl group at C9 (23) or removal of the C12 methyl group (24) resulted in loss of activity. The latter result may provide biological rationale for the four additional biosynthetic steps required for its installation[36]. Introduction of a primary or tertiary amine (32 or 42, respectively) resulted in complete loss of activity, but notably, 42 inhibited translation in vitro as effectively as VM2. The poor cellular activity probably results from decreased entry or increased efflux, highlighting the challenge of designing antibiotics with both high on-target activity and high cellular accumulation[37]. Analogs 26, 40q, and 21 displayed equal or improved activity against wild-type and VatA *S. aureus* compared to VM2, and their C16-fluorinated homologues (45, 46, and 47) exhibited substantially improved activity. Notably, analogs 46 and 47 were 16- to 32-fold more potent against wild-type and VatA *S. aureus* than flopristin (4). Furthermore, 47 had measurable activity (32 µg ml^{-1}) against ABC-F-expressing *E. faecalis*[11,38] and Gram-negative *E. coli* (16 µg ml^{-1}), species that are highly resistant to streptogramins. These results support the hypothesis that modifications to C3 and C4 of the group A streptogramin scaffold can overcome resistance caused by Vat proteins while improving antimicrobial activity.

a

MIC (µg ml⁻¹)

Strain:	1	2	3	4	5	6	7	8	9	10	11	12	10 µM in vitro translation (relative fluorescence)
	S. aureus ATCC 29213	*S. aureus* streptogramin-resistant (VatA, VgbA)	*S. aureus* methicillin-resistant ATCC 33591	*S. aureus* macrolide-resistant (inducible ErmA)	*S. aureus* macrolide-resistant (constitutive ErmA)	*S. aureus* multidrug-resistant (cfr)	*E. faecalis* ABC-F ATCC29212	*E. faecium* ATCC 35667	*E. faecium* vancomycin-resistant (VanA)	*S. pneumoniae* ATCC 49619	*H. influenzae* ATCC 49247	*E. coli* ATCC 25922	
Non-fluorinated													
VM2	16	>64	16	32	8	>64	>64	4	8	8	16	>64	
23	>64	>64	>64	>64	>64	>64	64	>64	>64	64	>64	>64	
24	>64	>64	>64	>64	>64	>64	>64	>64	>64	64	>64	>64	
32	>64	>64	>64	>64	>64	>64	>64	>64	>64	>64	>64	>64	
42	>64	>64	>64	>64	>64	>64	>64	>64	>64	>64	>64	>64	
26	16	64	16	16	8	>64	>64	4	8	8	32	>64	
40e	8	16	8	16	8	>64	>64	8	>64	>64	>64	>64	
41q	8	>64	8	16	8	>64	>64	4	16	2	>64	>64	
40q	4	16	4	8	4	>64	>64	4	8	16	2	>64	
21	4	16	4	4	2	>64	64	2	4	8	2	>64	
Fluorinated													
Flopristin (4)	0.5	8*	0.5	1	0.5	>64	>64	0.5	2	2	0.25	32	
45	0.5	8	0.5	1	0.5	>64	>64	0.5	1	1	0.25	32	
46	2	1	0.5	0.5	0.25	>64	>64	2	2	2	1	>64	
47	0.125	0.5-1*	0.25	0.25	0.125	>64	32	0.125	0.5	1	0.25	16	
+ Streptogramin B													
VS1 alone	8	16	8	4	8	8	2	2	64	1	>64	>64	
VM1 + VS1	0.125	16	1	0.25	1	8	1	≤0.06	0.25	0.125	1	64	
Flopristin (4) + VS1	0.125	4	0.5	0.125	0.5	16	0.5	≤0.06	≤0.06	0.125	0.5	32	
46 + VS1	0.25	1	0.25	0.25	0.125	4	0.5	≤0.06	0.125	≤0.06	0.25	>64	
47 + VS1	≤0.06	1	0.5	≤0.06	0.125	4	0.25	≤0.06	≤0.06	≤0.06	0.25	16	

b

MIC (µg ml⁻¹)

Strain:	2	13	14	15	16	17	18	19
	S. aureus CIP 111304	*S. aureus* CRBIP21.17	*S. aureus* CIP 111738	*S. aureus* CRBIP21.18	*S. aureus* CRBIP21.19	*S. aureus* CIP 108540	*S. aureus* CRBIP21.24	*S. aureus* CIP 107908
Group A resistance genes:	*vat*(A)	*vat*(A)	*vat*(A) *vga*(A)	*vat*(B) *vga*(A) *vga*(B)	*vat*(B) *vga*(A) *vga*(B)	*vat*(B) *vga*(A) *vga*(B)	*vat*(B) *vga*(A) *vga*(B)	*vat*(C)
Group B resistance genes:	*vgb*(A)	*vgb*(A)	*vgb*(A)	*erm*(A)	*erm*(C)	*erm*(A) *erm*(B)	*erm*(A)	*vgb*(B)
VM2	>64	64	32–64	64	32–64	64	32	32–64
Flopristin (4)	8*	2	16	16	4	8–16	8	4
47	0.5–1*	0.5	8	4	8	8–16	8	1–2

c

log₁₀(CFU/thigh) plotted against: Infection control (2 h, 24 h); Flopristin (4) (mg kg⁻¹): 10, 20, 50, 100, 200; 47 (mg kg⁻¹): 10, 20, 50, 100, 200.

Figure 1.2. Antibiotic activity and in vivo efficacy of selected group A streptogramins. **(A)** MIC values for selected analogs against an expanded panel of pathogens. Each MIC was obtained in technical triplicate. The bars to the right display in vitro translation that occurs in the presence of 10 µM of each analog (relative to dimethylsulfoxide (DMSO)). **(B)** MIC values against clinical isolates of *S. aureus* with Vat resistance genes. Ranges of values obtained from technical replicates are displayed; asterisks indicate MIC values that were obtained in technical triplicate and biological triplicate. **(C)** A mouse thigh model of infection with *S. aureus* CIP 111304 (*n* = 5 biologically independent animals per group, with the exception of the 2-h infection control where *n* = 4 per group, examined over one experiment). Each mouse is individually plotted, the center line is the mean, and the upper and lower whiskers bound the standard deviation from the mean. For detailed statistical analysis, see **Table 1.3**. CFU, colony-forming units.

Modifications that improve the activity of the group A component may not be compatible with the B component[7]. For example, C4 extensions into the nascent peptide exit tunnel may clash with the B component. Encouragingly, the combination of C3-modified 46 and even C4-modified 47 with the group B streptogramin virginiamycin S1 (VS1) resulted in improved activity

in many strains. In many cases, growth was completely inhibited even at the lowest concentration tested (**Fig. 1.2a**). In *E. faecalis*, substantial improvements in the minimum inhibitory concentration (MIC) were observed for 46–VS1 (>64, 2 µg ml^{-1} to 0.5 µg ml^{-1}) and 47–VS1 (32, 2 µg ml^{-1} to 0.25 µg ml^{-1}). In most strains, 47–VS1 was considerably more potent than the two antibiotics linezolid and daptomycin, which are used to treat multidrug-resistant Gram-positive bacterial infections (**Fig. 1.6**). These results highlight the use of synergistic combinations of streptogramin and demonstrate that group A streptogramin analogs can facilitate improved activity of the combination.

We tested 47 against an expanded panel of clinical isolates of *S. aureus* that contain *vat* genes. *Vat* genes are often accompanied by *vga* genes, which encode ABC-class proteins that also confer resistance to group A streptogramins[13,14] (**Fig. 1.2b**). Notably, strains in this panel also contained resistance genes to several other classes of antibiotics, such as β-lactams, tetracyclines, and aminoglycosides (see the CRBIP catalogue; https://catalogue-crbip.pasteur.fr/ recherche_catalogue.xhtml). As expected, VM2 did not effectively inhibit the growth of these streptogramin-resistant strains. Flopristin (4) exhibited good-to-moderate activity (2–16 µg ml^{-1}), and 47 showed excellent-to-moderate activity (0.5–16 µg ml^{-1}). These data demonstrate that the fully synthetic, C4-modified streptogramin 47 is effective at inhibiting the growth of multidrug-resistant clinical isolates with group A streptogramin-resistance genes, often with greater effectiveness than the clinical candidate flopristin (4).

Given the promising in vitro activity of 47 against streptogramin-resistant strains, we next tested its efficacy in a mouse thigh model of infection using *S. aureus* CIP 111304 (strain 2), a strain that exhibits a high level of group A streptogramin resistance (**Fig. 1.2c**). At 10 mg kg^{-1}, compound 47 showed an approximately 10-fold reduction in bacterial load compared to the 24-h infection control ($P = 0.001$) (**Table 1.3**), which was similar to high-dose flopristin (4) (200 mg kg^{-1}). At 200 mg kg^{-1}, 47 demonstrated a roughly 100-fold reduction in bacterial load compared to the 24-h infection control ($P = 0.001$). It is especially notable that compound 47

demonstrates notable potency in this demanding model of infection, even in the absence of a synergistic group B streptogramin partner.

Mechanisms of action and resistance

In agreement with their low MIC values, 4 (half-maximal inhibitory concentration (IC_{50}) of 40 ± 10 nM (mean $\pm$ s.d.)) and 47 (IC_{50} of 70 ± 20 nM) inhibited translation more effectively than VM2 (IC_{50} of 500 ± 200 nM) in vitro (**Fig. 1.3a**). The similar IC_{50} values of 4 and 47 suggest that their MIC differences are due to factors other than improved ribosome inhibition. To quantify deactivation by VatA, we measured rates of C14 acetylation using purified VatA for 4 and 47. The approximately 2.5-fold reduction in catalytic efficiency (k_{cat}/K_m) does not linearly account for the 8-fold to 16-fold reduction in MIC values in the plasmid-mediated VatA *S. aureus* strain (strain 2) (**Fig. 1.2a–c**), but it is similar to the reduction in the MIC values of the clinical isolates of *S. aureus* (strains 13–19). Nonlinear correlation of MIC value to drug deactivation can result from the contribution of other factors such as cellular accumulation, other resistance mechanisms, and efflux[39,40]. To determine the structural contributions of 47 to a low rate of VatA acetylation, we obtained an X-ray co-crystal structure (**Fig. 1.3b**), which reveals displacement of Leu110 by 1.5 Å compared to VM1 in VatA (PDB code 4HUS[2]) due to steric clash with the C4 extension of 47.
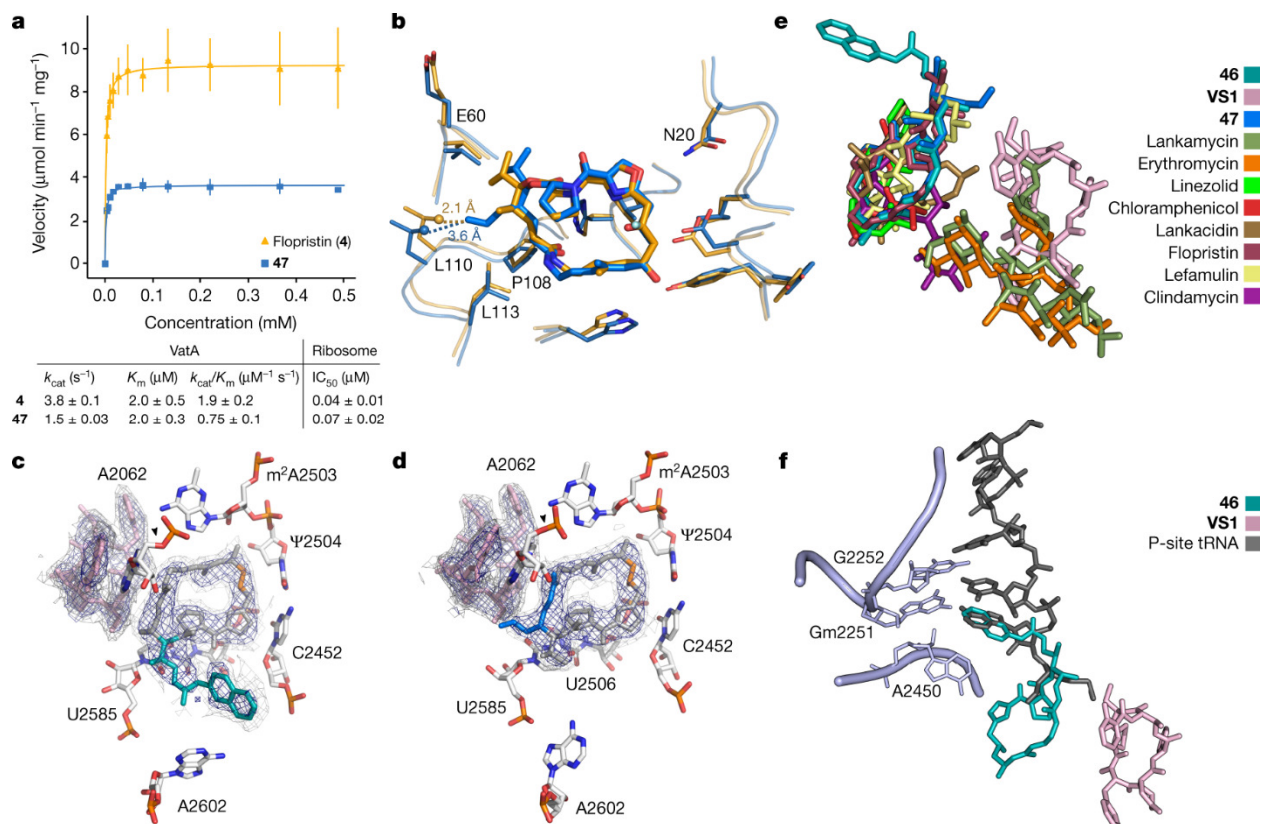
Figure 1.3. In vitro acetylation, VatA binding, and ribosome binding of highly active analogs. **(A)** Summary of VatA acetylation kinetics and in vitro inhibition of the *E. coli* ribosome by 4 and 47. Error bars denote s.d. (3 technical replicates). For detailed statistical analysis, see **Table 1.3**. **(B)** X-ray crystal structures of VM1 bound to VatA (PDB code 4HUS; 2.4 Å) and 47 bound to VatA at 3.2-Å resolution. Distances shown are measured between carbons of the C4 extension of 47 and Leu110 in the VM1-bound VatA structure (in orange dashes, 2.1 Å) and in the 47-bound VatA structure (in marine dashes, 3.6 Å). **(C)** 2.7-Å Cryo-EM Coulomb potential density map (contoured in dark blue at 4.0σ and light grey at 1.0σ) for ribosomes bound to 46 and VS1. **(D)** 2.8-Å Cryo-EM Coulomb potential density map for ribosomes bound to 47 and VS1. **(E)** Overlay of selected PTC-site antibiotics shows how the side chain of 46 and the extension of 47 occupy areas distinct to previously characterized antibiotics. **(F)** Overlay of P-site tRNA (dark grey, PDB code 1VY4) with the Cryo-EM structure of ribosome-bound 46 reveals that the side chain extends into the P-site and mimics the terminal adenosine (A2450) of the tRNA.

To explore the structural basis for antimicrobial activity, we characterized several analogs bound to the *E. coli* ribosome using Cryo-EM (**Fig. 1.3c, d, Fig. 1.8, Fig. 1.9**). The PTC is highly conserved across pathogenic species of bacteria, and the *E. coli* ribosome is an appropriate model for group A streptogramin binding in both Gram-negative and Gram-positive organisms[9]. The 2.6-Å structure of analog 47 bound to the ribosome clearly reveals the position of the C4-allyl extension, which projects towards the streptogramin B binding site and makes

contacts with A2062, U2585 and U2586 (**Fig. 1.8**). This extension also adopts a less strained conformation when ribosome-bound than when VatA-bound (calculated -2.3 kcal mol^{-1}) (**Fig. 1.10, Table 1.2**). This difference, along with protein conformational changes (**Fig. 1.3b**), could contribute to the observed differences in acetylation rates between 4 and 47. In the presence of VS1, the C4 extension adopts a strained conformation similar to its conformation in VatA but is probably stabilized by hydrophobic interactions with the B component (**Fig. 1.3d**).

Ligand strain may also have a role in the efficacy of 46. Predicted low-energy conformations of 46 position the arylcarbamate extension directly over the macrocycle (**Fig. 1.10**); however, the structures of 46 bound to the ribosome in the presence or absence of VS1 (**Fig. 1.3b**, **Fig. 1.8**) showed density for the extension in the P-site. The isoquinoline portion of the extension sits between A2602 and C2452, without making specific contacts with either. The proximity of C29 to U2585 may explain the difference in activity between the two diastereomeric series at this position (40a-q and 41a-q) (**Fig. 1.1c**). Consistent with this idea, 41q demonstrated poor density for the extension with several conformations. Notably, unlike 47, the modelled position of 46 does not clash with VatA when superposed in the crystal structure (**Fig. 1.10**). A crystal structure of 46 bound to VatA revealed an extended conformation with poor side-chain density and 10 kcal mol^{-1} higher calculated internal energies (**Fig. 1.10**, **Table 1.2**). Collectively, these results suggest that the ligands adopt distinct, strained conformations when VatA-bound than when ribosome-bound.

The bacterial PTC is a privileged antibiotic-binding site (**Fig. 1.3e**). It is notable that the arylcarbamate side chain in 46 and the allyl side chain in 47 do not considerably overlap with other ligands and that they do not preclude binding of VS1. The position of the arylcarbamate side chain in 46 extends into the P-site (**Fig. 1.3f**). By overlaying the five-terminal bases of P-site bound tRNA into the structure with 46 and VS1 bound to the catalytic center (PDB code 1VY4[41]), we discovered that the isoquinoline group in 46 overlaps substantially with the terminal adenosine that is conserved in all tRNAs. Only the non-selective inhibitor blasticidin, which

inhibits both eukaryotic and prokaryotic ribosomes, binds this deeply into the P-site by mimicking the cytosines in the CCA tail[33]. The 23-membered macrocyclic core of the group A streptogramins will probably provide a basis for selectivity for prokaryotic ribosomes that has not been achieved by tRNA mimics such as blasticidin. Further optimization of C3 side chains, guided by Cryo-EM characterization, may lead to the design of extremely potent, selective inhibitors of bacterial protein synthesis. This work highlights how Cryo-EM is contributing to the determination of structure–activity relationships[42,43].

Conclusion

By combining modular chemical synthesis, antibacterial evaluation, in vitro analysis, and high-resolution cryo-electron microscopy, we have developed a pipeline for the synthesis and optimization of group A streptogramin antibiotics. Our approach enabled the preparation of novel analogs by means of building block variation and late-stage diversification, providing valuable structure–activity relationships for the class. Modifications at two previously unexplored positions on the scaffold afforded the first group A streptogramins to overcome resistance caused by Vat enzymes. These C3- and C4-modified analogs can serve as templates for the optimization of both group A streptogramins and other PTC-binding antibiotics, potentially leading to candidates that overcome resistance caused by binding-site modifications such as methylation of A2503 by Cfr methylase. An analogy can be drawn to ketolides such as telithromycin and solithromycin, which possess biaryl side chains that enhance activity against ribosomes modified by erythromycin methyltransferases (Erm resistance)[44]. Although the emergence of other resistance mechanisms is inevitable, this approach may permit chemical adaptations to extend the clinical longevity of the streptogramin class.

Methods

MIC testing

Compounds were evaluated by Micromyx LLC (**Fig. 1.2a, Fig. 1.6, Fig. 1.7**) and at the

Collection of Institut Pasteur (**Fig. 1.2b**) for MIC activity against a variety of pathogenic bacteria,

using the broth microdilution method, as recommended by the Clinical and Laboratory

Standards Institute (CLSI). Pre-weighed vials of the test agents were stored at −20°C until

testing. On the day of the assay, the compounds were dissolved in 100% DMSO (Sigma

472301, Lot No. SHBH5551V) to a stock concentration of 6,464 µg ml^{-1}. The concentration

range tested for each of the compounds was 64–0.06 µg ml^{-1}, and each compound was tested

in triplicate. Levofloxacin was used as the quality control agent.

Animal study

The animal study was conducted at the University of North Texas Health Science Center

following UNTHSC approved (IACUC) protocol IACUC2017-049, which has been adapted from

comparable literature methods. Test articles were supplied by the Seiple Laboratory in a

randomized and blinded fashion. No statistical methods were used to predetermine sample size.

Mice

Female 5–6-week-old CD-1 mice (18–22 g) were used in the studies. The mice were

housed in groups of five with free access to food and water during the study. Mice were

obtained from Envigo Laboratories. Animals were cared for and housed in accordance with the

'Guide for Care and Use of Laboratory Animals' (National Academy Press, Washington DC,

2011). Ambient temperature was kept at 20–26°C and humidity was kept between 30% and

70%. Mice were kept on a 12 h:12 h cycle and housed according to NIH guidelines.

Pre-treatment

Mice were treated with 150 mg kg^{-1} and 100 mg kg^{-1} cyclophosphamide (Cytoxan) by the intraperitoneal route on days -4 and -1.

Infection

Inoculum was prepared in Trypticase Soy Broth (TSB) from an overnight streak plate to approximately 106 CFU ml^{-1} based on previous experimental growth curve results. Mice were infected by the intramuscular route with 0.1 ml of this adjusted inoculum.

Virulence

Micromyx provided the bacterial strain, *S. aureus* VatA strain (MMX-10227, CIP 111304), including detailed data on source, purity, in vitro growth characterization, and antibiotic susceptibility. Mice were made neutropenic by cyclophosphamide treatment before infection using standard methods. Bacterial (CFU) burden was evaluated for each group at 2 h after infection and at 24 h after infection using standard methods involving tissue thigh homogenization followed by dilution plating to permit accurate colony counts. Mice were inoculated with 5.75 log$_{10}$(CFU) of *S. aureus* MMX-10227 (with the inoculum prepared from fresh plates with 10 μg ml^{-1} VM1) and thigh samples taken at 2 h and 24 h after infection. Plate counts performed on Mueller-Hinton Agar (MHA) + 10 μg ml^{-1} virginiamycin, Brain Heart Infusion Agar (BHI) + 0.5% charcoal, and mannitol salts agar were comparable with mean bacterial thigh titres of 6.74–6.78 log$_{10}$(CFU) at 2 h and 8.20–8.61 log$_{10}$(CFU) at 24 h.

Tolerance

Test articles and a vehicle dose group were administered subcutaneously in a volume of 0.5 ml. The formulation selected for use was 10% DMSO in 25% hydroxypropyl-β-cyclodextrin (hpbCD). Mice were administered a single subcutaneous dose of each test article at 50, 100

and 200 mg kg^{-1}. For each of the dose groups in the maximum tolerated dose (MTD) determination study, three mice were used for each dose level. The use of three mice is sufficient for the determination of the MTD and this group size and proceeding in an ascending stepwise manner will allow for the use of as few animals as possible. Survival and general observations (breathing, mobility, reactions) as to the tolerability of the administered dose immediately following and for a period of time after each dose were recorded. Test articles were well tolerated over the dose range of 50, 100 and 200 mg kg^{-1} administered subcutaneously. There were no immediate adverse effects observed, and all mice appeared alert and responsive after observations at 0.5, 2, 14 and 24 h after dosing.

Efficacy study

All dosing was subcutaneous starting at 2 h after infection. Test articles were administered as a single dose to mice at 10, 20, 50, 100 and 200 mg kg^{-1}. For each of the dose groups, five mice were used at each dose level. The dosing samples were prepared fresh. Bacterial CFU/thigh at 2 h (control) and 24 h after infection were determined. Mice were euthanized by CO2 inhalation, skin reflected and thighs aseptically removed, placed in 2 ml cold sterile PBS, homogenized using a Polytron tissue homogenizer, serially diluted and plated on Mueller-Hinton Agar + 10 µg ml^{-1} virginiamycin (MHA+V).

In vitro translation assay 10-µM screen

The ability of group A streptogramin analogs to inhibit the 70S *E. coli* ribosome was first screened using the PURExpress In Vitro Protein Synthesis Kit (E6800, NEB), murine RNase inhibitor (M0314, NEB), and 6.66 ng µl^{-1} of template DNA encoding the fluorescent protein mEGFP (gift from the Cate laboratory). The volume of the reaction mixture was scaled down fivefold from the NEB protocol for a final reaction volume of 5 µl. Analogs were screened at a final concentration of 10 µM in 10% DMSO. Translation reactions were carried out in triplicate at

37°C for 1 h, then transferred to a 0°C metal block. To assist in the transfer of reactions to 96-well half-area Non-Binding Surface (NBS) microplates (Corning 3993) for final measurements, the reaction volume was increased to 50 µl by adding buffer (20 mM Tris-HCl pH 7.5, 60 mM NH4Cl, 6 mM MgCl2, 0.5 mM EDTA). Using a Cytation 5 plate reader (BioTek), translated mEGFP was excited at 485 nm; its emission was recorded at 535 nm. For comparison of analog activities across multiple initial screens, fluorescence readouts were normalized to the blank. Data were analyzed using Microsoft Excel.

In vitro translation assay for IC$_{50}$ determination

IC$_{50}$ values of group A streptogramin analogs were determined using the PURExpress Δ Ribosome Kit (E3313, NEB) for in vitro protein synthesis, 70S *E. coli* ribosomes (P0763S, NEB), murine RNase inhibitor (M0314, NEB), and 6.66 ng µl–1 of template DNA encoding the fluorescent protein mEGFP (gift from the Cate laboratory). This kit was specifically used to achieve a final ribosome concentration of 24 nM. The volume of the reaction mixture was scaled down fivefold from the NEB protocol for a final reaction volume of 5 µl. Analogs were tested in a range from 0 to 36 µM in 10% DMSO (final concentration). Translation reactions were carried out in triplicate in a 37°C water bath for 4 h, then transferred to a 0°C metal block. To assist in the transfer of reactions to 96-well half-area NBS microplates (Corning 3993) for final measurements, the reaction volume was increased to 50 µl by adding buffer (20 mM Tris-HCl pH 7.5, 60 mM NH4Cl, 6 mM MgCl2, 0.5 mM EDTA). Using a Cytation 5 plate reader (BioTek), translated mEGFP was excited at 485 nm; its emission was recorded at 535 nm. Raw data were processed and visualized using Python 2.7 and Matplotlib 2.0.2; the script is available on github. The IC$_{50}$ value was interpreted by fitting the dose response curve to the following equation, where 'top' and 'bottom' are the values of the plateaus: y = bottom + (top – bottom)/(1 + (x/IC$_{50}$)).

VatA cloning, expression and purification

This protocol was adapted from that previously described[2]. The *S. aureus* VatA sequence from residues 7 to 219 was cloned into the pET28a plasmid with an N-terminal 6xHis-tag followed by a tobacco etch virus (TEV) protease cleavage site. The plasmid was transformed into *E. coli* BL21 cells for VatA protein expression. Bacterial cultures were grown at 37°C with shaking to an OD_{600} of approximately 0.6–0.8, then induced with IPTG at a final concentration of 0.5 mM. After induction, the cultures were grown at 16°C with shaking and were collected 20–22 h later. Cells were resuspended into 50 ml of 50 mM HEPES pH 7.8, 10 mM imidazole pH 7.8, 300 mM NaCl, and EDTA-free protease inhibitor (11836170001, Roche) and then sonicated using 5 rounds of 30 s pulses with a 60 s wait period. The lysate was clarified by centrifugation at 35,000 rcf for 45 min at 4°C. Supernatant was passed over a 5 ml Ni-NTA column (HisTrap FF, GE Healthcare), washed with 50 mM HEPES pH 7.8, 20 mM imidazole pH 7.8, 300 mM NaCl, and eluted using a 50–500 mM imidazole pH 7.8 gradient. The protein was dialysed (10,000 MWCO) into 25 mM HEPES pH 7.8, 150 mM NaCl and simultaneously cleaved using 6xHis-tagged TEV protease[45] in a 1:10 ratio by weight for 48 h at 4°C. The sample was passed a second time through a Ni-NTA column (HisTrap FF, GE Healthcare), and VatA was collected in the wash. For enzymology, the sample was passed over a Superdex 200 16/600 sizing column (GE Healthcare) with 25 mM HEPES pH 7.8, 150 mM NaCl and collected in the elution. For both enzymology and crystallography, purified protein was concentrated and stored at –80°C until further use.

VatA acetylation assay

Acetylation assays were performed in 96-well clear polystyrene flat-bottom NBS plates (Corning 3641) at 100 µl of 50 mM HEPES pH 7.8, 0.5 mM 5,5′-dithiobis-(2-nitrobenzoic acid) (DTNB or Ellman's Reagent), 1 mM acetyl-CoA (AcCoA), 29 nM TEV-cleaved enzyme, and 0 to 0.4875 or 0.65 µM streptogramin A analog[2,46]. Analogs were diluted from stock solutions

prepared at 35 mM compound in 80% ethanol; the final amount of ethanol in the acetylation

reaction was 2%. All reactions were carried out in triplicate. Immediately upon adding enzyme,

the reaction plate was moved to an Epoch 2 plate reader (BioTek) and its wells read at 415 nm

for absorbance of the yellow TNB, a product of the 1:1 reaction of DTNB with the free sulfhydryl

of CoA. Plates were read at room temperature for approximately 8 min with 4 s intervals

between each reading of the same well. The quantity of CoA produced as a byproduct of

acetylation was determined relative to a CoA standard curve, prepared in duplicate, which

contained all components of the reaction solution except analog, enzyme, and AcCoA, which

itself was substituted for 0 to 0.375 mM CoA, final concentrations. Linear regions and slopes of

the progress curves were determined in Microsoft Excel using the best fit to a linear regression

model, optimizing R^2. Using the CoA standard curve, these rates were converted to VatA activity

in μmol CoA min^{-1} mg^{-1} enzyme. Kinetic information was derived by fitting the data to the

following Michaelis–Menten model using a script available on github.

VatA crystallization

Purified VatA was concentrated to 60 mg ml^{-1} in dialysis buffer (25 mM HEPES pH 7.8,

150 mM NaCl), mixed to a final 2:1 molar ratio (protein: compound) with 10 mM streptogramin

analog in 100% DMSO, and crystallized at room temperature using the hanging drop method

with a reservoir volume of 96 μl. After mixing, the samples were filtered through a 0.22-μm filter.

For the VatA-46 co-crystal structure, 100 nl of mixed sample were combined with 100 nl of 1 M

LiCl, 0.1 M BICINE pH 9, and 10% (w/v) PEG 6K from JCSG Core II (Qiagen) using mosquito

LCP (SPT Labtech). For the VatA-47 co-crystal structure, 100 nl of mixed sample were

combined with 100 nl of 0.2 M $(NH_4)_2SO_4$, 0.1 M phosphate-citrate pH 4.2, 20% (v/v) PEG 300,

and 10% glycerol from JCSG Core II (Qiagen) using mosquito LCP (SPT Labtech). Both

crystals were cryoprotected by a brief transfer into a 2 μl mixture of 75% reservoir solution and

25% glycerol.

X-ray diffraction data collection, processing, and model building

For both crystal structures, the diffraction data were collected at the Advanced Light Source (ALS, Berkeley, CA), beamline 8.3.1, at 92 K with a wavelength of 1.11583 Å using a DECTRIS PILATUS3 6M detector. Data were processed using Xia2 (v.0.6.354)[47], which used XDS (v20200131)[48] for indexing and integration and XSCALE[48] for merging. The resolution cut-off was selected automatically, using the default criteria in Xia2. Model construction was carried out using the PHENIX (v.1.17.1) suite and Coot (v.0.8.9.2) as follows. Structures were solved by molecular replacement using the 4HUR[2] VatA trimer and phenix.phaser[49]. Refinement was performed using phenix.refine with manual model building in Coot[50]. B-factors were refined individually for the VatA–47 structure and as single residue groups for VatA–46. NCS constraints were applied in the refinement of both structures based on density and consisted of three groups: chains A + E, chains B + F, and chains C + D for VatA–46. The NCS constraints for VatA–47 consisted of: chains A + F, chains B + E, and chains C + D. TLS groups were used based on those used previously for refinement of VatA[2]. Both VatA–46 and VatA–47 were refined with the OPLS3e/VSGB2.1 force field from Schrödinger as described below but using phenix.refine to obtain low energy conformations for the ligands. Data collection and refinement statistics are reported in **Table 1.4**. To obtain low energy conformations of VM1 in VatA and the *E. coli* ribosome, respectfully from 4HUS[2] and 4U25[9], the models were refined once using phenix.refine and the VM1 ligand refined with the OPLS3e/VSGB2.1 force field. Ligand energies were then evaluated by Prime with OPLS3e/VSGB2.1 (**Table 1.4**).

Cryo-EM sample preparation

For Cryo-EM analysis, purified 50S ribosomes from *E. coli* strain MRE600[51] were prepared in 50 mM HEPES pH 7.5, 150 mM potassium acetate, 6 mM magnesium acetate, and 7 mM fresh β-mercaptoethanol (BME). Inhibitor was added, mixed gently, and incubated on ice for 1 h. The final concentration of ribosomes was 100 nM; the final concentration of each

inhibitor was 60 µM. For samples prepared with two inhibitors, both were added in a 1:1 ratio. For each grid (Quantifoil holey carbon grids, C2-C14nCu30-01 or N1-C14nCu40-01, Quantifoil Micro Tools Gmbh), 3.5 µl of sample was deposited onto a freshly glow-discharged (EMS-100 Glow Discharge System, Electron Microscopy Sciences, 30 s at 15 mA) grid and incubated for 30 s at 25°C and 100% humidity. Grids were vitrified by plunge-freezing into liquid ethane[52] using a FEI Vitrobot Mark IV (ThermoFisher). To achieve optimal ice quality for collection, liquid was blotted from the grid using Whatman #1 filter paper and multiple grids for each sample were frozen with a range of different blotting times. Grids were screened using a FEI Talos Arctica electron microscope (ThermoFisher, operating at 200 kV, located at UCSF) to check ice quality and identify the optimum grids for data collection.

Cryo-EM data collection

All datasets were collected on FEI Titan Krios electron microscopes (ThermoFisher, operating at 300 kV, located at UCSF or NCCAT), with the exception of 40q, which was collected on a FEI Talos Arctica electron microscope (ThermoFisher, operating at 200 kV, located at UCSF). Automated data collection at UCSF was facilitated by SerialEM (v3.6)[53]; collection at NCCAT was via Leginon (v.3.4)[54]. The 50S with 47–VS1 bound data et was collected on a K3 (Gatan) Direct Electron Detector (DED) with a Gatan Imaging Filter (Gatan, 20 eV slit) using a nine-shot beam-image shift approach with coma compensation[55]. The 50S with 47 bound and the 50S with 46–VS1 bound data sets were collected using a four-shot beam-image shift approach with coma compensation on a K2 Summit DED (Gatan). All other datasets were collected on-axis using a K2 Summit DED (Gatan). Pixel sizes, number of images in dose-fractionated micrographs, dose rates, and defocus ranges varied slightly and are reported in **Table 1.5**. All image stacks were collected in super-resolution mode.

Cryo-EM image and data processing

Super-resolution image stacks were binned by a factor of 2, corrected for beam-induced motion, and dose-weighted using MotionCor2 (v.1.2.1)[56]. All Coulomb potential density maps were reconstructed in cisTEM (1.0.0-beta)[57] using dose-weighted micrographs. Initial CTF parameters were determined using CTFFIND4, included as part of the cisTEM package, with the resolution range between 30 and 4 Å included in the fitting. Bad micrographs (crystalline ice, poor CTF fits) were excluded from processing through visual inspection. Particles were picked in cisTEM by matching to a soft-edged disk template with a maximum particle radius of 110 Å and a characteristic particle radius of 90 Å. The number of particles picked from all micrographs and from good micrographs is found in **Table 1.5**. CisTEM refinement packages were made using a particle molecular weight of 1,800 kDa. Particles were 2D-classified into 50 classes with a mask radius of 150 Å. Classes containing the 50S ribosome were carried forward into single-class auto refinement with an outer mask radius of 125 Å and a default starting resolution of 20 Å. A filtered volume was used to make a binary mask; the volume eraser tool from UCSF Chimera (v.1.12)[58] was used to exclude the mobile L1 stalk from the mask. This mask was used in single-class manual refinement with a final high-resolution limit of either 3.50 or 3.00 Å (see **Table 1.5**). Unsharpened maps were used in model refinement and for all figures.

Cryo-EM model building and refinement with OPLS3e

We used UCSF Chimera (v.1.12) to rigid body align a high-resolution X-ray structure of the *E. coli* ribosome (PDB code 4YBB[59]) into our maps. Principle versions of the PHENIX suite used for Cryo-EM model building were 1.14, dev-3406, 1.16, and 1.17. Initially, the ligand restraints files (CIF files) were generated with phenix.eLBOW[60] using the analog's SMILES string and a 'final geometry' reference PDB of the analog that was derived from the pose of flopristin bound to the *E. coli* ribosome (PDB code 4U20[9]). These ligands were superimposed

into 4YBB based on the binding pose of flopristin in 4U20, and manual edits to the surrounding structure were performed in Coot (v.0.8.9.2).

After constructing these initial models, structures were refined using phenix.real_space_refine with the default protocol, initially with CIF restraints files from phenix.eLBOW. These resulted, however, in non-physical high energy conformations of the ligands (**Fig. 1.4, Table 1.1**). To improve the models of the ligands, we used a new version of phenix.real_space_refine interfaced with the OPLS3e/VSGB2.1 force field, a high quality force field for ligands[61]. This approach allows obtaining physics-based energies and gradients for either the whole or part of the structure without resorting to accurate manual CIF restraint generation. Standard PHENIX restraints were used for the macromolecule, while the ligand was governed by the OPLS3e/ VSGB2.1 force field. Precisely, the unliganded complex and ligand were individually prepped using phenix.ready_set and prepwizard, respectively, and subsequently recombined. The recombined complex served as input for refinement using the additional Schrödinger-dependent options use_schrodinger = True maestro_file = ligand.mae schrodinger. selection = "resname LIG", in which 'ligand.mae' describes the ligand structure in Maestro format and LIG is the residue three-letter code, and otherwise default parameters. For models with two ligands, namely 46–VS1 and 47–VS1, VS1 was prepared in the same way as the ligand described above. All refinement for 46–VS1 and 47–VS1 was carried out using PHENIX-OPLS3e/VSGB2.1. Atomic coordinates for VS1 and the companion ligand were merged into one instance in Maestro and exported to one .mae file. Both ligands were included in the Schrödinger selection for OPLS3e refinement.

The PHENIX-OPLS3e/VSGB2.1 interface works as follows: the PHENIX refinement engine spawns an external process serving as an energy server, initialized with the ligand structure present in the provided maestro_file option. When the refinement engine requests energies and gradients, the ligand's internal coordinates are written to file and read in by the external server. After updating ligand coordinates on the server side, the energy and gradients

are calculated and exchanged with the refinement engine. The refinement engine on its side updates the ligand energy and gradients contribution in its energy function using a default weight factor of 10 for the OPLS3e/VSGB2.1 energies. Refinement with the OPLS3e/VSGB2.1 force field reduced the energy for all ligands compared to the conformations refined using CIF based restraints calculated by phenix.eLBOW (**Table1.1**).

For all Cryo-EM figures, the full, unsharpened density maps and full PDB models were boxed using phenix.map_box with a selection radius of 20 Å around the ligand(s). Boxed map and model were loaded into PyMol (incentive v.2.2.3) with set normalize_ccp4_maps, off. Maps were contoured at 4σ for tight density (dark blue) and 1σ for loose density (light grey), both centered around the ligand with a carve of 1.8.

Quantum mechanical calculations

Calculations were based on the scaffold of flopristin (4) from the crystal structure bound to the ribosome[9]. Compound 46 was constructed using the LigPrep tool of Maestro (v2019-4, Schrödinger Inc.). First, the macrocycle conformation sampling method[62] was validated by comparison to the low energy pose as that of the co-crystal structure of flopristin (4). By using the thorough sampling intensity strategy, 1000 conformations of 46 were obtained, and the lowest prime energy pose with the r.m.s.d. <2A scaffold atoms of 4 as reference atoms) was regarded as the preferred conformation. Finally, the C3 side chain of this preferred conformation was further optimized using Jaguar software[63] using the B3LYP/6-31G* basis set by imposing the constraints on the scaffold atoms.

Statistical analyses

Statistical evaluation of data was carried out in Microsoft Excel as follows: mouse thigh infection model data (24-h control, 4, 47) were analyzed using a one-way ANOVA followed by a post hoc Tukey's test. MIC data (4, 47) in strain 2 (CIP 111304) were evaluated by a Mann–

Whitney *U* test. Kinetics data (4, 47) were analyzed using a two-tailed unpaired *t*-test and a

Cohen's d. All values are reported in **Table 1.3**.

Reporting summary

Further information on research design is available in the Nature Research Reporting

Summary linked to this paper.

Data availability

Models and maps generated during this study are available in the EMDB and PDB

(accessions are listed in **Tables 1.4 and 1.5**). Source data are provided with this paper.

Code availability

Forcefield-based refinement is available in PHENIX (versions 1.15 and later) using beta

features available in Schrödinger 2019-3. Python code for analyzing IVT data and VatA kinetics

data are available on github: https://github.com/fraser-lab/streptogramin.

Author Contributions

Q.L. and I.B.S. determined analogs for synthesis and designed the synthetic routes; Q.L. executed and optimized the syntheses of analogs, with assistance from A.A.T. (analogs 29–32), R.W. (analog 21), K.J. (analogs 27 and 28), and D.C. (analog 26); J.P. and D.J.L. prepared samples and collected Cryo-EM data; J.P. and A.F.B. calculated Cryo-EM reconstructions; J.P. and J.E.P. performed the VatA acetylation assay; J.P. performed the in vitro translation experiments; G.v.Z. and K.B. developed new tools for Cryo-EM model refinement; J.P., K.B.

and J.T.B. performed Cryo-EM model refinements; G.v.Z., J.P., H.A.C., N.Z. and M.P.J. determined relative energies of macrocycle confirmations; H.A.C. collected X-ray crystallographic data and performed X-ray model refinements; D.S., C.W., B.M., E.M, and O.C. designed and executed the MIC assays; Q.L., J.P., I.B.S. and J.S.F. wrote the manuscript. All authors discussed the results and commented on the manuscript.

Competing Interests

K.B. and G.v.Z. are employees of Schrodinger Inc. D.S., C.W. and B.M. are employees of Micromyx

Extended Data
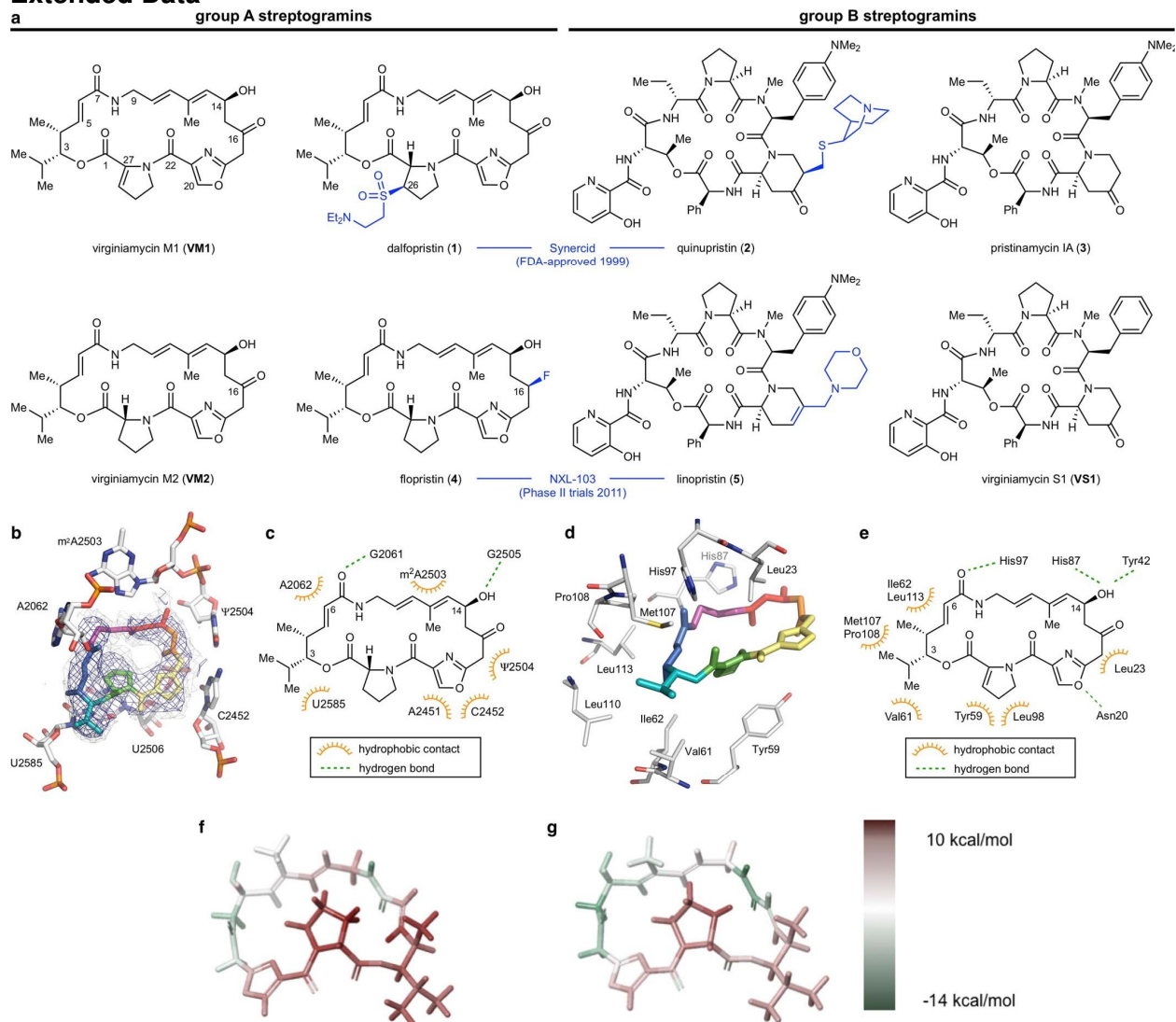
Figure 1.4. Natural and semisynthetic streptogramins and their molecular mechanisms of action and resistance. **(A)** Selected natural and semisynthetic streptogramin analogs. Modifications installed by semisynthesis are highlighted in blue. **(B)** 2.5-Å Cryo-EM structure of VM2 bound to the 50S subunit of the *E. coli* ribosome. Coulomb potential density is contoured in dark blue at 4.0σ and light grey at 1.0σ. Atom coloring of VM2 mirrors the building blocks used in its synthesis (see Fig. 2). **(C)** Binding interactions between VM2 and residues in the ribosomal binding site. **(D)** X-ray crystal structure VM1 bound to the resistance protein VatA (PDB ID: 4HUS). **(E)** Binding interactions between VM1 and VatA, highlighting the extensive hydrophobic interactions at C3–C6. Acetylation occurs at the C14 alcohol. **(F,G)** Conformational energy of VM2 showing contributions on a per atom basis when refined with standard CIF-based restraints generated by 'phenix.eLBOW' **(F)** and when refined with OPLS3e/VSGB2.1 force field **(G)**. Color indicates low strain (green, −14 kcal mol⁻¹) up to high strain (red, 10 kcal mol⁻¹), with total conformational energy of 39.5 kcal mol⁻¹ **(F)** and −88.3 **(G)**. Hydrogens were added and optimized with fixed heavy atoms for the CIF-based refined conformation using 'prepwizard'; the PHENIX-OPLS3e/VSGB2.1 refined conformation was taken as is. Energies were calculated using Prime and per atom contribution visualized using Maestro's prime energy visualization.
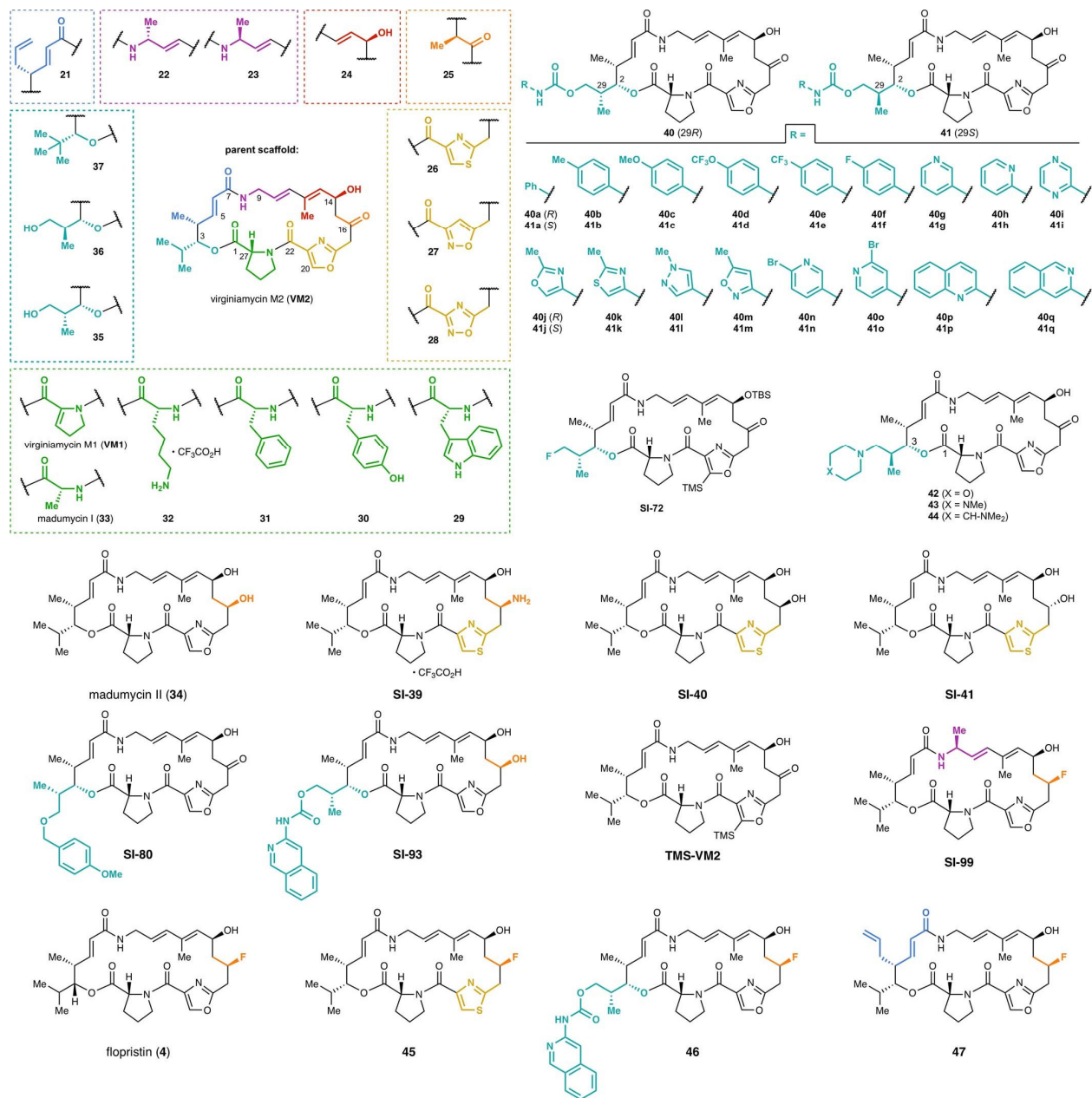
Figure 1.5. List of streptogramins tested for inhibitory activity. Fully synthetic group A streptogramins tested for inhibitory activity against 20 strains of bacteria (see Figs. 1.6, 1.7).

Minimal Inhibitory Concentration (MIC) Values (µg/mL)

Compound ID	SA Barcode	E. faecalis CLSI QC, In vivo strain MMX 0101; ATCC 29212	E. faecium ATCC isolate; VSE MMX 709; ATCC 35667	E. faecium VRE; vanA MMX 0752	S. aureus CLSI QC MMX 100; ATCC 29213	S. aureus VatA streptogramin acetyltransferase-mediated resistance CIP 111304; MMX 10227	S. aureus MRSA MMX 2001; ATCC 33591	S. aureus MLSb ErmA resistance; inducible MMX 2321; BAA-977	S. aureus MLSb ErmA resistance; constitutive MMX 3035	S. aureus Linezolid-resistant; cfr MMX 3067	S. pneumoniae PSSP; CLSI QC MMX 1195; ATCC 49619
VM2	SA0106120	>64	4	8	16	>64	16	32	8	>64	8
VM1	SA0106145	64	2	8	4	32	2	8	2	>64	8
madumycin I (33)	SA0106141	32	2	4	8	64	8	8	4	64	4
madumycin II (34)	SA0106143	>64	0.5	8	8	>64	8	16	8	>64	4
21	SA0601037	64	2	4	4	16	4	4	2	>64	8
22	SA0112091	>64	>64	>64	>64	>64	>64	>64	>64	>64	64
23	SA0112090	64	>64	>64	>64	>64	>64	>64	>64	>64	64
24	SA0110239	>64	>64	>64	>64	>64	>64	>64	>64	>64	64
25	SA0112078	64	64	>64	64	64	64	64	64	>64	64
26	SA0110141	>64	4	8	16	64	16	16	8	>64	8
27	SA05101042	>64	>64	>64	>64	>64	>64	>64	>64	>64	>64
28	SA05101054	>64	>64	>64	>64	>64	>64	>64	>64	>64	64
29	SA0202089	>64	32	32	32	64	32	32	32	>64	32
30	SA0202097	>64	>64	>64	>64	>64	>64	>64	>64	>64	64
31	SA0202061	32	32	64	64	64	64	64	64	>64	16
32	SA0202094	>64	>64	>64	>64	>64	>64	>64	>64	>64	>64
35	SA0110170	>64	>64	>64	>64	>64	>64	>64	>64	>64	64
36	SA0110026	>64	64	>64	64	>64	>64	>64	>64	>64	64
37	SA0306004	>64	32	>64	32	>64	64	64	32	>64	64
42	SA0110161	>64	>64	>64	>64	>64	>64	>64	>64	>64	>64
43	SA0110241	>64	>64	>64	>64	>64	>64	>64	>64	>64	>64
44	SA0110252	>64	>64	>64	>64	>64	>64	>64	>64	>64	>64
40a	SA0110196	>64	16	64	32	>64	32	64	16	>64	32
40b	SA0110184	>64	16	16	16	>64	16	32	16	>64	32
40c	SA0110185	>64	16	32	32	>64	16	32	16	>64	32
40d	SA0110195	>64	8	>64	16	>64	16	16	8	>64	>64
40e	SA0110193	>64	8	>64	8	16	8	16	8	>64	>64
40f	SA0110180	>64	16	16	32	>64	16	32	16	>64	32
40g	SA0110205	>64	32	64	>64	>64	>64	>64	>64	>64	32
40h	SA0110222	>64	32	64	>64	>64	>64	>64	64	>64	32
40i	SA0110215	>64	64	>64	>64	>64	>64	>64	>64	>64	64
40j	SA0110210	>64	64	64	>64	>64	>64	>64	>64	>64	64
40k	SA0110214	>64	32	64	64	>64	64	>64	64	>64	32
40l	SA0110218	>64	>64	>64	>64	>64	>64	>64	>64	>64	>64
40m	SA0110225	>64	32	64	>64	>64	64	>64	64	>64	32
40n	SA0110209	>64	16	>64	16	>64	16	>64	16	>64	16
40o	SA0110206	>64	8	16	16	>64	16	32	16	>64	8
40p	SA0110223	>64	4	16	8	32	8	16	4	>64	32
40q	SA0110224	>64	4	8	4	16	4	8	4	>64	16
41a	SA0110043	>64	16	64	32	>64	32	64	32	>64	16
41b	SA0110037	>64	16	64	32	>64	32	64	16	>64	16
41c	SA0110040	>64	16	64	32	>64	32	64	16	>64	16
41d	SA0110041	>64	8	>64	>64	>64	>64	>64	32	>64	>64
41e	SA0110044	>64	16	>64	>64	>64	>64	>64	32	>64	>64
41e	SA0111044	>64	>64	>64	>64	>64	>64	>64	>64	>64	>64
41f	SA0110036	>64	8	32	32	>64	32	>64	16	>64	16
41g	SA0110067	>64	32	>64	>64	>64	>64	>64	64	>64	32
41h	SA0110120	>64	32	64	64	>64	64	>64	32	>64	16
41i	SA0110101	>64	64	>64	>64	>64	>64	>64	>64	>64	32
41j	SA0110095	>64	32	>64	>64	>64	>64	>64	64	>64	16
41k	SA0110098	>64	16	64	64	>64	32	64	32	>64	16
41l	SA0110113	>64	64	>64	>64	>64	>64	>64	>64	>64	8
41m	SA0110115	>64	32	>64	>64	>64	>64	>64	64	>64	16
41n	SA0110082	>64	32	>64	>64	>64	>64	>64	32	>64	8
41o	SA0110081	>64	32	>64	>64	>64	>64	>64	32	>64	32
41p	SA0110117	>64	16	32	16	>64	16	32	16	>64	4
41q	SA0110118	>64	4	16	8	>64	8	16	8	>64	2
SI-39	SA0110268	>64	64	>64	>64	>64	>64	>64	>64	>64	32
SI-40	SA0110264	>64	1	4	8	>64	16	16	8	>64	2
SI-41	SA0110266	>64	>64	>64	>64	>64	>64	>64	>64	>64	>64
SI-72	SA0110273	>64	16	64	64	>64	64	64	32	>64	16
SI-80	SA0110016	32	32	64	64	64	64	64	64	64	16
SI-93	SA0111221B	>64	8	>64	16	>64	16	32	16	>64 a	8
SI-99	SA0112129	>64	>64	>64	>64	>64	>64	>64	>64	>64	>64
TMS-VM2	SA0110261	>64	64	>64	>64	>64	64	>64	64	>64	64
flopristin (4)	SA0110272	>64	0.5	2	0.5	8	0.5	1	0.5	>64	2
45	SA0110279	>64	0.5	1	0.5	8	0.5	1	0.5	>64	1
46	SA0111223	>64	2	2	2	1	0.5	0.5	0.25	>64	2
47	SA0112131	32	0.12	0.5	0.12	0.5	0.25	0.25	0.12	>64	1
VS1	SB0306015	2	2	64	8	16	8	4	8	8	1
VM1 + VS1	SAB0306016	1	≤0.06	0.25	0.12	16	12	0.25	1	8	0.12
flopristin (4) + VS1	SA0113191	0.5	≤0.06	≤0.06	0.12	4	0.5	0.12	0.5	16	0.12
46 + VS1	SAB0306017	0.5	≤0.06	0.12	0.25	1	0.25	0.25	0.12	4	≤0.06
47 + VS1	SAB0306018	0.25	≤0.06	≤0.06	≤0.06	1	0.5	≤0.06	0.12	4	≤0.06
linezolid	-	1-4	2	nt	0.12-1	nt	1	2	2	16	0.25-2
daptomycin	-	1-4	2	nt	1-4	nt	1	nt	nt	0.25	0.06-0.5

Figure 1.6. Inhibitory activity against Gram-positive organisms. MIC values for selected analogs against an expanded panel of Gram-positive pathogens.

Minimal Inhibitory Concentration (MIC) Values (µg/mL)

Compound ID	SA Barcode	*A. baumannii* In vivo strain MMX 1630; ATCC 19606	*E. coli* CLSI QC, In vivo strain MMX 102; ATCC 25922	*E. coli* TolC efflux defective MMX 121	*E. coli* permeability mutant BAS1314;IMP4213ZAB::TN10 MMX	206 *E. coli* permeability mutant; BAS2006, OMP C, OMP F	*E. coli* ΔompC768; KanR insert MMX 9658	*K. pneumoniae* ATCC isolate MMX 4972; ATCC 43816	*K. pneumoniae* MMX 8438	*P. aeruginosa* CLSI QC, In vivo strain MMX 103; ATCC 27853	*P. aeruginosa* MDR clinical isolate MMX 8799	*H. influenzae* In vivo strain MMX 1224; ATCC 49247
VM2	SA0106120	>64	>64	2	2	2	nt	>64	>64	>64	>64	16
VM1	SA0106145	>64	>64	2	0.25	1	>64	>64	>64	>64	>64	2
madumycin I (33)	SA0106141	>64	>64	2	0.25	0.5	nt	>64	>64	>64	>64	8
madumycin II (34)	SA0106143	>64	>64	2	0.5	1	nt	>64	>64	>64	>64	1
21	SA0601037	>64	>64	4	0.25	0.25	>64	>64	>64	>64	>64	2
22	SA0112091	>64	>64	8	8	8	>64	>64	>64	>64	>64	>64
23	SA0112090	>64	>64	>64	>64	>64	>64	>64	>64	>64	>64	>64
24	SA0110239	>64	>64	8	8	64	>64	>64	>64	>64	>64	>64
25	SA0112078	>64	>64	32	>64	32	>64	>64	>64	>64	>64	>64
26	SA0110141	>64	>64	2	1	1	nt	>64	>64	>64	>64	32
27	SA05101042	>64	>64	>64	>64	>64	>64	>64	>64	>64	>64	1
28	SA05101054	>64	>64	32	32	>64	>64	>64	>64	>64	>64	>64
29	SA0202089	>64	>64	16	8	32	nt	>64	>64	>64	>64	>64
30	SA0202097	>64	>64	32	32	>64	>64	>64	>64	>64	>64	>64
31	SA0202061	>64	>64	4	4	16	nt	>64	>64	>64	>64	>64
32	SA0202094	>64	>64	>64	32	>64	>64	>64	>64	>64	>64	>64
35	SA0110170	>64	>64	32	32	>64	>64	>64	>64	>64	>64	32
36	SA0110026	>64	>64	32	64	64	nt	>64	>64	>64	>64	64
37	SA0306004	>64	>64	4	4	4	nt	>64	>64	>64	>64	>64
42	SA0110161	>64	>64	>64	>64	>64	>64	>64	>64	>64	>64	>64
43	SA0110241	>64	>64	>64	>64	>64	>64	>64	>64	>64	>64	>64
44	SA0110252	>64	>64	>64	>64	>64	>64	>64	>64	>64	>64	>64
40a	SA0110196	>64	>64	2	8	32	>64	>64	>64	>64	>64	16
40b	SA0110184	>64	>64	4	2	>64	>64	>64	>64	>64	>64	16
40c	SA0110185	>64	>64	2	4	64	>64	>64	>64	>64	>64	16
40d	SA0110195	>64	>64	8	8	>64	>64	>64	>64	>64	>64	>64
40e	SA0110193	>64	>64	8	4	>64	>64	>64	>64	>64	>64	>64
40f	SA0110180	>64	>64	4	4	>64	>64	>64	>64	>64	>64	16
40g	SA0110205	>64	>64	8	16	>64	>64	>64	>64	>64	>64	32
40h	SA0110222	>64	>64	4	16	64	>64	>64	>64	>64	>64	16
40i	SA0110215	>64	>64	8	16	>64	>64	>64	>64	>64	>64	16
40j	SA0110210	>64	>64	8	8	>64	>64	>64	>64	>64	>64	16
40k	SA0110214	>64	>64	8	8	64	>64	>64	>64	>64	>64	16
40l	SA0110218	>64	>64	16	32	>64	>64	>64	>64	>64	>64	32
40m	SA0110225	>64	>64	4	8	>64	>64	>64	>64	>64	>64	16
40n	SA0110209	>64	>64	2	2	>64	>64	>64	>64	>64	>64	8
40o	SA0110206	>64	>64	2	2	16	>64	>64	>64	>64	>64	4
40p	SA0110223	>64	>64	2	2	16	>64	>64	>64	>64	>64	8
40q	SA0110224	>64	>64	1	1	8	>64	>64	>64	>64	>64	2
41a	SA0110043	>64	>64	2	8	16	nt	>64	>64	>64	>64	32
41b	SA0110037	>64	>64	4	8	16	nt	>64	>64	>64	>64	>64
41c	SA0110040	>64	>64	2	8	16	nt	>64	>64	>64	>64	16
41d	SA0110041	>64	>64	8	8	>64	nt	>64	>64	>64	>64	>64
41e	SA0110044	>64	>64	16	16	>64	nt	>64	>64	>64	>64	>64
41e	SA0111044	>64	>64	>64	>64	>64	>64	>64	>64	>64	>64	>64
41f	SA0110036	>64	>64	2	8	8	nt	>64	>64	>64	>64	>64
41g	SA0110067	>64	>64	8	32	64	nt	>64	>64	>64	>64	>64
41h	SA0110120	>64	>64	4	8	32	nt	>64	>64	>64	>64	32
41i	SA0110101	>64	>64	8	16	64	nt	>64	>64	>64	>64	64
41j	SA0110095	>64	>64	8	16	32	nt	>64	>64	>64	>64	64
41k	SA0110098	>64	>64	2	8	16	nt	>64	>64	>64	>64	32
41l	SA0110113	>64	>64	8	16	64	nt	>64	>64	>64	>64	64
41m	SA0110115	>64	>64	8	16	64	nt	>64	>64	>64	>64	64
41n	SA0110082	>64	>64	4	16	32	nt	>64	>64	>64	>64	64
41o	SA0110081	>64	>64	4	32	32	nt	>64	>64	>64	>64	>64
41p	SA0110117	>64	>64	2	4	8	nt	>64	>64	>64	>64	>64
41q	SA0110118	>64	>64	2	2	8	nt	>64	>64	>64	>64	>64
SI-39	SA0110268	>64	>64	2	2	16	>64	>64	>64	>64	>64	64
SI-40	SA0110264	>64	>64	2	1	4	>64	>64	>64	>64	>64	1
SI-41	SA0110266	>64	>64	64	16	>64	>64	>64	>64	>64	>64	64
SI-72	SA0110273	>64	>64	4	8	16	>64	>64	>64	>64	>64	8
SI-80	SA0110016	>64	>64	8	16	>64	nt	>64	>64	>64	>64	>64
SI-93	SA0111221B	>64	>64	2	8	>64	>64	>64	>64	>64	>64	4
SI-99	SA0112129	>64	>64	8	16	>64	>64	>64	>64	>64	>64	>64
TMS-VM2	SA0110261	>64	>64	64	16	>64	>64	>64	>64	>64	>64	>64
flopristin (4)	SA0110272	>64	32	1	≤0.06	0.25	64	>64	>64	>64	>64	0.25
45	SA0110279	>64	32	1	≤0.06	0.25	329	>64	>64	>64	>64	0.25
46	SA0111223	>64	>64	1	0.5	>64	>64	>64	>64	>64	>64	1
47	SA0112131	>64	16	1	≤0.06	0.25	32	>64	>64	>64	>64	0.25
VS1	SB0306015	>64	>64	8	8	>64	>64	>64	>64	>64	>64	>64
VM1 + VS1	SAB0306016	>64	64	4	≤0.06	1	64	>64	>64	>64	>64	1
flopristin (4) + VS1	SA0113191	>64	32	1	1	≤0.06	32	>64	>64	64	>64	0.5
46 + VS1	SAB0306017	64	>64	1	0.12	2	>64	>64	>64	>64	>64	0.25
47 + VS1	SAB0306018	64	16	1	≤0.06	0.5	32	64	64	64	>64	0.25

Figure 1.7. Inhibitory activity against Gram-negative organisms. MIC values for selected analogs against an expanded panel of Gram-negative pathogens.
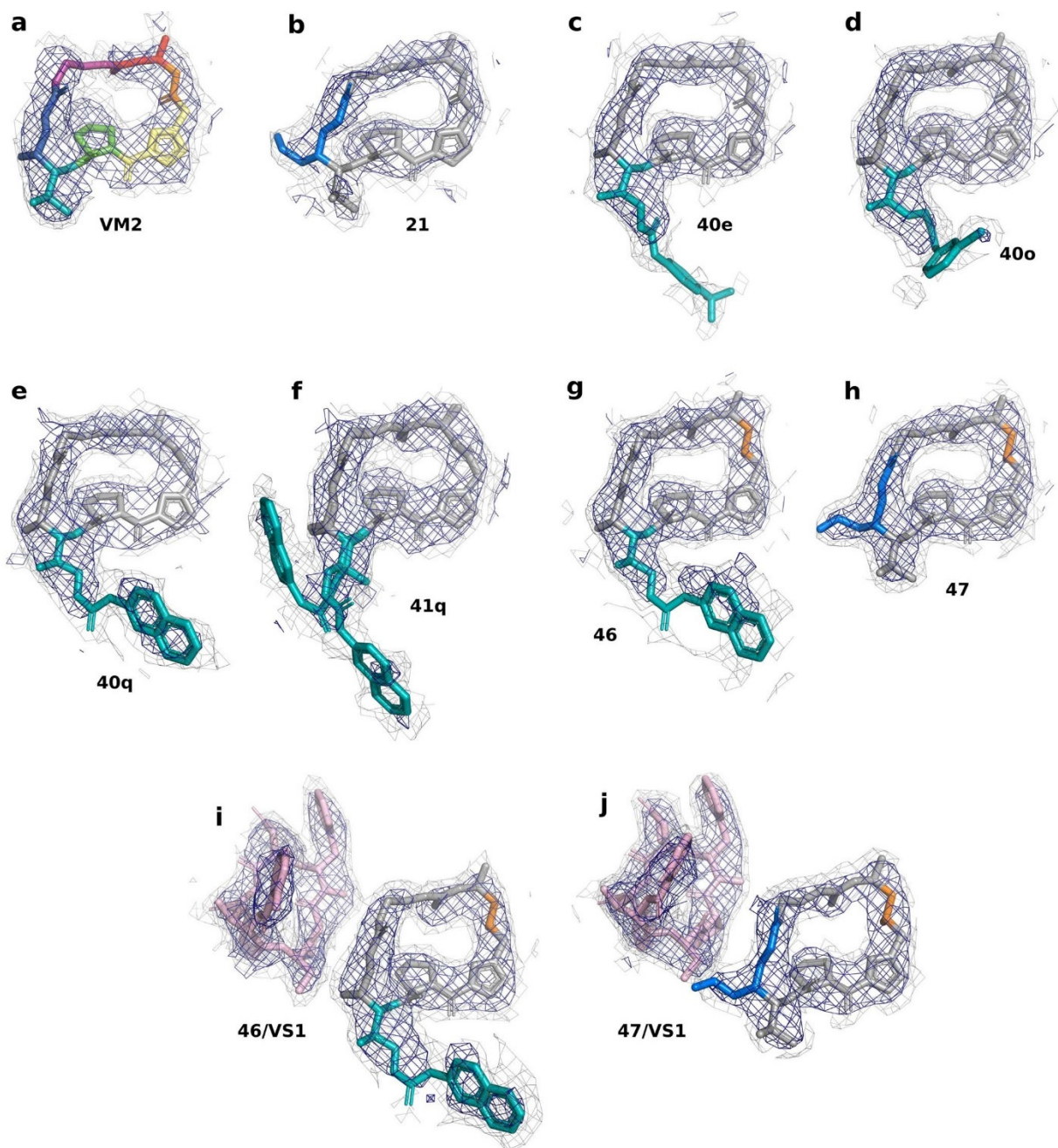
Figure 1.8. Cryo-EM density for all compounds bound to the *E. coli* ribosome. **(A)** 2.6-Å Cryo-EM structure of VM2 bound to the 50S subunit of the *E. coli* ribosome. Coulomb potential density is contoured in dark blue at 4.0σ and light grey at 1.0σ for the entire figure. **(B)** 2.8-Å Cryo-EM structure of 21 bound to the 50S subunit of the *E. coli* ribosome. **(C)** 2.8-Å Cryo-EM structure of 40e bound to the 50S subunit of the *E. coli* ribosome. **(D)** 2.5-Å Cryo-EM structure of 40o bound to the 50S subunit of the *E. coli* ribosome. **(E)** 2.8-Å Cryo-EM structure of 40q bound to the 50S subunit of the *E. coli* ribosome. **(F)** 2.6-Å Cryo-EM structure of 41q bound to the 50S subunit of the *E. coli* ribosome. **(G)** 2.5-Å Cryo-EM structure of 46 bound to the 50S subunit of the *E. coli* ribosome. **(H)** 2.5-Å Cryo-EM structure of 47 bound to the 50S subunit of the *E. coli* ribosome. **(I)** 2.7-Å Cryo-EM structure of 46/VS1 bound to the 50S subunit of the *E. coli* ribosome. **(J)** 2.8-Å Cryo-EM structure of 47/VS1 bound to the 50S subunit of the *E. coli* ribosome.
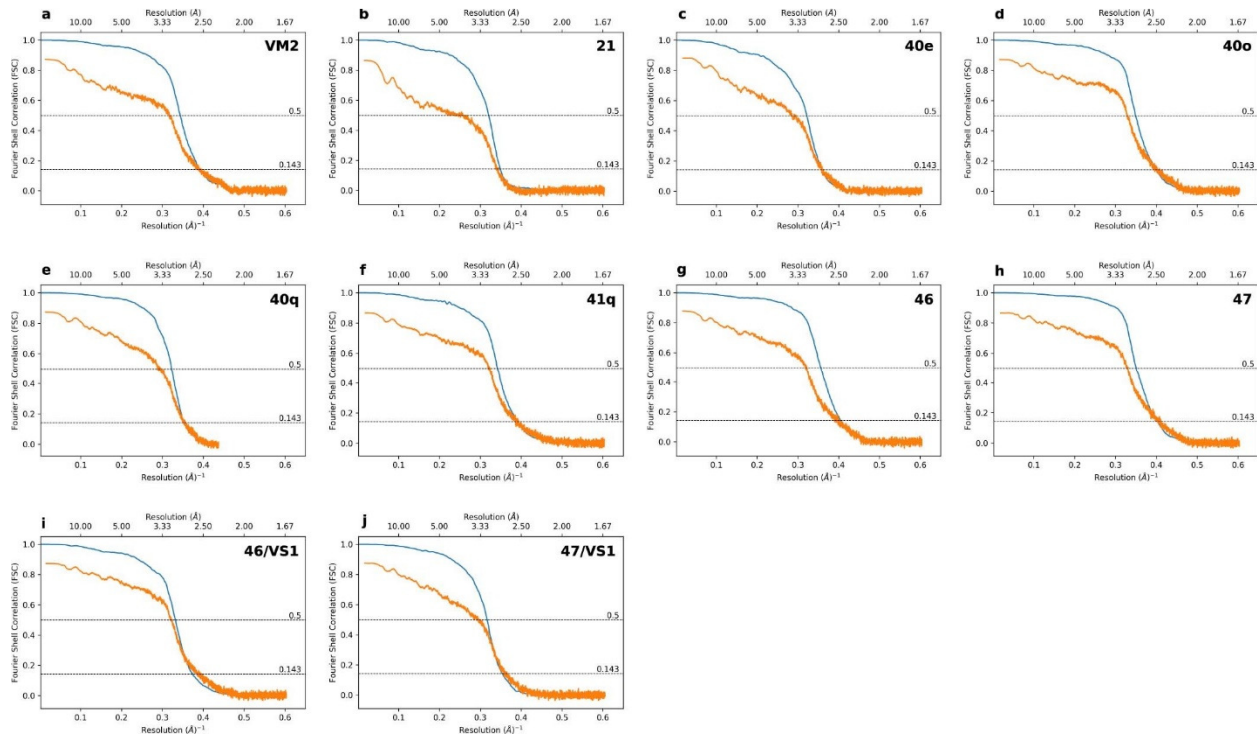
Figure 1.9. Gold standard and map to model Fourier shell correlation plots. **(A-J)** The particle Fourier shell correlation (FSC) curves for reconstructions obtained by cisTEM using a molecular mass of 1.8 MDa are shown in blue with unmasked map–model FSC curves obtained from 'phenix. mtriage' shown in orange. Dashed lines indicate FSC of 0.143 for estimating gold standard resolution and FSC of 0.5 for estimating map–model resolution.
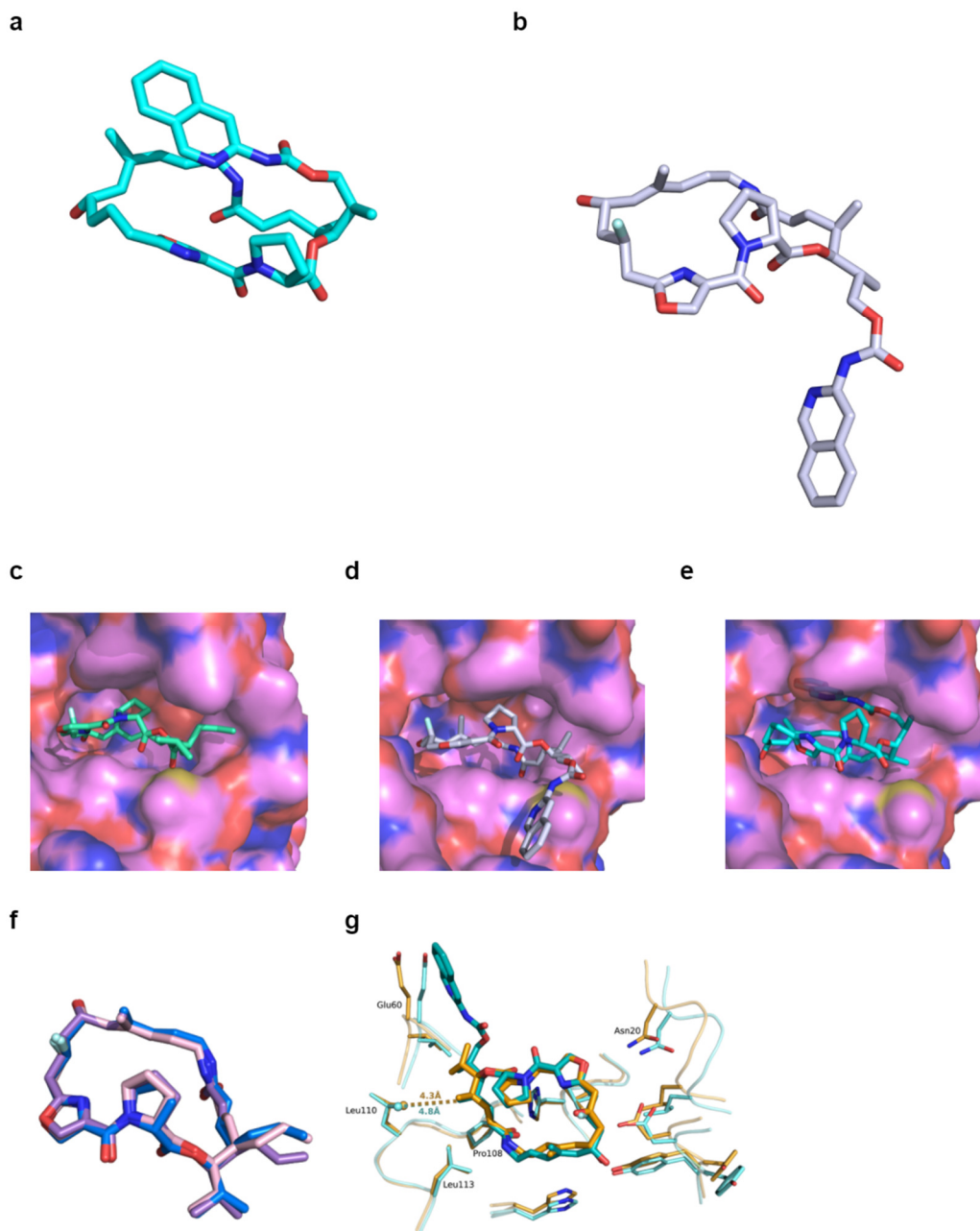
Figure 1.10. Conformations of 46 and 47 in the ribosome and in VatA. **(A)** The conformation of 46 minimized by quantum mechanical methods in low dielectric, shows how the isoquinoline side chain packs over the macrocycle. **(B)** By contrast, the ribosome-bound conformations of 46 determined by Cryo-EM show that the side chain extends away from the macrocycle due to interactions formed in the binding site. **(C)** Model of 47 in the conformation bound to the ribosome modelled into the active site of VatA (shown in surface). **(D)** Model of 46 in the conformation bound to the ribosome modelled into the active site of VatA. **(E)** Low energy model of 46 modelled into the active site of VatA. **(F)** Overlay of VatA-bound (marine), ribosome-bound (violet), and ribosome with VS1-bound (light pink) conformations of 47. **(G)** X-ray crystal structures of VM1 bound to VatA (PDB code 4HUS; 2.4 Å) and 46 bound to VatA at 2.8-Å resolution.

Table 1.1. Ligand energies by different refinement schemes. Comparative table of ligand energies when ligands are refined using 'phenix.eLBOW' generated restraints and the PHENIX force field versus when ligands are decoupled from the receptor environment and refined with PHENIX-OPLS3e/VSGB2.1. Energies were evaluated by Prime with OPLS3e/VSGB2.1.

Compound	Energy CIF refinement (kcal/mol)	Energy OPLS3e/VSGB2.1 (kcal/mol)	Delta (kcal/mol)
VM2	65.80	-93.28	-159.08
21	146.35	-91.09	-237.44
40e	702.53	-127.58	-829.11
40o	128.09	-136.21	-264.30
40q	200.53	-115.57	-316.10
41q, conf A	199.19	-118.32	-317.51
41q, conf B	284.39	-120.96	-405.35
46	84.43	-82.77	-167.20
47	107.20	-68.53	-175.73

Table 1.2. Comparative energies of ligands bound to VatA and to the ribosome. Energies of VM1, 46 and 47 bound to VatA or the *E. coli* ribosome, as evaluated by Prime with OPLS3e/VSGB2.1 after refinement with PHENIX-OPLS3e/VSGB2.1, where ligands are decoupled from the receptor environment. Included are VatA-bound VM1 from 4HUS and *E. coli* ribosome-bound VM1 from 4U25.

Compound	Ribosome	VatA chain	Energy (kcal/mol)
VM1	ASU 1		-58.27
VM1	ASU 2		-58.59
VM1		A	-58.52
47 (from 47/VS1)	X		-65.51
47	X		-68.53
47		A	-67.99
47		B	-63.40
47		C	-68.13
47		D	-67.98
47		E	-62.18
47		F	-67.66
46 (from 46/VS1)	X		-85.70
46	X		-82.77
46		A	-73.74
46		B	-79.70
46		C (conformer 1)	-67.31
46		C (conformer 2)	-65.70
46		D	-73.72
46		E	-69.07
46		F	-80.08

Table 1.3. Statistical analyses of mouse thigh in vivo data, MIC assays and VatA kinetics data. Analysis of the MIC data by Mann–Whitney U test, the mouse thigh infection model data by one-way ANOVA followed by Tukey's test, and analysis of VatA in vitro acetylation kinetics data by two-tailed unpaired t-test and Cohen's d., df, degrees of freedom, M, mean; MS, mean square; SS, sum of squares, Sign., significance.

Mann-Whitney U Test – MIC comparison of flopristin (**4**) and **47**

	N	MIC_{obs} (µg/mL)	M_{rank}	∑ rank	U	Z	p value
flopristin (**4**)	3	0.5, 0.5, 1.0	2	6	0	-1.9640	0.0248
47	3	8, 8, 8	5	15			* p < 0.05

One-way ANOVA – Murine thigh infection model comparison of flopristin (**4**), **47**, and 24-hour control

Summary	10 mg/kg			200 mg/kg		
	N	$M_{log10\ CFU/thigh}$	$SD_{log10\ CFU/thigh}$	N	$M_{log10\ CFU/thigh}$	$SD_{log10\ CFU/thigh}$
control	5	7.49	0.28	5	6.15	0.21
flopristin (**4**)	5	5.93	0.28	5	5.25	0.31
47	5	7.08	0.08	5	7.08	0.08
total	15	6.83	0.72	15	6.16	0.80

ANOVA	SS	df	MS	F_{ratio}	Sign.	SS	df	MS	F_{ratio}	Sign.
between groups	6.58	2	3.29	59.0	6.21e-7	8.35	2	4.18	86.3	7.53e-8
within groups	0.67	12	0.06			0.58	12	0.05		
total	7.25	14				8.94	14			

Tukey's Test	Q statistic	p value	Inference	Q statistic	p value	Inference
4 vs control	3.93	0.041	* p < 0.05	9.41	0.001	** p < 0.01
47 vs control	10.89	0.001	** p < 0.01	18.59	0.001	** p < 0.01
4 vs **47**	14.82	0.001	** p < 0.01	9.17	0.001	** p < 0.01

Two-tailed, unpaired t-test (Student's test) – *In vitro* acetylation of flopristin (**4**) and **47** by VatA

	N	$M_{kcat/Km}$	$SD_{kcat/Km}$	t	df	p value	Cohen's d
flopristin (**4**)	3	1.834	0.342	-4.391	4	0.012	3.585
47	3	0.765	0.247			* p < 0.05	

Table 1.4. X-Ray data collection, processing, and model refinement statistics.

	VatA-47 (6X3C)	VatA-46 (6X3J)
Wavelength	1.11583	1.11583
Resolution range	89.1 - 3.05 (3.159 - 3.05)	86.51 - 2.7 (2.797 - 2.7)
Space group	P 21 21 21	P 21 21 21
Unit cell	105.54 105.62 178.2 90 90 90	104.8 109.22 173.03 90 90 90
Total reflections	509261 (48068)	1633267 (74766)
Unique reflections	38654 (3766)	55239 (5440)
Multiplicity	13.2 (12.8)	29.6 (13.7)
Completeness (%)	99.92 (99.92)	99.96 (99.96)
Mean I/sigma(I)	6.67 (1.05)	9.41 (1.05)
Wilson B-factor	65.64	53.44
R-merge	0.3627 (1.954)	0.4085 (2.669)
R-meas	0.3773 (2.035)	0.415 (2.772)
R-pim	0.1029 (0.5651)	0.07086 (0.7417)
CC1/2	0.989 (0.575)	0.995 (0.404)
CC*	0.997 (0.855)	0.999 (0.758)
Reflections used in refinement	38637 (3766)	55232 (5440)
Reflections used for R-free	1836 (162)	2796 (285)
R-work	0.2335 (0.3299)	0.2337 (0.3325)
R-free	0.2662 (0.3169)	0.2710 (0.3361)
CC(work)	0.915 (0.714)	0.929 (0.608)
CC(free)	0.878 (0.741)	0.901 (0.571)
Number of non-hydrogen atoms	10349	10639
macromolecules	9847	9924
ligands	458	507
solvent	44	208
Protein residues	1243	1240
RMS(bonds)	0.006	0.006
RMS(angles)	0.85	0.84
Ramachandran favored (%)	95.73	97.23
Ramachandran allowed (%)	4.27	2.44
Ramachandran outliers (%)	0	0.33
Rotamer outliers (%)	0.19	0.19
Clashscore	7.31	6.54
Average B-factor	64.13	57.72
macromolecules	64.06	57.34
ligands	68.64	68.36
solvent	34.13	49.7
Number of TLS groups	18	18

Table 1.5. Cryo-EM data collection, processing, and model refinement statistics.

	VM2	21	40e
PDB code	6PCQ	6PCH	6PCS
EMDB	EMD-20304	EMD-20300	EMD-20306
EM data collection / processing			
Microscope	FEI Titan Krios	FEI Titan Krios	FEI Titan Krios
Voltage (kV)	300	300	300
Camera	Gatan K2 Summit	Gatan K2 Summit	Gatan K2 Summit
Electron exposure (e-/Å^2)	71.2	75.2	83
Defocus range (µm)	0.3 - 0.8	0.3 - 0.8	0.3 - 0.8
Pixel size (Å)	0.8283	0.8283	0.8283
Symmetry imposed	C1	C1	C1
Total number of micrographs	939	1064	848
Number of good micrographs	788	919	698
Particles picked from all micrographs	76934	95449	60400
Particles from good micrographs	64138	82551	49686
Particles used in final reconstruction	31630	23048	20644
Map resolution (Å)	2.6	2.9	2.8
FSC threshold	0.143	0.143	0.143
High resolution refinement limit (Å)	3.50	3.50	3.50
Refinement			
Initial model used (PDB code)	4YBB	4YBB	4YBB
Model resolution (Å)	3.2	3.8	3.5
FSC threshold	0.5	0.5	0.5
Map sharpening *B* factor (Å^2)	0	0	0
Model composition			
Total atoms	72125	72134	72169
Hydrogens only	0	0	0
Non-hydrogen atoms	72125	72134	72169
Protein residues	963	964	967
Nucleotide residues	3015	3015	3015
Ligands	1	1	1
B factors (Å^2), mean			
Protein	63.04	70.17	67.29
Nucleotide	78.00	85.38	83.67
Ligand	58.70	59.19	63.50
R.m.s. deviations			
Bond lengths (Å) (# >4sigma)	0.006 (1)	0.003 (8)	0.002 (0)
Bond angles (°) (# >4sigma)	0.455 (3)	0.400 (3)	0.389 (0)
Validation			
MolProbity score	1.75	1.93	1.61
Clash score	3.11	3.89	3.31
Rotamer outliers (%)	1.84	2.23	1.31
Ramachandran plot			
Favored (%)	92.95	92.02	94.15
Allowed (%)	6.94	7.88	5.75
Outliers (%)	0.11	0.11	0.10
Cβ outliers (%)	0.00	0.00	0.00
EM-Ringer Score	4.35	3.30	3.98

Table 1.5 continued

	40o	40q	41q
PDB code	6PCR	6PC8	6PCT
EMDB	EMD-20305	EMD-20299	EMD-20307
EM data collection / processing			
Microscope	FEI Titan Krios	FEI Talos Arctica	FEI Titan Krios
Voltage (kV)	300	200	300
Camera	Gatan K2 Summit	Gatan K2 Summit	Gatan K2 Summit
Electron exposure (e-/Å^2)	71.2	75	71.2
Defocus range (μm)	0.3 - 0.8	0.3 - 0.8	0.3 - 0.8
Pixel size (Å)	0.8283	1.1434	0.8283
Symmetry imposed	C1	C1	C1
Total number of micrographs	1051	895	895
Number of good micrographs	853	731	710
Particles picked from all micrographs	88694	164391	81839
Particles from good micrographs	71885	134703	64790
Particles used in final reconstruction	44462	70760	16182
Map resolution (Å)	2.5	2.8	2.6
FSC threshold	0.143	0.143	0.143
High resolution refinement limit (Å)	3.00	3.50	3.00
Refinement			
Initial model used (PDB code)	4YBB	4YBB	4YBB
Model resolution (Å)	3.0	3.4	3.1
FSC threshold	0.5	0.5	0.5
Map sharpening B factor (Å^2)	0	0	0
Model composition			
Total atoms	72166	72169	72198
Hydrogens only	0	0	0
Non-hydrogen atoms	72166	72169	72198
Protein residues	967	967	964
Nucleotide residues	3015	3015	3015
Ligands	1	1	1
B factors (Å^2), mean			
Protein	60.71	79.07	57.46
Nucleotide	75.06	95.28	71.71
Ligand	59.63	71.97	51.50
R.m.s. deviations			
Bond lengths (Å) (# >4sigma)	0.003 (8)	0.003 (8)	0.003 (1)
Bond angles (°) (# >4sigma)	0.429 (1)	0.410 (4)	0.413 (3)
Validation			
MolProbity score	1.71	1.89	1.81
Clash score	2.71	3.23	2.94
Rotamer outliers (%)	2.36	2.62	2.50
Ramachandran plot			
Favored (%)	94.57	92.69	93.59
Allowed (%)	5.22	7.21	6.30
Outliers (%)	0.21	010	0.11
Cβ outliers (%)	0.00	0.00	0.23
EM-Ringer Score	4.33	3.45	4.28

Table 1.5 continued

	46	47	46 + VS1
PDB code	6PC7	6PC6	6PC5
EMDB	EMD-20298	EMD-20297	EMD-20296
EM data collection / processing			
Microscope	FEI Titan Krios	FEI Titan Krios	FEI Titan Krios
Voltage (kV)	300	300	300
Camera	Gatan K2 Summit	Gatan K2 Summit	Gatan K2 Summit
Electron exposure (e-/Å^2)	80	79.97	79.97
Defocus range (μm)	0.3 - 0.8	0.4 - 0.8	0.4 - 0.8
Pixel size (Å)	0.8283	0.8289	0.8289
Symmetry imposed	C1	C1	C1
Total number of micrographs	921	2565	1095
Number of good micrographs	667	1756	944
Particles picked from all micrographs	83600	212341	60807
Particles from good micrographs	60607	145664	53315
Particles used in final reconstruction	36564	114964	21139
Map resolution (Å)	2.5	2.5	2.7
FSC threshold	0.143	0.143	0.143
High resolution refinement limit (Å)	3.50	3.00	3.00
Refinement			
Initial model used (PDB code)	4YBB	4YBB	4YBB
Model resolution (Å)	3.1	3.0	3.3
FSC threshold	0.5	0.5	0.5
Map sharpening B factor (Å^2)	0	0	0
Model composition			
Total atoms	72146	72127	72206
Hydrogens only	0	0	0
Non-hydrogen atoms	72146	72127	72206
Protein residues	964	963	964
Nucleotide residues	3015	3015	3015
Ligands	1	1	2
B factors (Å^2), mean			
Protein	66.15	71.00	59.62
Nucleotide	79.79	85.41	74.30
Ligand	62.11	60.54	47.35
R.m.s. deviations			
Bond lengths (Å) (# >4sigma)	0.003 (2)	0.006 (7)	0.002 (1)
Bond angles (°) (# >4sigma)	0.404(2)	0.474 (5)	0.383 (0)
Validation			
MolProbity score	1.75	1.75	1.62
Clash score	2.82	2.91	2.67
Rotamer outliers (%)	2.23	2.11	1.58
Ramachandran plot			
Favored (%)	93.70	93.48	93.80
Allowed (%)	6.20	6.41	6.09
Outliers (%)	0.11	0.11	0.11
Cβ outliers (%)	0.00	0.00	0.00
EM-Ringer Score	3.71	4.50	5.14

Table 1.5 continued

	47 + VS1
PDB code	6WYV
EMDB	EMD-21969
EM data collection / processing	
Microscope	FEI Titan Krios
Voltage (kV)	300
Camera	Gatan K3 w/ GIF, 20 eV slit
Electron exposure (e-/Å^2)	79.3
Defocus range (μm)	0.3 - 0.8
Pixel size (Å)	0.8261
Symmetry imposed	C1
Total number of micrographs	2656
Number of good micrographs	503
Particles picked from all micrographs	339838
Particles from good micrographs	63683
Particles used in final reconstruction	19484
Map resolution (Å)	2.8
FSC threshold	0.143
High resolution refinement limit (Å)	3.50
Refinement	
Initial model used (PDB code)	4YBB
Model resolution (Å)	3.4
FSC threshold	0.5
Map sharpening B factor (Å^2)	0
Model composition	
Total atoms	72194
Hydrogens only	0
Non-hydrogen atoms	72194
Protein residues	964
Nucleotide residues	3015
Ligands	2
B factors (Å^2), mean	
Protein	75.36
Nucleotide	87.56
Ligand	45.43
R.m.s. deviations	
Bond lengths (Å) (# >4sigma)	0.003 (8)
Bond angles (°) (# >4sigma)	0.407 (2)
Validation	
MolProbity score	1.78
Clash score	3.89
Rotamer outliers (%)	1.58
Ramachandran plot	
Favored (%)	92.75
Allowed (%)	7.14
Outliers (%)	0.11
Cβ outliers (%)	0.00
EM-Ringer Score	3.35

Chapter II

Streptogramin group A analogs evoke changes in the mutational sensitivity of VatA

Contributing Authors

Jenna Pellegrino[1], Jennifer M. Michaud[1], Christian B. Macdonald[1], Qi Li[2], Ian B. Seiple[2], James S. Fraser[1,3], Willow Coyote-Maestas[1,3]

[1]Department of Bioengineering and Therapeutic Sciences, University of California, San Francisco, San Francisco, CA, USA.

[2]Department of Pharmaceutical Chemistry, Cardiovascular Research Institute, University of California, San Francisco, San Francisco, CA, USA.

[3]Quantitative Biosciences Institute, University of California, San Francisco, San Francisco, CA, USA.

Abstract

Common approaches to antibiotic design are narrowly focused on overcoming current prevalent resistance mechanisms. However, a significant challenge to this approach is that bacteria, under the selective pressure of the new antibiotic, will quickly evolve mutations to restore the resistance phenotype. Exploring the mutational landscape of resistance-conferring proteins may aid in understanding the drivers of evolved resistance and developing more robust antibiotics. Here, we explore how different streptogramin group A antibiotics affect the mutational landscape of the resistance-conferring enzyme virginiamycin acetyltransferase A (VatA). By subjecting a site-saturation mutagenesis library of VatA to growth under the selective pressure of three stepwise analogs, we observed both commonalities in mutational sensitivity to each of the analogs and several strong gain of function (GOF) mutations to tryptophan in the poorly conserved C-terminal domain. Because these residues are distal to the active site, we

hypothesize that these mutations do not significantly affect enzyme catalysis. While further analyses will be required to better understand the role of tryptophan in these GOF mutations, our results suggest that stability and folding strongly influence evolved resistance in VatA.

Introduction

Antibiotic resistance is a growing global public health crisis that is rendering once easily treatable bacterial infections complex and deadly, necessitating the development of novel antibiotics that overcome resistance. Part of what makes this task so challenging is that resistance is a moving target, subject to change over generations of bacterial life. An antibiotic that circumvents a current resistance mechanism can quickly become ineffective due to the selective pressure it imposes on bacteria, which naturally suffer random DNA mutations that can be driven in the right environment to select for mutations that restore the resistance phenotype.

An approach to designing novel antibiotics that may extend their clinical longevity is to take this evolutionary phenomenon into consideration by exploring the mutational sensitivity of the resistance-conferring enzyme through techniques such as deep mutational scanning (DMS). By exploring how a library of amino acid mutations affect phenotypic characteristics, like bacterial growth in the presence of an antibiotic, it is possible to identify key residues that are either intolerant to mutation or that drive resistance. This knowledge of the enzyme's mutational landscape can in turn be leveraged during negative design of new antibiotic analogs.

Recently, we paired new approaches to the synthesis of novel streptogramin group A (SA) analogs with structural and molecular biology techniques to design and identify novel SA analogs that overcome resistance mediated by WT virginiamycin acetyltransferase A (VatA), as described in Chapter 1. This work led us to identify 47, an analog of the semi-synthetic derivative flopristin with an allyl moiety, as our most potent analog produced through our iterative design process (**Fig. 2.1**). While we were able to identify how the allyl group negatively affected deactivation of 47 by WT VatA through crystallography and kinetics, it remained

43

unknown how the extension affected VatA's mutational sensitivity. To answer this, we performed a DMS using a site-saturation library of VatA with 47 to study the effects of all possible single amino acid mutations in the enzyme on bacterial survival in the context of the analog. However, in order to keenly interpret the effects of the allyl group from these results, we also performed the DMS with stepwise analogs flopristin and VM2. Examining these data together would help deconvolute the roles that the allyl and fluorine modifications on the natural SA macrocycle play in influencing the mutational sensitivity of VatA. We propose that mutations in common across the different screens will be more commonly observed across a variety of analogs and therefore be more important to understanding how resistance evolves in VatA.
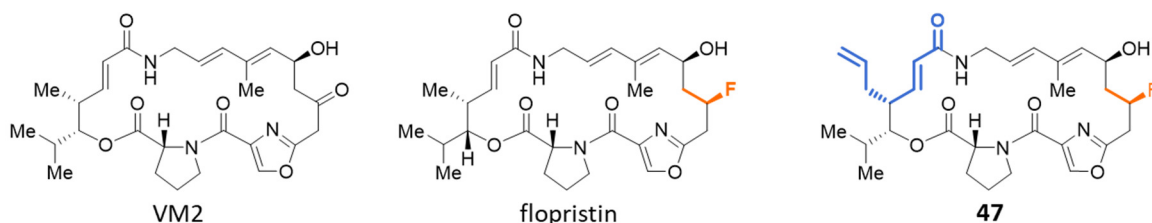
Figure 2.1. Streptogramin group A antibiotics virginiamycin M2 (VM2), flopristin, and analog 47. Regions colored on the macrocycle indicate structural modifications that differentiate the compounds.

Results and Discussion

Analog 47 demonstrates selective potential toward GOF mutations

Our previous crystal structure of WT VatA bound to 47 revealed that the allyl extension imposed significant steric bulk in the binding pocket. Residues on either side of this moiety, M107 and V61, appeared to be likely targets for evolved resistance in the enzyme due to their close proximity with the allyl group (**Fig. 2.2a**). To test this hypothesis, we mutated these residues to smaller amino acids that might better tolerate the steric bulk of the allyl. We then observed how well these mutants, M107T and V61A, improved bacterial tolerance under growth conditions in the presence of VM2 at different concentrations. If these mutations were well tolerated in the context of VM2, it could suggest their more beneficial effects in the context of 47. As a means of comparison, we also performed these growth experiments using WT VatA

and mutant L113A, a known loss of function (LOF) mutant which alters a conserved active site residue responsible for positioning SA for catalytic attack[2].

In order to more accurately test how these mutations affect bacterial survival, we needed a selection platform that could detach differential growth effects due to VatA from other competing influences, such as varying gene expression levels and antibiotic expulsion from the cell through efflux pumps in the membrane. Therefore, we performed our growth experiment using a low-copy plasmid with the constitutive β-lactamase Pbla promoter, pGDP3, and a hyperpermeable, efflux-deficient *E. coli* mutant, BW25113 ΔbamBΔtolC. This selection system was previously developed to screen for new antibiotic adjuvant candidates in the context of various resistance mechanisms, including the homolog VatD[64].

We observed that mutants M107T and V61A did improve bacterial survival in the presence of VM2, observed with the best dynamic range within the window of 1, 0.5, and 0.25 mg/L (**Fig. 2.2b**). These results revealed the potential for evolution in VatA to improve its performance at deactivating SA antibiotics as well as validated the parameters of our selection setup for future DMS experiments.
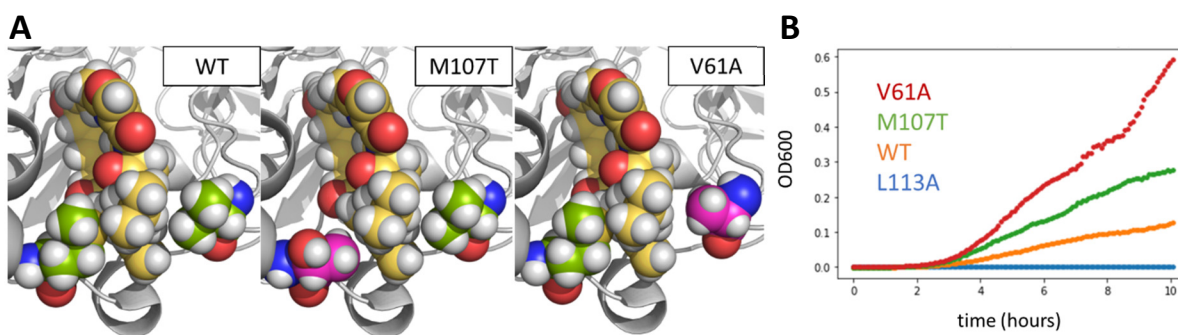
Figure 2.2. Analysis of VatA mutants. **(A)** View of the streptogramin group A binding pocket in WT VatA (left) with analog 47, yellow, bound (PDB 6X3C). Residues M107 and V61, shown in green on either side of analog 47 exhibit a strong likelihood to clash with the allyl moiety. Mutations to M107T (center) and V61A (right), colored in magenta and modeled *in silico*, alleviate steric bulk in the pocket. **(B)** Differential growth curves of ΔbamBΔtolC *E. coli*, grown with 0.5 mg/L VM2, expressing WT VatA and mutants V61A, M107T, and L113A.

Site-saturation mutagenesis and fitness of VatA under VM2 selection

Understanding the role 47's allyl group plays in perturbing the mutational landscape of VatA hinges on deconvolving the mutational effects of 47 from those of its stepwise analogs, flopristin and VM2. As VM2 serves as the natural antibiotic scaffold to these analogs, we first explored how VM2 influences evolution in VatA. To do this, we designed a site-saturation mutagenesis library of VatA comprising mutations to all 20 possible amino acids, codon-optimized for *E. coli*. This included synonyms WT mutations and early STOP codons at each position in the gene. The resulting library of 4578 mutants was subjected to selective growth conditions with the parent scaffold, VM2. Analyzing the prevalence of each mutant over the course of 12 hours of growth revealed several gain of function (GOF) mutations that confer increased resistance to VM2, including V61A (**Fig. 2.3a**). Interestingly, GOF mutations are clustered at the beginning and end of the gene, with the strongest GOF mutations appearing after residue 160, in a region not part of the active site. These observations serve as the baseline for interpreting how flopristin and 47 influence changes in VatA's mutational landscape.
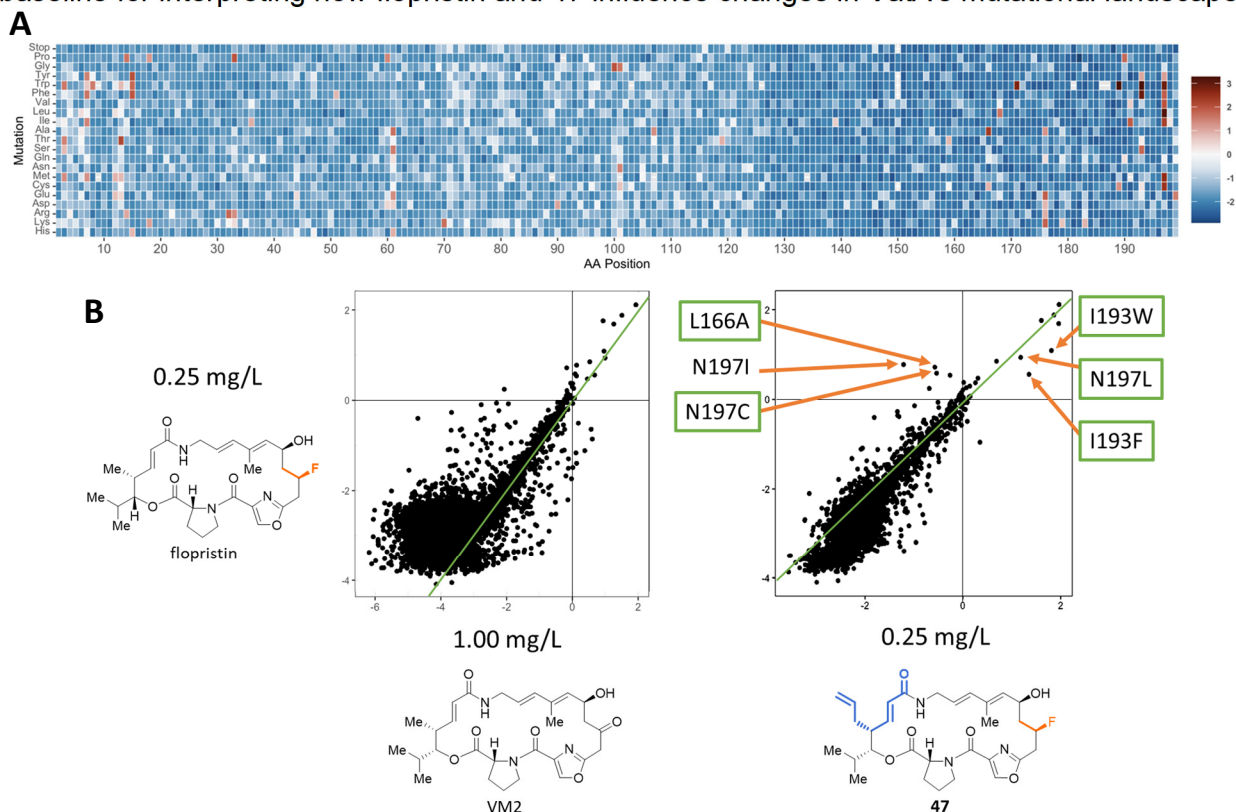
Figure 2.3. Mutational selectivity of VatA against streptogramin A analogs. **(A)** Heatmap of the DMS experiment conducted using the VatA library grown in 0.25 mg/L VM2. Mutated positions in the gene are on the *x*-axis; amino acids and the early STOP codon to which each position was mutated are on the *y*-axis. Squares, which represent an individual mutant, are colored according to the mutant's fitness score, normalized to overall counts. Blue signifies a deleterious, loss of function (LOF) mutant; red signifies a beneficial, gain of function (GOF) mutant. **(B)** Comparisons of mutants' fitness scores for VatA DMS experiments with VM2 (1 mg/L), flopristin (0.25 mg/L), and 47 (0.25 mg/L) highlight correlations in selection effect. The green line guides the eye as to where the 1:1 correlation resides. Data points for key mutants with differential signal that were further analyzed are indicated.

Flopristin and analog 47 do not strongly affect mutational sensitivity of VatA

The apparent importance of non-active-site residues in the evolved fitness of VatA for VM2 deactivation drove further curiosity to see whether flopristin and 47 would induce the same trends or more strongly promote mutations at the active site. We conducted the DMS as before, this time using flopristin and 47. As VM2 is the least potent of these three antibiotics, we drew comparisons between the selection conditions of VM2 at the highest concentration tested, 1 mg/L, and flopristin and 47 at the lowest concentration tested, 0.25 mg/L. Plotting the fitness scores of these selections against each other more easily revealed key trends in the perturbed mutational landscapes. Comparing fitness scores of the VM2 selection with the flopristin selection reveals a good 1:1 correlation, especially for shared GOF mutations (**Fig. 2.3b**). While few uniquely beneficial mutations emerge, many LOF mutations are more tolerated in the presence of flopristin. This suggests that the selective pressure imposed by the fluorine group in flopristin tilts the balance of resistance costs, making some LOF mutations less deleterious. Interestingly, comparing fitness scores of the flopristin selection with the 47 selection reveals a more pronounced 1:1 correlation. While there are a few unique GOF mutants between the pair, these data may suggest that the allyl modification on 47 does not greatly impose additional perturbations in the mutational landscape of VatA over the fluorine. Some mutants that exhibit significant differential growth signal between these two selections are L166A, I193F, I193W, N197I, N197C, and N197L. Interestingly, mutations for I193 and N197 are strongly represented, hinting that these positions play critical roles in regulating VatA evolution.

***Mutations in C-terminal alpha-helical bundle confer strong resistance in VatA***

In order to validate the results of our DMS selections, we tested 12 potential GOF mutants by repeating the individual growth experiments performed with WT VatA and mutants M107T and V61A, this time using 0.19 mg/L of flopristin. Among these 12 were the five of the mutants previously described with having significant differential growth signal between the DMS selection experiments using flopristin and analog 47. The remainder mostly consisted of GOF mutants that were common across selections with the three different SA antibiotics. Surprisingly, the majority of these potential GOF mutants were beneficial to VatA (**Fig. 2.4a**), serving to validate the credibility of our DMS screen. Notably, I193F demonstrated a LOF phenotype under these experimental conditions; it is possible this mutation, which was shown to be weakly GOF in the flopristin selection, was only supported through the competition assay in the context of the mutational library. Although it remains to be tested, I193F likely still indicates GOF activity in the context of analog 47 alone.

We observed that the top 4 fastest growing mutants exhibit OD's greater than 11-fold that of WT VatA after 6 hours of growth. Curiously, three of these bear mutations to tryptophan, the largest amino acid: L189W, I193W, and N197W. Further analysis of these mutations in the context of multiple sequence alignment with other closely related Vat enzymes reveals that most of these strong GOF mutations are found in a poorly conserved region of the enzyme in the C-terminal domain (**Fig. 2.4b**). This suggests that mutations in this domain may be generally tolerated and frequently sampled through evolution. Therefore, it may not be so surprising to find many GOF mutations in this region.
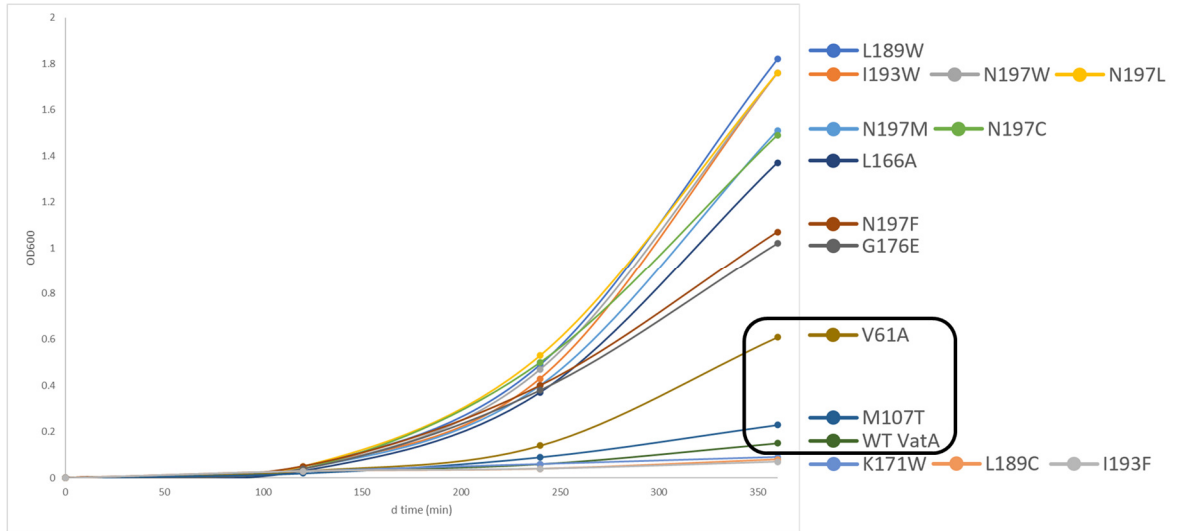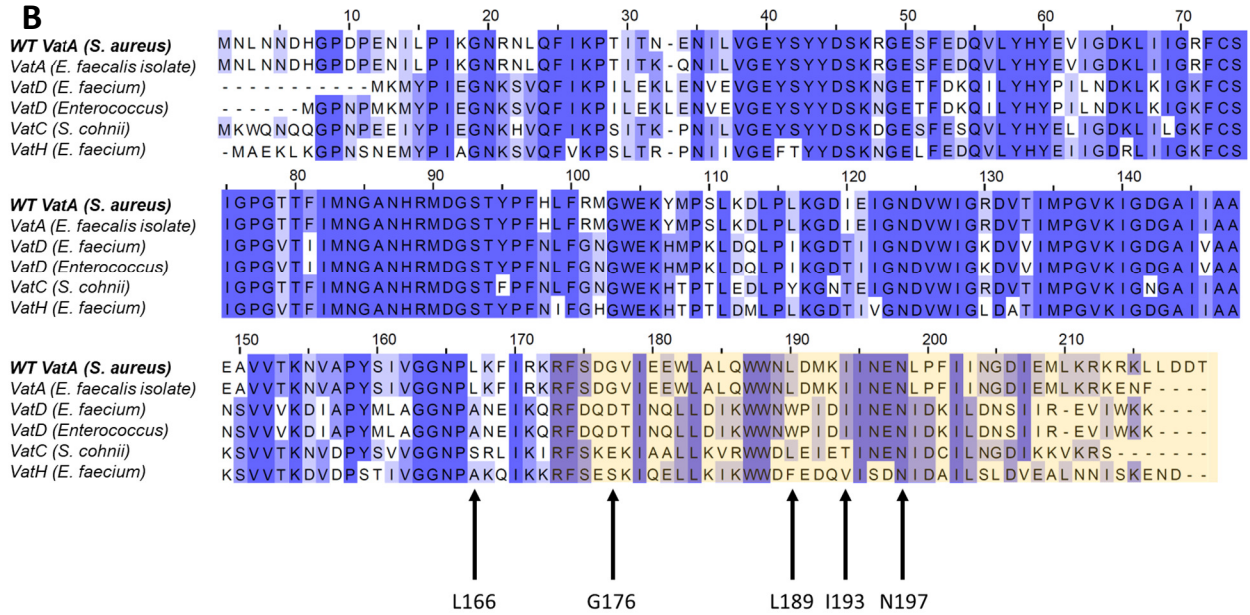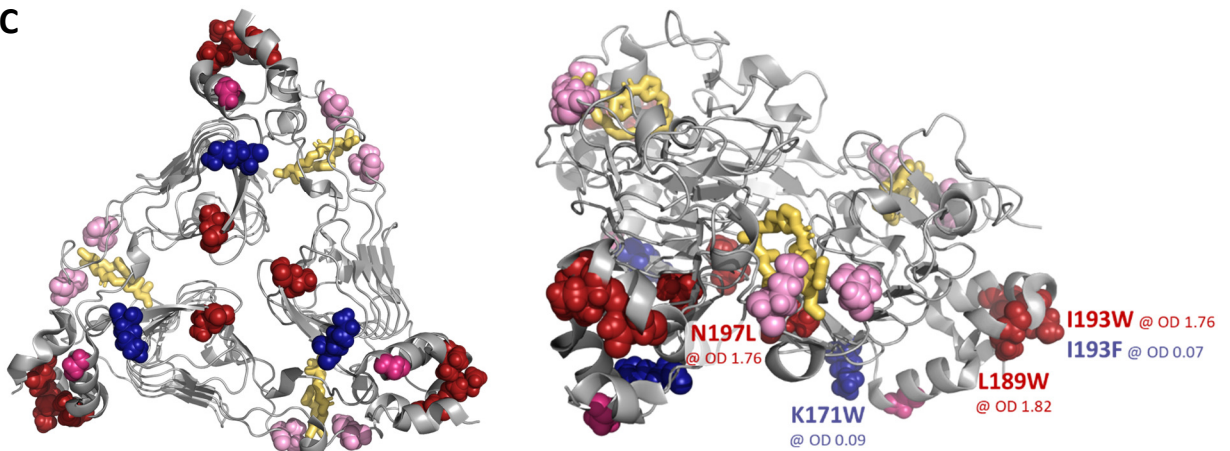
Figure 2.4. Strong GOF mutants of VatA are clustered in C-terminal domain. **(A)** Growth curves of WT VatA, M107T, V61A and 12 potential GOF mutants identified through VatA DMS. Growths were performed in 0.19 mg/L of flopristin and their OD's tracked for 6 hours. WT VatA, M107T, and V61A are designated in the box to draw attention to them for comparison. **(B)** Multiple sequence alignment of WT VatA with closely related homologs. Sequences are colored by percentage identity. Residues that are part of the C-terminal domain are highlighted in yellow. Key positions in WT VatA that lead towards GOF mutations, identified through the DMS, are indicated with arrows. **(C)** WT VatA bound to 47, in yellow (PDB 6X3C). WT residues of potential GOF mutants identified through VatA DMS are shown in spheres colored by maximum fitness effect: strong GOF (deep red), weak GOF (hot pink), very weak GOF (light pink), and LOF (dark blue). Left, a view from the bottom of VatA. Right, an angled view; key mutants of interest are denoted with their OD after 6 hours of growth.

Mapping onto the structure of WT VatA the maximum fitness score per position of each mutant analyzed in the comprehensive growth assay more clearly reveals how these residues influence VatA's structure or function. First, we observed that the strongest GOF mutations are not located in the binding site, as expected, but clustered together in an alpha-helical bundle or in a loop region near the center periphery of the enzyme (**Fig. 2.4c**). Judging by their location in the enzyme, we hypothesize that these mutations function in the stability and folding of VatA, rather than providing a catalytic effect to restore resistance. However, these observations may reflect differences in *E. coli* proteostasis rather than *S. aureus*, as experiments were conducted with *E. coli* using the sequence of VatA from *S. aureus*.

One potentiating residue with differential growth dynamics in the presences of flopristin and analog 47 is N197 (**Fig. 2.3b**). Following the common trend discussed, this residue is present in the alpha-helical bundle of the C-terminal domain. Mutant N197I, whose growth dynamics were not examined in the comprehensive growth assay, exhibited GOF activity for flopristin but LOF activity for analog 47 in the DMS experiment. In silico modeling of this mutant shows tighter packing of this hydrophobic mutant residue within the alpha-helical bundle (**Fig. 2.5**). Mutating position 197 from a polar to nonpolar amino acid could improve stability and folding in this region of the protein, supporting our hypothesis of these being the driving forces behind VatA evolution. Curiously, mutating N197 to leucine, a residue with characteristics similar to isoleucine, restores GOF activity to VatA in the presence of both flopristin and analog

47. Although it is not clear from the in silico model alone, it is possible that looser packing in this alpha-helical group may allow for more flexibility in the active site to accommodate the larger alkyl extension of 47. This conclusion, however, is not compatible with the trends observed in the strongest GOF mutants. Therefore, further characterization will be needed.
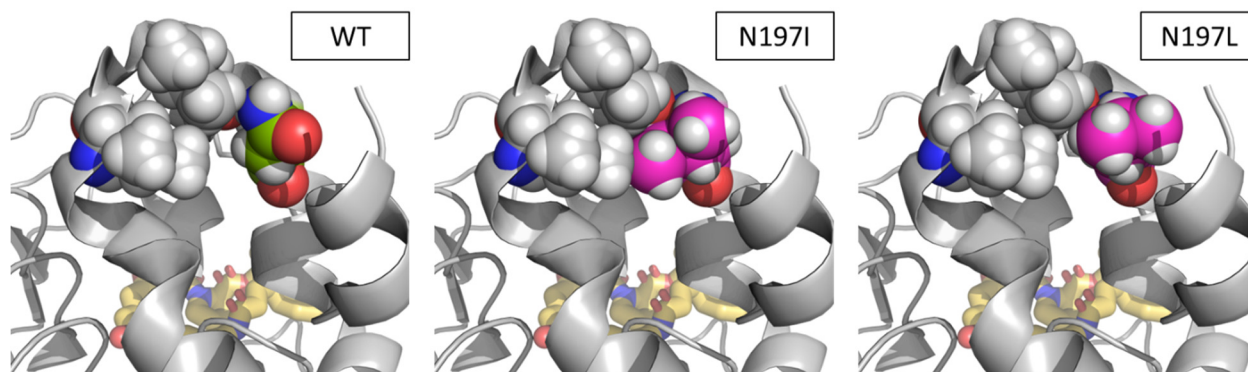

Figure 2.5. In silico modeling of N197I and N197L. Residue N197 (green) is situated in the alpha-helical bundle of the C-terminal domain near other potentiating residues I193 and L189, depicted in gray spheres. Mutant N197I (magenta, center) confers GOF activity in the presence of flopristin. Mutant N197L (magenta, right) confers GOF activity in the presence of both flopristin and analog 47. The streptogramin A analog 47 is represented in yellow to aid orientation (PDB 6X3C).

Many of the strongest GOF mutants observed had mutations to tryptophan, the least observed amino acid found in soluble proteins[65]. Commonly, tryptophan plays a role in stabilizing membrane proteins through techniques such as anchoring the protein to the lipid bilayer[66,67]. Observing that these GOF-inducing tryptophan residues are within the alpha-helical bundle of VatA, a soluble protein, we hypothesize that these mutations to tryptophan likely improve the stability and folding of VatA, although their specific roles are less obvious and require further scrutiny. It is of note that, although I193W was beneficial in the tested experimental condition, mutating I193 to phenylalanine, a smaller aromatic residue, was not tolerated. Additionally, K171W, situated at the beginning of a loop region also not near the active site, demonstrated LOF behavior. This may be due to steric bulk interfering with loop positioning and having a downstream effect, but this would need to be validated through characterization.

Normalized selective concentrations reveal unexpected potency trends

Our preliminary DMS results made clear that our original selective pressures for flopristin and analog 47 were too high and emphasized the need to choose concentrations for each analog that better normalize the selective pressure across experiments. This would make comparing datasets and drawing conclusions about the roles of different amino acids easier. To this end, we established methods to more carefully choose concentrations of the SA analogs that equalize the selective pressures. We also introduced two more analogs to our screen: SA analogs 46 and 3336 (**Fig. 2.6a**). Analog 46 is a fluorinated synthetic derivative with an arylcarbamate extension at the C3 position of the macrocycle and our second most potent analog described in Chapter 1; 3336 is a hybrid of this molecule and analog 47.

Streptogramin A compound	median concentration (mg/L)
VM2	0.32
47	0.23
3336	0.23
flopristin	0.19
46	0.13
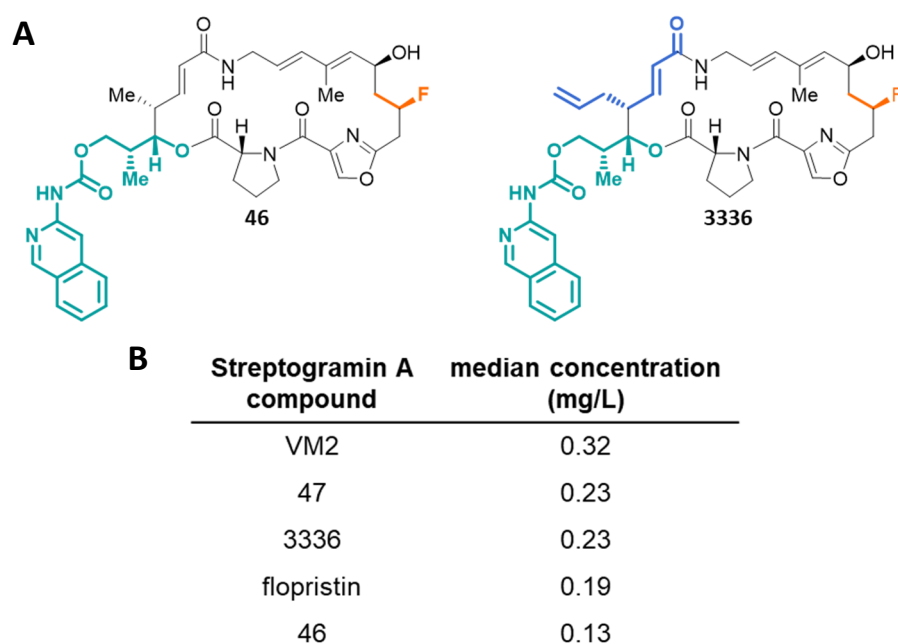
Figure 2.6. Streptogramin A compounds tested in improved DMS. **(A)** Streptogramin group A antibiotic analogs 46 and 3336. Regions colored on the macrocycle indicate structural modifications that differentiate the compounds. **(B)** Median antibiotic concentrations used for the second DMS experiments, normalized by selective pressure. The full range of concentrations tested include one concentration 1.2-fold above and below the reported median.

Surprisingly, the observed potency of our SA compounds based on growths performed with the VatA mutant library in our selection strain, *E. coli* ΔbamBΔtolC, were different than expected, considering the minimum inhibitory concentrations (MICs) of these compounds with

VatA-expressing *S. aureus*, described in Chapter 1 (**Fig. 2.6b**). While the concentrations needed to supply a selective pressure on the library decreased between VM2, flopristin, and analog 46, respectively, analogs 47 and 3336 required higher concentrations than flopristin to contribute the same selective effect. One striking commonality is that only analogs 47 and 3336, which appear to have a suppressed potency, have allyl modifications at the C4 position on the macrocycle. We questioned whether the presence of this allyl extension contributed to the apparent potency trend exclusively in the context of VatA mutants, such as during competition of the library.

To determine this, we grew the library alongside WT VatA using the five SA compounds at their normalized concentrations, and we observed the same order of potency in WT VatA (**Fig. 2.7**). Therefore, we hypothesize that the difference in apparent potencies is not a function of the VatA mutant library but rather the *E. coli* strain used for selection. Despite having a more permeable membrane deficient in efflux pumps, which theoretically should improve the access of antibiotics into these Gram-negative cells, our results highlight a significant difference in the way *E. coli* ΔbamBΔtolC cells interact with SA analogs compared to Gram-positive *S. aureus*. One potential explanation for the difference in apparent potencies observed in *E. coli* ΔbamBΔtolC is that our SA analogs could be retained within the periplasm, restraining diffusion into the cytoplasm. For instance, if the allyl extension on analogs 47 and 3336 interact strongly with an attribute of the *E. coli* ΔbamBΔtolC cells not present in *S. aureus*, it could explain their apparent decreased potency in our selection experiments. Therefore, the increased concentrations needed may not truly reflect bioavailability of the molecule within the cell. This highlights a caveat to data interpretation for our selection experiments. Determining how much of each SA analog gets into the cytoplasm of the *E. coli* ΔbamBΔtolC cells may reveal a potency trend that better correlates with the MIC results.

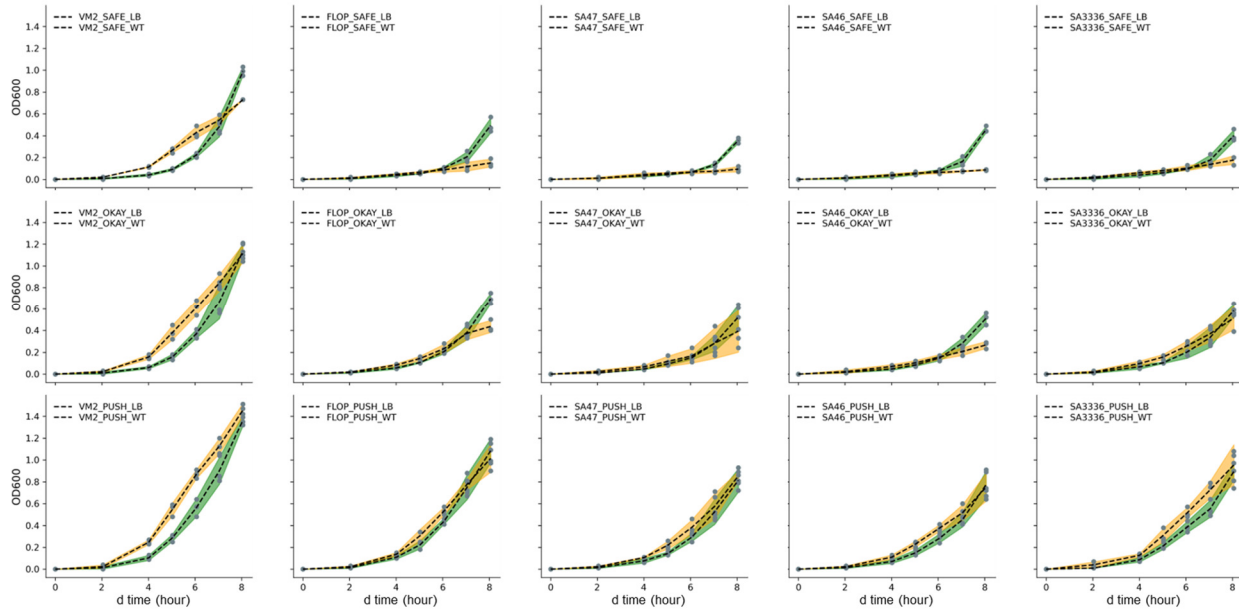**Figure 2.7**. Comparative growth curves of the VatA library (green) and WT VatA (yellow) grown with either VM2, flopristin, analog 47, analog 46, or analog 3336 at the three concentrations above the minimum selective concentration. "OKAY" represents the median concentration: going left to right, these are 0.32 mg/L for VM2, 0.19 mg/L for flopristin, 0.23 mg/L for SA analog 47, 0.13 mg/L for SA analog 46, and 0.23 mg/L for SA analog 3336. "SAFE" represents the concentration 1.2-fold above the median, and "PUSH" represents the concentration 1.2-fold below the median. Growths were performed in triplicate. Dashed lines represent the average OD_{600} at each time of recording; colored regions represent standard deviation.

Stability and function may drive evolution in VatA

Our preliminary DMS selection experiments reveal key amino acid residues in VatA at which mutations potentiate restored activity and improved cell survival in the presence of antibiotic selective pressure. While GOF mutations broadly appear to impact cell survival equally regardless of the antibiotic present, some mutants more strongly lend GOF effects in certain contexts, as observed in the differential growth signal between the flopristin and 47 selection experiments. We observed that many of these mutants that are GOF in both contexts are more strongly GOF in the presence of analog 47, such as mutations to I193 and N197. As the strongest GOF mutations we identified are not found in VatA's active site, we hypothesize that these residues do not affect catalysis but rather play roles in stability and function. These trends remain consistent across the three different antibiotic selections, despite approximating concentrations that deliver a comparable selective pressure to compare mutational sensitivities

across the antibiotics with different potencies. We expect that repeating this DMS using our identified SA analog concentrations that better normalize the selective strength across competition experiments will further increase the discernibility of these assays. Future iterations of this experiment would also benefit from pairing our selection assay with a protein abundance based assay to ascertain how much the effects on survival are attributable to the protein's altered function or stability and how much are attributable to the amount of protein expressed and tolerated by the cell. However, our results still reveal several mutants of interest that can be further characterized to explore how evolution in VatA is driven. Particularly, determining the role of tryptophan and the effects of our C-terminal mutants through experiments such as kinetics, differential scanning fluorimetry, and crystallography will be compelling next steps in this project to better understand structure-function relationships in VatA as they are related to evolved resistance to various SA antibiotics.

Methods

Saturation mutagenesis library construction

Preparation of WT vatA/pGDP3 plasmid

      The pGDP3 vector was chosen for the growth selection experiments for its previous success in studying resistance, low copy number, and constitutive promoter[64]. We obtained this plasmid harboring the vatD gene from Addgene as a colony stab. The vatD gene was exchanged for the N-term truncated WT vatA gene previously obtained from GenScript in pET-28a, as described in Chapter 1, by amplifying the vatA gene with primers p01-F and p01-R and performing a double digestion ligation assembly strategy with NcoI-HF (NEB) and NotI-HF (NEB). Next, the truncated vatA gene was amplified using primers p02-F and p02-R that readded the six missing amino acids to the amplicon. Restriction enzymes NcoI-HF and NotI-HF were used to digest both the vatA amplicon and pGDP3 backbone at 37°C for 15 min. Additionally, the backbone was simultaneously treated with rSAP. The cut backbone was gel

extracted and left to ligate with the cut insert using T4 DNA ligase for 10 min at room temperature (RT) and then heat inactivated for 10 min at 65°C. The ligation reaction was transformed and plated. Colonies were picked, grown, and miniprepped. The final assembly product, WT vatA/pGDP3, was confirmed through Sanger sequencing by Quintara using primers BDPR and AmprReverse(-121). All primer sequences are listed in **Table 2.1**.

Design and generation of VatA site saturation mutagenesis library inserts

The VatA mutagenesis library was prepared by Twist Bioscience using the aforementioned WT vatA/pGDP3 plasmid as a template. The library was designed to include all possible single amino acid mutants by incorporating *E. coli* optimized codons for all 20 amino acids at all positions, including synonyms wild type and early STOP codons. In total, 218 positions were mutagenized, making a library of 4578 mutants. The lyophilized library inserts were delivered in 96-well plates, with each well containing 50 ng of variant inserts per position. The inserts were stored at -20°C until needed.

Assembly and culturing of VatA library in pGDP3 selection vector

Each well of lyophilized library insert was resuspended in 100 µL of TE buffer, mixed by pipet, and transferred in full to a separate 1.5-mL tube. Next, 10 µL from each tube (5 ng per position) were pooled together. The pooled library inserts were cleaned and concentrated (Zymo D4004) across 16 columns using a 5:1 binding buffer ratio. Each column was eluted with 6 µL of elution buffer (EB) and pooled into one tube. The concentration of the resulting pool of library inserts was determined by the Qubit using the HS dsDNA assay. The purity and size of the pooled library inserts were confirmed by running 40 ng of DNA on a 0.8% agarose DNA gel stained using SYBR-Safe.

The entire library insert pool was digested with BamHI-HF and HindIII-HF (NEB) at 37°C for 3 h, followed by heat inactivation at 80°C for 20 min. The digested inserts were then cleaned

and concentrated (Zymo D4004) on one column into 20 µL of EB. Similarly, the pGDP3 backbone was prepared by digesting WT vatA/pGDP3 with BamHI-HF, HindIII-HF, MfeI-HF, and rSAP (NEB) at 37°C for 3 h. The reaction was heat inactivated at 80°C for 20 min and then gel extracted (Zymo D4001). The concentrations of both cut library insert and cut backbone were determined by Nanodrop.

Cut library inserts (40 ng) were T4-ligated with 100 ng of cut backbone (2:1 ratio by weight) overnight at 16°C. The ligation reaction was then cleaned and concentrated (Zymo D4004) to 6 µL in EB, all of which was electroporated into 20 µL of MegaX cells (Invitrogen). As a transformation efficiency control, 100 ng of cut backbone were also electroporated. Immediately after electroporation, 1 mL of supplied LB media was added to the cells. After recovering for 1 h at 37°C with shaking, the following dilutions of assembled library culture and control culture were plated onto LB/CARB agar: 1/100, 1/1k, 1/10k, 1/100k, 1/1M. The remaining assembled library culture was divided in half, and each half (~495 µL) was added to 100 mL LB/CARB in a 500-mL flask. These cultures were left to grow at 37°C with shaking, and their OD_{600}'s were recorded every ~30 min from the time of inoculation. Cultures were harvested at OD_{600}'s of 0.60 and 0.62. Cultures were combined and centrifuged at 4000 rpm for 15 min at 4°C. Half the resulting pellets were stored at -20°C as backup while the assembled library DNA was harvested from the other half using a midiprep kit and eluted across 2 columns in a total of 400 µL warmed EB (Zymo D4201-A). The concentration of extracted library plasmids was determined by Qubit, and some of this DNA was used to prepare 10 ng/µL aliquots in EB to avoid freeze-thawing the stock for transformations later. Library plasmid DNA was stored at -20°C until further use.

The following day, colony counts on the dilution plates were used to determine transformation efficiency of the library. We defined the minimum acceptable TE of the library to be 100X the library size, or roughly 500,000 clones. Additionally, the harvested library DNA was

only kept if the number of colonies on assembled library plates were significantly greater than the number of colonies on the backbone-only control plates.

Preparation of selection cell strain

Obtaining E. coli ΔbamBΔtolC strain for selection experiments

Selections were performed using a hyperpermeable, efflux-deficient strain of *E. coli* that lacked genes for BamB and TolC, essential components of efflux pump systems[64]. This delinquent strain is more membrane permeable, which was essential to ensure that any positive growth results were attributable to the VatA enzyme deactivating the SA analog through acetylation and not due to the cells ejecting the antibiotics through the use of their efflux pumps.

Making electrocompetent E. coli cells

Throughout the preparation, *E. coli* ΔbamBΔtolC cells were grown in antibiotic-free conditions at 37°C, with attention to aseptic technique. Cells were propagated on an agar plate overnight from a glycerol stock. One colony was picked to grow in 6 mL LB overnight, all of which were used to inoculate 300 mL of LB. When this culture reached OD_{600} 0.5-0.8, it was divided into pre-chilled 50-mL Falcon tubes, cooled on ice for 15 min, and then centrifuged at 4000 rpm for 20 min at 4°C. All pellets were collected and resuspended in a total of 75 mL sterile, chilled 10% glycerol. The resuspended cells were centrifuged for a second time at 4000 rpm for 10 min at 4°C. This step was repeated once more. Finally, all pellets were resuspended in a total of 2 mL 10% glycerol. These resuspended cells were allotted into 50 µL in PCR tubes and immediately plunged into LN2. Aliquots were kept at -80°C until needed.

Propagation of cell culture and set-up for growth experiments

Here described are the methods for propagation and set-up of cell culture harboring library or other pGDP3 systems for all growth experiments. On Day 1, the plasmid was

electroporated into 50 µL of *E. coli* ΔbamBΔtolC and immediately suspended in 1 mL SOC. The cells were left to recover for 1 h at 37°C with shaking. Next, 10 µL of this recovered culture were used to prepare the following dilutions, which were plated onto LB/CARB agar: 1/100, 1/1k, 1/10k, 1/100k, 1/1M. The remaining culture was added to 5 mL LB and 6 µL CARB to prepare an overnight culture. This 6-mL ON was left to grow at 37°C with shaking for 14 h.

On Day 2, 5 µL of the ON culture were diluted 1:1000 in 5 mL of LB/CARB. This 5-mL culture was left to grow at 37°C with shaking until OD_{600} reached 0.10. Meanwhile, SA analogs were diluted in DMSO from their 10 mM stocks in 100% DMSO to the appropriate working concentrations and added to LB/CARB media.

Once the 1:1000 culture reached OD 0.10, the culture was diluted 1:100 into 125-mL Erlenmeyer flasks containing 25 mL of LB/CARB/SA media such that the theoretical OD of the starting culture would be 0.001. To be consistent, the order in which each selection experiment was inoculated was the same as the order they would be OD'd, collected, and replenished later. Selection flasks were left to grow at 37°C with shaking at 180 rpm.

VatA library antibiotic selection

Choosing initial analog concentrations for VatA library selection experiments

Concentrations of the chosen SA analogs were first selected based on the range of VM2 concentrations that provided the best differential growth rates for WT, a known loss of function mutant, L113A, and a newly identified gain of function mutants, M107T and V61A. Growth experiments were set up by electroporating 100 ng of DNA for WT, L113A, M107T, and V61A into 40-50 µl of *E. coli* ΔbamBΔtolC cells and letting the cultures recover with shaking for 1 h at 37°C in 1 mL of LB. Then, 500 µl of recovered culture was diluted into 5 mL of LB for an OD reading. Turbidity of the cultures was adjusted until OD was between 0.08-0.13. Within 30 min, 10^8 CFU/mL (50 µl) of culture was used to inoculate a total of 100 µl growth, including VM2 diluted to as appropriate in DMSO. Growth experiments were performed in 96-well clear bottom

plates sealed with breathable seals. OD readings were recorded in a plate reader every 5 min for 12-20 h, or until saturation at OD 2.0. The concentrations 1, 0.5, and 0.25 mg/L were chosen for all compounds.

Choosing normalized analog concentrations for VatA library selection

Concentrations of the chosen SA analogs were carefully selected to best equalize their selective pressure and supply the least pressure possible, while still maintaining selection, so as to maintain a high level of diversity in the library and avoid quickly leading to a monoculture. Therefore, we sought SA concentrations just above the selective threshold by observing the differential between the growth curves of the VatA library and the negative control: empty pGDP3 vector lacking the *vatA* gene. SA concentrations were tested in a 1.2-fold dilution range. Growth experiments were set up by electroporating 10 ng of library and empty vector and propagating the cultures following the methods previously described above, except that calculating TE for the empty pGDP3 was not necessary. OD readings were recorded every hour until saturation at OD 2.0. Concentrations where no difference was observed between the library and empty vector growths were deemed too low, and the three concentrations above this threshold were selected for the DMS experiments. These trends were validated across a minimum of two replicates on different days to ensure reproducibility.

Validation of library selection conditions using WT VatA

To validate that the normalized SA concentrations chosen above the selection threshold of the empty vector were high enough to also supply a selective pressure on the library, we compared the growth curves of the VatA library and WT VatA in the chosen SA conditions. 10 ng of the library and WT VatA were electroporated and propagated following the methods previously described, except that calculating TE for the WT VatA plasmid was not necessary. OD readings were recorded roughly every hour for a total of 6 h.

VatA library selection and taking time points

For the selection experiments, 10 ng of the library were electroporated and propagated following the methods previously described. The remainder of the 1:1000 growth was collected and used later as the t0 time point; it was stored at -20°C for further use. All other time points were collected from each selection culture every 2 h after inoculation. Only 3 flasks were removed from the shaking incubator at a time to reduce the time left unshaking and unwarmed. For each selection experiment, the OD was recorded using 1 mL of culture, which was then stored in a 1.5-mL tube. To replenish the culture and retain a consistent selective pressure, 1 mL of LB/CARB/SA of the appropriate concentration was added back into the selection flask. Once all 3 flasks were OD'd, samples taken, and replenished, they were returned to the shaking incubator, and the next batch was removed. This repeated until all selection flasks were observed. Time point collection proceeded until 12 h post inoculation. Therefore, time point sampling occurred at 0, 4, 8, and 12 h after inoculation. All 1-mL time point samples were stored at -20°C for further use.

Illumina NGS Sequencing

Tile design

To accommodate the sequencing length limit of the 250PE NovaSeq run, we took a tiling approach to sequencing. The vatA gene, itself 660 bp long, was subdivided into two overlapping tiles. Primers to amplify each tile were designed with overhangs complementary to UC-TruSeq indexing primers. The primers used for Tile 1 were tile1-F and tile1-R. The primers used for Tile 2 were tile2-F and tile2-R. All primer sequences are listed in **Table 2.1**.

Preparation of time point DNA for sequencing

Time point samples were thawed at RT. Only 750 μL of culture were miniprepped using Zymo's 96-well plate kit (D4043). The remaining 250 μL were stored at -20°C as backup. DNA

was eluted in 30 µL of warmed EB, following 2 min incubation at RT. Half of this eluate was stored at -20°C as an additional backup, while the other half continued through the sample preparation pipeline.

The VatA gene was amplified for 15-20 cycles into Tile 1 and Tile 2 by using half the eluted DNA as template and following the protocol for NEBNext Ultra II Q5. The annealing temperatures used for Tile 1 and Tile 2 were 69°C and 67°C, respectively. PCR reactions were done in 96-well PCR plates (Bio-Rad MLP9601) sealed with a foil plate seal (TempPlate 2923-0100) and performed using a BioRad 96-well thermocycler. Products were cleaned and concentrated, following 2 wash steps, using ZR-96 D4024. DNA in each well of the plate was eluted in 15 µL of warmed EB, following 3 min incubation at RT.

Next, the DNA was digested by DpnI (NEB) in CutSmart buffer for 1 h at 37°C in a bead bath. Products were cleaned, concentrated, and eluted in 15 µL as previously described. Finally, 1 µL of all DNA samples were analyzed via Qubit (HS dsDNA assay, Q32851) to confirm sufficient quantities of DNA were produced and to provide quality control. In cases where insufficient DNA was produced, both additional PCR cycles and backup samples were used to supplement. Samples were stored at 4°C in between steps.

Illumina sequencing

Prepared DNA samples were delivered on dry ice to QB3/Functional Genomics Lab at the University of California Berkeley. Samples were indexed using UC-TruSeq primers. The quality and size of amplicons were confirmed using the BioAnalyzer before stoichiometrically being pooled. Samples spiked with PhiX DNA were run on 2 lanes of a 250PE NovaSeq SP.

DMS data analysis and variant score calculation

Raw Illumina data were demultiplexed by QB3/Functional Genomics Lab. PhiX DNA and poor reads were removed using *Illumina_preprocessing_pipeline.nf*, available on github.

Forward and reverse reads of the same experimental tile were merged. Tiles of the same experimental sample were aligned using LibraryAnalysis2, available on github. Outputs were reformatted for Enrich2 using *get_enrich_inputs_v13.1.py*, available on github. Reads were scored in Enrich2 using weighted least squares and normalized by total reads; source code for Enrich2 is made available on github by the Fowler Lab.

Growth validation of GOF VatA mutants

GOF mutants were prepared through site-directed mutagenesis of the wild type VatA gene in pGDP3 using the primers listed in **Table 2.1** and the Q5 Site-Directed Mutagenesis Kit (NEB, E0552S). Mutants were confirmed through Sanger sequencing by ElimBio using BDPR and AmprReverse(-121) sequencing primers, listed in **Table 2.1**. Electroporation and propagation of mutant VatA cultures were done following the methods previously described, except that calculating TE was not necessary and only one SA condition was tested. Growth curves were determined by tracking ODs every 2 h for a total of 6 h. Growth validation was carried out in duplicate.

VatA mutant expression and purification

The pET28a plasmid containing an N-truncated WT VatA gene with an N-terminal 6xHis-tag followed by a tobacco etch virus (TEV) protease cleavage site, as described in Chapter 1, was used as the template for cloning. First, the missing amino acids were cloned into the wild type gene using primers p02-F and p02-R and the Q5 Site-Directed Mutagenesis Kit (NEB, E0552S). Successful clones were then subjected to site-directed mutagenesis to incorporate the desired amino acid mutations using the primers listed in **Table 2.1** and the Q5 Site-Directed Mutagenesis Kit (NEB, E0552S). Sanger sequencing by ElimBio was used for sequence confirmation steps using T7 forward and T7 reverse sequencing primers. Mutant plasmids were

transformed in *E. coli* BL21 cells for VatA protein expression. VatA expression and purification were performed as described in Chapter 1. All primer sequences are listed in **Table 2.1**.

Table 2.1. Sequences of primers used for sequencing and cloning of vatA. Lower case identifies overhangs and mutated codons. Where used, -F indicates a forward primer and -R indicates a reverse primer.

Primer name	Sequence (5' to 3')
BDPR	ATAATGGTGCAGGGCGCTGAC
AmprReverse(-121)	GTGCACCCAACTGATCTTCA
T7 forward	TAATACGACTCACTATAGGG
T7 reverse	GCTAGTTATTGCTCAGCGG
p01-F	nnnnnnccatggGACCTGATCCCGAAAATATTTTACCGATAAAAGGGAATCGG
p01-R	AGTTATTGCTCAGCGGTGGCAGCAG
p02-F	ggatcctaccATGAATTTAAACAATGACCATGGACCTGATCCCGAAAATATTTTACCG
p02-R	tatctccttcttaaagttaaacaaaattatttctagagaagc
tile1-F	cctacacgacgctcttccgatctAAGAAGGAGATATACCGGATCCTACCATG
tile1-R	agacgtgtgctcttccgatcTGTGACAACAGCTTCTGCAGC
tile2-F	cctacacgacgctcttccgatctGGGACATTGAAATTGGAAATGATGTATGG
tile2-R	agacgtgtgctcttccgatcGAGGGTACCCAATCCGTTATTCTTCACC
L166A-F	TGGAAATCCCgcaAAATTTATAAGAAAAAG
L166A-R	CCGACAATAGAATAGGGAG
K171W-F	ATTTATAAGAtggAGGTTTTCTGATGGAGTTATC
K171W-R	ATTTATAAGAtggAGGTTTTCTGATGGAGTTATC
G176E-F	GTTTTCTGATgaaGTTATCGAAGAATG
G176E-R	CTTTTTCTTATAAATTTTAAGGGATTTC
L189W-F	ATGGTGGAATtggGATATGAAAATTATTAATG
L189C-F	ATGGTGGAATtgtGATATGAAAATTATTAATG
L189-R	TGTAAAGCTAACCATTCTTC
I193W-F	AGATATGAAAtggATTAATGAAAATCTTCCCTTC
I193F-F	AGATATGAAAtttATTAATGAAAATCTTCCC
I193-R	AAATTCCACCATTGTAAAGC
N197W-F	TATTAATGAAtggCTTCCCTTCATAATAAATGG
N197F-F	TATTAATGAAtttCTTCCCTTCATAATAAATGGAG
N197L-F	TATTAATGAActgCTTCCCTTCATAATAAATGGAG
N197M-F	TATTAATGAAatgCTTCCCTTCATAATAAATGG
N197C-F	TATTAATGAAtgtCTTCCCTTCATAATAAATGGAG
N197-R	ATTTTCATATCTAAATTCCACC
V61A-F	TCATTATGAAgcgATTGGAGATAAG
V61A-R	TATAAGACTTGATCTTCAAAGG
M107T-F	GGAGAAGTATaccCCTTCCTTAAAAGATCTTC
M107T-R	CAACCCATCCTGAATAGATG

Chapter III

Exploring the potential of covalently linked streptogramin groups A and B antibiotics

Contributing Authors

Jenna Pellegrino[1], Yoshito Takahashi[2], Volga Kojasoy[3], D. John Lee[1], Dean J. Tantillo[3], James S. Fraser[1], Ian B. Seiple[2]

[1]Department of Bioengineering and Therapeutic Sciences, University of California, San Francisco, San Francisco, CA, USA.

[2]Department of Pharmaceutical Chemistry, Cardiovascular Research Institute, University of California, San Francisco, San Francisco, CA, USA.

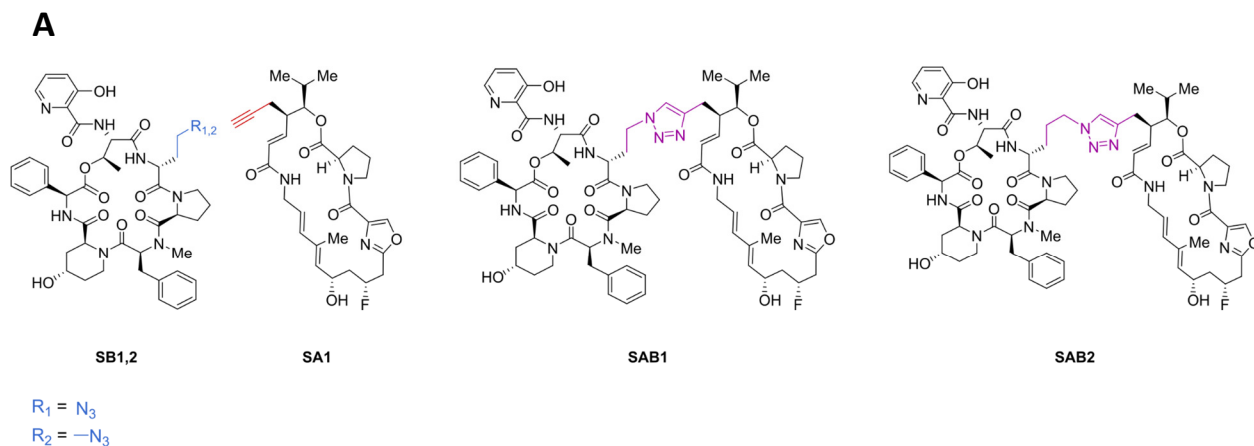[3]Department of Chemistry, University of California, Davis, Davis, CA, USA.

Introduction

Streptogramin group A and group B antibiotics are naturally produced by the same species of bacteria, *Streptomyces*. These antibiotics bind beside each other in the bacterial ribosome and have a synergistic antimicrobial effect, acting as bactericidal antibiotics when used together. While this phenomenon makes SA and SB a powerful combination, the observance of this synergistic effect may be limited due to the susceptibility of each antibiotic to its own independent resistance mechanisms. This is especially the case with SA, which induces the conformational change in the PTC that allows SB to bind with higher affinity. Considering the close proximity in which these two antibiotics bind, we wondered whether analogs of SA and SB could be designed to induce click chemistry on the ribosome, covalently linking them together. We hypothesized that, compared to the individual streptogramin analogs, the clicked molecule would demonstrate improved activity on the ribosome due to its increased contacts making it more difficult to be dislodged by resistance mechanisms. Here, we explore the structure of pre-

clicked SA and SB analogs bound to the *E. coli* ribosome to inform design of clickable streptogramin molecules. We also examine how post-clicked molecules SAB1 and SAB2 interact with the ribosomal binding pocket.

Results and Discussion

In order to design SA and SB analogs with the potential to perform click chemistry on the ribosome, we first observed the structure of natural streptogramin antibiotics VM2 and VS1 bound to the *E. coli* ribosome (EMPIAR-11024). Inspired by the successful use of azide-alkyne cycloadditions on solithromycin antibiotics[68], we determined that click chemistry could be attained by installing an alkyne at the C4 position of the streptogramin A molecule and an azide on the streptogramin B molecule, following a single carbon extension to bring these moieties within proximity to react (**Fig. 3.1a**). These molecules, here named SA1 and SB1, were tested along with their clicked product, SAB1, for their activity against a panel of bacterial strains. These minimum inhibitory concentration (MIC) data showed that analog SA1 was moderately less active, compared to flopristin (0.25-2 µg/mL compared to 0.125-4 µg/mL; **Fig. 3.4b**). Compared to virginiamycin S1, SB1 was more active in both Gram-positive strains tested (2-4 µg/mL compared to 8-16 µg/mL) but significantly less active in all three strains of deficient *E. coli* strains (4-32 µg/mL compared to 1-4 µg/mL). However, SAB1 was not active at all, with the exception of two deficient *E. coli* strains with their efflux pumps and out membrane systems knocked out (16-32 µg/mL). We hypothesized this was due to the inability of the large compound to penetrate into the cell but that SAB1, if formed through click chemistry of the active compounds SA1 and SB1 on the ribosome, may result in significantly improved MIC compared to SA1 and SB1 alone. This hypothesis was supported by the observation that SA1 and SB1 showed slight synergistic favorability for each other (**Fig. 3.1c**).

A

R₁ = N₃ → $R_1 = N_3$
R₂ = —N₃ → $R_2 = -N_3$

B

MIC (µg/mL)

	S. aureus	*S. pyogenes*	*E. coli* ΔtolC[*]	*E. coli* ΔbamBΔtolC[ɤ]	*E. coli* ΔsurA[*ɤ]
flopristin	0.25	0.25	0.5	0.125	4
VS1	8	16	4	4	1
SA1	0.5	1	1	0.25	2
SB1	4	4	32	8	4
SAB1	>64	>64	>64	16	32

C

SA1

	µg/mL	4	2	1	0.5 (MIC)	0.25	0.125	0.063	0.031	0.016	0
SB1	16	12.000	8.000	6.000	5.000	4.500	4.250	4.125	4.063	4.031	
	8	10.000	6.000	4.000	3.000	2.500	2.250	2.125	2.063	2.031	
	4 (MIC)	9.000	5.000	3.000	2.000	1.500	1.250	1.125	1.063	1.031	
	2	8.500	4.500	2.500	1.500	1.000	0.750	0.625	0.563	0.531	
	1	8.250	4.250	2.250	1.250	0.750	0.500	x	x	x	
	0.5	8.125	4.125	2.125	1.125	0.625	0.375	x	x	x	
	0.25	8.063	4.063	2.063	1.063	0.563	x	x	x	x	
	0										

Figure 3.1. Activity of clickable streptogramin analogs. **(A)** Pre-clicked streptogramin analogs with their respective clicked analogs: SA1 and SB1 with SAB1; SA1 and SB2 with SAB2. SB1 and SB2 differ in the R group of their azide linker (blue). SB1 corresponds to R_1, while SB2 corresponds to R_2. The alkyne (red) and azide interact via Huisgen cyclization to form the triazole linker (purple). **(B)** Antimicrobial activity (MIC in µM) of streptogramin A and B compounds in various bacterial strains. *Efflux knockout strain. ɤOuter membrane knockout strain. **(C)** Fractional inhibitory concentration (FIC) index of SA1 and SB1. The FIC index is calculated from *S. aureus* MIC data as follows: FIC index = $FIC_A + FIC_B = [A]/MIC_A + [B]/MIC_B$. Regions are colored such that red indicates antagonism, yellow indicates indifference or additivity, and green indicates synergism. Regions in gray represent concentrations of either compound that were too low to inhibit cellular growth.

We proposed that SA1 and SB1 would react on the ribosome to form a triazole linker in the new clicked molecule, SAB1, following the Huisgen cyclization reaction. To observe this, we incubated analogs SA1 and SB1 for 24 hours with the *E. coli* ribosome and obtained a high-resolution Cryo-EM structure of the product. Our 2.35-Å structure revealed that SA1 and SB1 remained unlinked molecules (**Fig. 3.2a**). Density for the azide suggests disorder in this moiety, which appears to be stabilized in two alternative conformations. In one conformation, the azide hydrogen bonds with an oxygen in the ribose of U2585; the other conformation reveals a hydrogen bond with the nitrogen in the SA1 macrocycle (**Fig. 3.2b**). In both conformations, the azide is not well positioned to perform click chemistry with the alkyne.
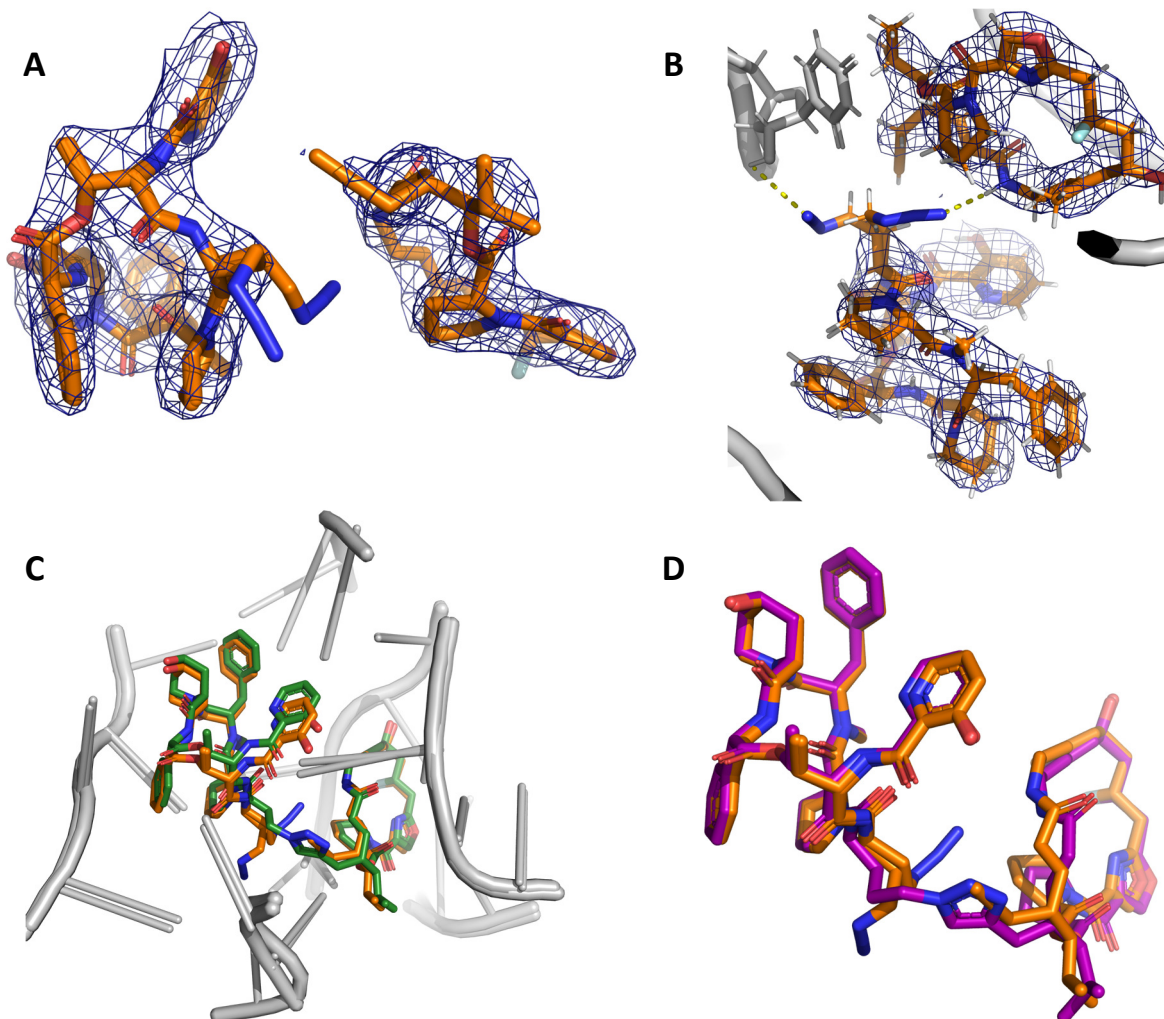
Figure 3.2. Ribosome binding of pre- and post-clicked antibiotics. **(A)** Cryo-EM of SA1 (right) and SB1(left) does not support the occurrence of click chemistry between the two compounds in the *E. coli* ribosome. SB1 is modeled in two alternative conformations. **(B)** SB1's azide is stabilized by hydrogen bonding to either U2585 (3.3 Å) or the SA1 macrocycle (2.3 Å). **(C)** Overlay of SA1 and SB1 (orange) with their post-clicked counterpart, SAB1 (green). SAB1 exhibits translational perturbations in the SB portion. **(D)** Overlay of SA1 and SB1 (orange) with SAB2 (purple).

To inform our next designs of potentially clickable streptogramin analogs, we obtained a Cryo-EM structure of SAB1 with the *E. coli* ribosome. While this 2.23-Å structure revealed minimal perturbations in the ribosome at the binding site, we observed differences in the pose of SAB1 compared to its pre-clicked counterparts. The SA portion of the molecule binds in nearly the same pose as SA1, but the SB portion exhibits translational perturbation (**Fig. 3.2c**). This translational shift supports our previous structural observation that SB1 does not bind in an ideal pose for clicking with SA1. Further, since the SB portion of SAB1 is in a different pose than SB1 alone, this portion of the molecule may not be in its optimal pose on the ribosome, either exhibiting higher energy or jeopardized contacts with the binding pocket. In order to encourage click chemistry between SA and SB analogs, we concluded that modifications to SB1 were needed.

Computational analysis of SA1 and SB1 was used to inform the design of our next clickable SB component. We determined the predicted energy barrier for a reaction between methylazide and propyne to form the triazole to be high at 29.0 kcal/mol, even at an ideal distance from each other (**Fig. 3.3a**). Using the lowest energy conformers of SA1 and SB1, based on their poses in our Cryo-EM model, we found that these regions of the molecules were significantly further away than ideal at 4.6 Å (**Fig. 3.3b**), which could be due to interactions between the analogs and the ribosome residues, as previously discussed. As a distance of 3.44 Å should not be exceeded for click chemistry to occur between SA and SB components, our results confirm that SA1 and SB1 are not in productive orientations for click chemistry to occur on the ribosome.
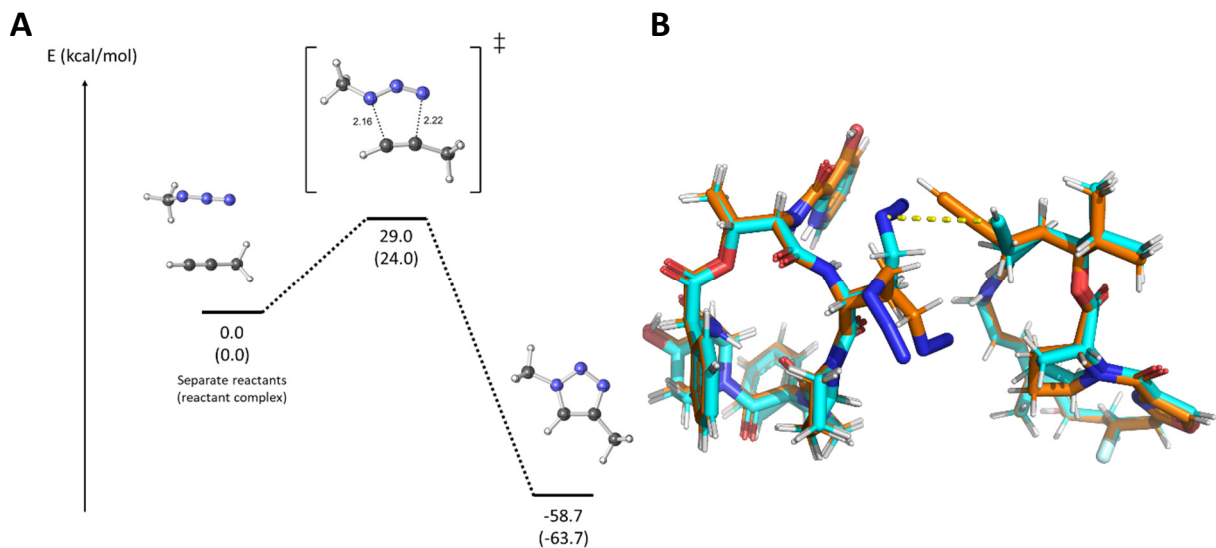
Figure 3.3. Potential for click reaction. **(A)** Reaction diagram for methylazide and propyne forming a triazole. Energies are reported in kcal/mol. **(B)** Overlay of the Cryo-EM models of SA1 and SB1 (orange) with their lowest energy conformers (cyan), for which the distance between the reacting species is 4.6 Å.

These results led us to hypothesize that adding a carbon to the SB1 linker, creating the new analog called SB2, might bring the azide close enough to the alkyne to encourage click chemistry on the ribosome. To explore this result on a structural level, we obtained a high-resolution (2.27 Å) CryoEM structure of SAB2, the clicked product of SA1 and SB2, bound the *E. coli* ribosome. Structural analysis revealed that SAB2 adopts a nearly identical pose as SA1 and SB2, suggesting improved potential for its pre-clicked counterparts to react on the ribosome (**Fig. 3.2d**). Further experiments will be required to better understand the supported chemistry that can occur in this binding pocket and to inform other approaches to designing clickable antibiotics. Although we were unsuccessful in designing SA and SB analogs that could perform click chemistry on the ribosome, these preliminary studies underline the complexities with designing clickable molecules on the ribosome and demonstrate the flexibility of the ribosomal binding pocket in accommodating large antibiotics.

As a final means of investigating the activity of SAB1 and SAB2, we explored the capability of these molecules to inhibit translation of the 70S *E. coli* ribosome in vitro. Interestingly, our IVT data revealed that SAB1 and SAB2 are worse ribosomal inhibitors than

flopristin (**Fig. 3.4**). Considering that we have observed SAB1 and SAB2 binding at the ribosome through Cryo-EM, it is possible that factors during the active translation process, such as the presence of mRNA or tRNA, could impede the binding of these molecules and decrease their activity. Another potential explanation for this result is that SAB1 and SAB2 are large molecules composed of two antibiotics, each having their own resistance sensitivities. It is possible that having SA and SB covalently linked together leads to greater susceptibility of the SAB compound to factors that discourage binding of either portion of the molecule, which in turn affects the binding of the other half. Further calculations will be necessary to better understand this on a molecular level.
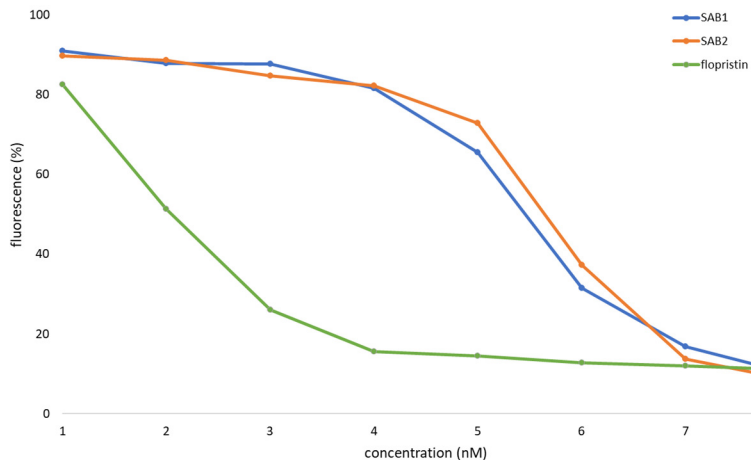

Figure 3.4. In vitro translation of the 70S *E. coli* ribosome at 23.9 nM in complex with inhibitors SAB1 (blue), SAB2 (orange), or flopristin (green). Inhibitor concentrations are reported in nM. Readout is reported in percent fluorescence, compared to a no-compound DMSO control.

Methods

Computational energy calculations

Constrained conformational searching for SA1 and SB1 were performed with CREST (version 2.11.1) using the GFN2//GFN-FF force field and the generalized Born model with the solvent accessible surface (SASA) water solvent model[69,70]. Density functional theory calculations were carried out using Gaussian 16[71] at the PCM(H2O)-B3LYP-D3(BJ)/def2-SVP level of theory[72–76].

MIC testing and checkboard assay

Compounds were evaluated for MIC activity against a variety of bacteria using the broth microdilution method of antimicrobial substances[77].

In vitro translation assay screen

The ability of antibiotic compounds to inhibit the 70S *E. coli* ribosome was performed based on methods described in Chapter 1. Inhibition of streptogramin compounds were determined using the PURExpress Δ Ribosome Kit (E3313, NEB) for in vitro protein synthesis, 70S *E. coli* ribosomes (P0763S, NEB), murine RNase inhibitor (M0314, NEB), and 6.66 ng/µl of template DNA encoding the fluorescent protein mEGFP (gift from the Cate laboratory). This kit was specifically used to achieve a final ribosome concentration of 24 nM. The volume of the reaction mixture was scaled down fivefold from the NEB protocol for a final reaction volume of 5 µl. Analogs were tested in a range from 70 to 9000 nM in 1% DMSO (final concentration). Translation reactions were carried out in triplicate in a 37°C dry incubator for 4 h, then transferred to a 0°C ice bath. To assist in the transfer of reactions to 96-well half-area NBS microplates (Corning 3993) for final measurements, the reaction volume was increased to 50 µl by adding buffer (20 mM Tris-HCl pH 7.5, 60 mM NH4Cl, 6 mM MgCl2, 0.5 mM EDTA). Using a Cytation 5 plate reader (BioTek), translated mEGFP was excited at 485 nm; its emission was recorded at 535 nm. Raw data were processed and visualized using Microsoft Excel.

Cryo-EM sample preparation

Cryo-EM samples were prepared as described in Chapter 1 with the following exceptions: For the ribosome sample prepared with SA1 and SB1, the antibiotic analogs were incubated with the ribosome in the sample buffer for 24 h at 4°C prior to vitrification. All samples were incubated on freshly glow-discharged Quantifoil holey carbon grids with 1.2/1.3 spacing

and 2 nm carbon on top (C2-C14nCu30-01) for 30 s at 10°C and 100% humidity prior to
vitrification.

Cryo-EM data collection and processing

All datasets were collected on FEI Titan Krios electron microscopes (ThermoFisher,
operating at 300 kV, located at UCSF). Automated data collection was facilitated by SerialEM
(v3.6)[53]. All data sets were collected on a K3 (Gatan) Direct Electron Detector (DED) with a
Gatan Imaging Filter (Gatan, 20 eV slit for SAB1 and SA1+SB1, 10 eV for SAB2) nine-shot
beam-image shift approach with coma compensation[55]. The SAB2 additionally took 4 shots per
hole. Pixel sizes, number of images in dose-fractionated micrographs, dose rates, and defocus
ranges varied slightly and are reported in **Table 3.1**. Image stacks for SA1+SB1 and SAB1 were
collected in super-resolution mode; image stacks for SAB2 were collected in physical resolution
mode. Datasets were processed as described in Chapter 1, with the exceptions being that
binning SAB2 was not required, as it was collected in physical resolution mode, and final high-
resolution limits used were of either 3.20 or 3.00 Å (see **Table 3.1**).

Cryo-EM model building and refinement with OPLS3e

UCSF Chimera (v.1.12) was used to rigid body align our previous Cryo-EM model of the
E. coli ribosome (PDB: 6PC6) into our maps. Additional ribosomal protein chains were added to
this model from a high-resolution X-ray structure of the *E. coli* ribosome (PDB: 4YBB[59]).
Principle versions of the PHENIX suite used for Cryo-EM model building were 1.17 and 1.19.
Ligands were made by using the SMILES string and a 'final geometry' reference PDB of the
analog that was derived from either the pose of flopristin (PDB: 4U20[9]) or the pose of VS1
(PDB: 6WYV) bound to the *E. coli* ribosome. Structures were refined using
phenix.real_space_refine interfaced with the OPLS3e/VSGB2.1 force field[61], as described in
Chapter 1.

For all Cryo-EM figures, the full, unsharpened density maps and full PDB models were boxed using phenix.map_box with a selection radius of 20 Å around the ligand(s). Boxed map and model were loaded into PyMol (incentive v.2.4.1) and contoured at 4.0σ, centered around the ligand(s) with a carve of 1.4.

Author Contributions

J.P. and D.J.L. prepared samples and collected Cryo-EM data; J.P. calculated Cryo-EM reconstructions; J.P. performed Cryo-EM model refinements; Y.T. executed and optimized the syntheses of streptogramin A and streptogramin B analogs; Y.T. performed the MIC and checkerboard assays; Y.T. performed the in vitro translation experiments; V.K. performed the energy calculations; J.P., Y.T., and V.K. wrote the manuscript; D.J.T. assisted with the analysis of the energy calculations; I.B.S. assisted with designing synthetic routes; J.S.F. assisted with experimental design and edited the manuscript.

Extended Data

Table 3.1. Cryo-EM data collection, processing, and model refinement statistics for structures associated with SA1+SB1, SAB1, and SAB2.

	SA1+SB1	SAB1	SAB2
PDB code	8E32	8E33	8E35
EMDB	EMD-27854	EMD-27855	EMD-27857
EM data collection / processing			
Microscope	FEI Titan Krios	FEI Titan Krios	FEI Titan Krios
Voltage (kV)	300	300	300
Camera	Gatan K3	Gatan K3	Gatan K3
Electron exposure (e-/Å^2)	47.2	67	47.2
Defocus range (µm)	0.5 - 1.3	0.4-1.2	0.6 - 1.6
Pixel size (Å)	0.665	0.8261	0.665
Symmetry imposed	C1	C1	C1
Total number of micrographs	1980	1960	8240
Number of good micrographs	1761	1623	8036
Particles picked from all micrographs	190396	353461	821243
Particles from good micrographs	170514	292703	800949
Particles used in final reconstruction	161222	162125	537105
Map resolution (Å)	2.35	2.23	2.27
FSC threshold	0.143	0.143	0.143
High resolution refinement limit (Å)	3.2	3	3.2
Refinement			
Initial model used (PDB code)	4YBB	4YBB	4YBB
Model resolution (Å)	2.7	2.6	2.5
FSC threshold	0.5	0.5	0.5
Map sharpening B factor (Å^2)	0	0	0
Model composition			
Total atoms	116273	116091	116163
Hydrogens only	42226	42152	42176
Non-hydrogen atoms	74047	73939	73987
Protein residues	1179	1179	1179
Nucleotide residues	3016	3015	3016
Ligands	2	1	1
B factors (Å^2), mean			
Protein	64.55	80.61	42.43
Nucleotide	79.55	95.56	62.02
Ligand	43.26	73.65	27.94
R.m.s. deviations			
Bond lengths (Å) (# >4sigma)	0.001 (2)	0.002 (0)	0.001 (2)
Bond angles (°) (# >4sigma)	0.310 (4)	0.318 (4)	0.300 (10)
Validation			
MolProbity score	1.15	1.29	1.12
Clash score	1.21	1.98	1.03
Rotamer outliers (%)	0.74	0.53	0
Ramachandran plot			
Favored (%)	95.44	95.36	95.44
Allowed (%)	4.56	4.64	4.56
Outliers (%)	0	0	0
Cβ outliers (%)	0	0	0

Chapter IV

High-resolution Cryo-EM structures of novel ribosomal PTC-directed inhibitors

Contributing authors

Jenna Pellegrino[1], Qi Li[2], Jonathan H. Boyce[2], Seul Ki Yeon[2], Quinn Edmonson[2], Andrew K. Ecker[2], D. John Lee[1], James S. Fraser[1], Ian B. Seiple[2]

[1]Department of Bioengineering and Therapeutic Sciences, University of California, San Francisco, San Francisco, CA, USA.

[2]Department of Pharmaceutical Chemistry, Cardiovascular Research Institute, University of California, San Francisco, San Francisco, CA, USA.

Introduction

Expanding on our success and discoveries with novel SA analogs, we have studied many other analogs of ribosome-binding antibiotics. Here, I briefly introduce four collections of analogs for which we have obtained structures by Cryo-EM. The first of these is a continuation of our series of fluorinated SA analogs, in which we further explore C4 modifications to the macrocycle. Second are structures of the ribosome bound to solithromycin antibiotics, including two analogs conjugated to a siderophore linker designed for the purpose of improving uptake into gram-negative bacteria. The third is a collection of hybrid macrolide/oxazolidinone antibiotics. Finally, we explore the potential for synergy between tiamulin and NPET-binding antibiotics.

Results and Discussion

Other fluorinated C4-modified SA analogs

Since identifying SA 47 as an analog with great success in overcoming resistance mediated by WT VatA, we have made and studied several other fluorinated SA analogs with C4 modifications (**Fig. 4.1a,b**). The first of these is 3057, which replaces the terminal carbon of 47 with a hydroxyl. We hypothesized that this hydroxyl would hydrogen bond with nearby residue U2586, as was previously observed for 47. On the contrary, our EM structure (2.58 Å) of 3057 bound to the *E. coli* ribosome revealed a loss in the hydrogen bond with U2586 (**Fig. 4.1c**). The C4 extension of 3057 adopts a different binding pose than the C4 extension of 47, possibly due to steric clashing between the oxygen in the ribose of nearby U2585 and the hydroxyl of 3057. This positions the hydroxyl moiety of 3057 too far from U2585 to engage in hydrogen bonding. This hydrogen bond loss could explain the apparent decrease in translation inhibition activity of 3057, when compared to 47 (**Fig. 4.1b**). Compared to the structure of 47 bound to the ribosome, no change in the position of U2586 was observed. Although other PTC conformational change was observed between these structures, notably with U2506 and A2062, they do not appear to improve or affect the binding of 3057.

In vitro translation data revealed two SA analogs, 3142 and 3146, with significantly improved inhibitory action on the *E. coli* ribosome (**Fig. 4.1b**) and prompted further structural analysis via Cryo-EM. In both of these analogs, we explored long C4 extensions with conjugated rings that we hypothesized might engage in cation-pi interactions and/or pi-pi stacking with the ribosome to improve activity. Our 1.91-Å structure of 3142, the analog with the shorter extension, bound to the *E. coli* ribosome revealed a major and minor pose for the C4 extension (**Fig. 4.1d**). In the major pose, 3142 engages in one hydrogen bond with the U2586 nucleotide and another with the ribose of U2585. Surprisingly, it is in the minor conformation that the triazole ring stacks beneath the nucleotide of U2586. The minor pose of 3142 also engages in two hydrogen bonds with U2586: one in the nucleotide and one in the ribose.

Analog 3146 also exhibits heterogeneity in its C4 extension, as revealed by our 2.38-Å structure with the *E. coli* ribosome. Both conformations of 3146, which appear to be equally sampled, find the triazole stacked beneath U2586, which also hydrogen bonds to the small molecule (**Fig. 4.1e**). Only one conformer additionally hydrogen bonds with U2585 and U2609.

The observed heterogeneity of analogs 3142 and 3146 allow them to sample unique hydrogen bonding networks and other interactions with the ribosome. It is possible that, in these cases, heterogeneity may be a driving factor that improves the inhibitory effect of these molecules on the ribosome.

Figure 4.1. In vitro and structural analysis of novel streptogramin A analogs binding the ribosome. **(A)** Fluorinated streptogramin group A analogs with C4 modifications that showed significantly improved inhibitory activity on the *E. coli* ribosome, compared to VM2. **(B)** Fluorescence of meGFP translated by the *E. coli* ribosome after 1 hour incubation in the presence of 10 µM of each analog observed, relative to dimethylsulfoxide (DMSO). **(C)** Overlay of analog 3057 (raspberry) and analog 47 (green; PDB: 6PC6) bound to the *E. coli* ribosome. Compared to 47, the C4 extension of 3057 adopts a new pose that is too far away from residue U2586 to hydrogen bond. **(D)** Analog 3142 binds the *E. coli* ribosome in major and minor conformations. Hydrogen bonds are observed between the C4 extension and residues U2585 and U2586. In the minor pose, the triazole ring stacks below U2586. Hydrogen bonds are shown in dashed lines. **(E)** Analog 3146 binds the *E. coli* ribosome in two conformations, both of which find the triazole stacked below U2586. Hydrogen bonds are shown in dashed lines.

D- and L-linker solithromycin conjugates adopt distinct poses in the NPET

Five of the seven recognized ESKAPEE pathogens, regarded as the most urgent threats to human health, are Gram-negative. Owing to their selectively permeable outer membrane, these pathogens are particularly difficult targets for antibiotic design. Many successful antibiotic candidates mimic nutrient-essential molecules to hijack the cell's active transport system. An example of this is a siderophore-antibiotic conjugate (SAC), which makes strategic use of the cell's active transport of iron-chelating siderophore molecules. However, antibiotic conjugates commonly require further modification once inside the cell, such as proteolytic cleavage, in order to successfully bind their target and have the desired antibacterial effect. Previous work in the development of solithromycin SACs revealed unexpected results for a cleavable L-linker analog and an uncleavable D-linker analog[78] (**Fig. 4.2a**). Antimicrobial activity assays revealed that both linker conjugates demonstrated activity in several strains of *E. coli* in which linker cleavage was not required, but only the L-linker was active in cases where cleavage was necessary (**Fig. 4.2c**). This corroborated the expected result that SACs require lysis in order to function. However, cell-free translation inhibition of the 70S *E. coli* ribosome with these two linkers surprisingly revealed strong activity, even compared to solithromycin (**Fig. 4.2b**).
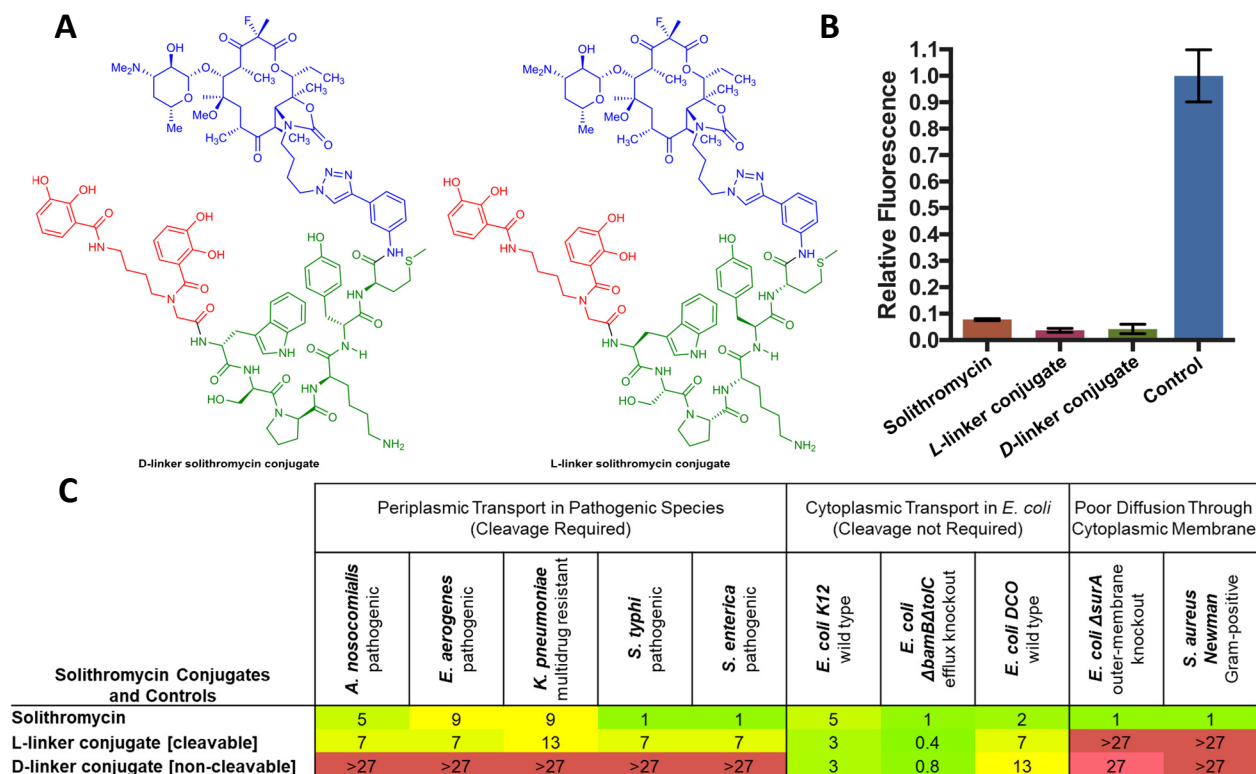
A

D-linker solithromycin conjugate

L-linker solithromycin conjugate

B

C

Solithromycin Conjugates and Controls	Periplasmic Transport in Pathogenic Species (Cleavage Required)					Cytoplasmic Transport in *E. coli* (Cleavage not Required)			Poor Diffusion Through Cytoplasmic Membrane	
	A. nosocomialis pathogenic	*E. aerogenes* pathogenic	*K. pneumoniae* multidrug resistant	*S. typhi* pathogenic	*S. enterica* pathogenic	*E. coli K12* wild type	*E. coli ΔbamBΔtolC* efflux knockout	*E. coli DCO* wild type	*E. coli ΔsurA* outer-membrane knockout	*S. aureus Newman* Gram-positive
Solithromycin	5	9	9	1	1	5	1	2	1	1
L-linker conjugate [cleavable]	7	7	13	7	7	3	0.4	7	>27	>27
D-linker conjugate [non-cleavable]	>27	>27	>27	>27	>27	3	0.8	13	27	>27

Figure 4.2. Activity of siderophore-antibiotic conjugates (SACs) of solithromycin. **(A)** The siderophore (red) is conjugated to the solithromycin (blue) through peptide linker WSPKYM (green) using either D- (left) or L- (right) amino acids. **(B)** In vitro translation shows, at 10 µM, the ability of the L- and D- linker conjugates to inhibit the 70S *E. coli* ribosome compared to solithromycin and a DMSO control, as shown in published work[78]. **(C)** Antimicrobial activity (MIC in µM) of solithromycin and the L- and D-linker conjugates, as shown in published work[78].

To investigate how these SACs interact with the ribosome, we obtained high resolution

Cryo-EM data of the L- and D-linkers (2.25-Å and 2.35-Å, respectively) bound to the *E. coli*

ribosome. We observed that both SACs bind the entrance of the NPET, near the PTC; however,

they adopt distinct binding conformations. Compared to a crystal structure of solithromycin

bound to the *E. coli* ribosome (PDB: 4WWW[44]), the macrocycle for both SACs adopts the same

conformation and binds the same site in the NPET (**Fig. 4.3a**). The non-cleavable D-linker

extends out from the entrance of the NPET to occupy a portion of the tunnel before folding back

over itself and extending back toward the entrance. In contrast, the cleavable L-linker adopts

roughly the same pose as the D-linker from the macrocycle until the triazole, where it deviates

by approximately 180 degrees and begins to fold over itself. Therefore, rather than binding

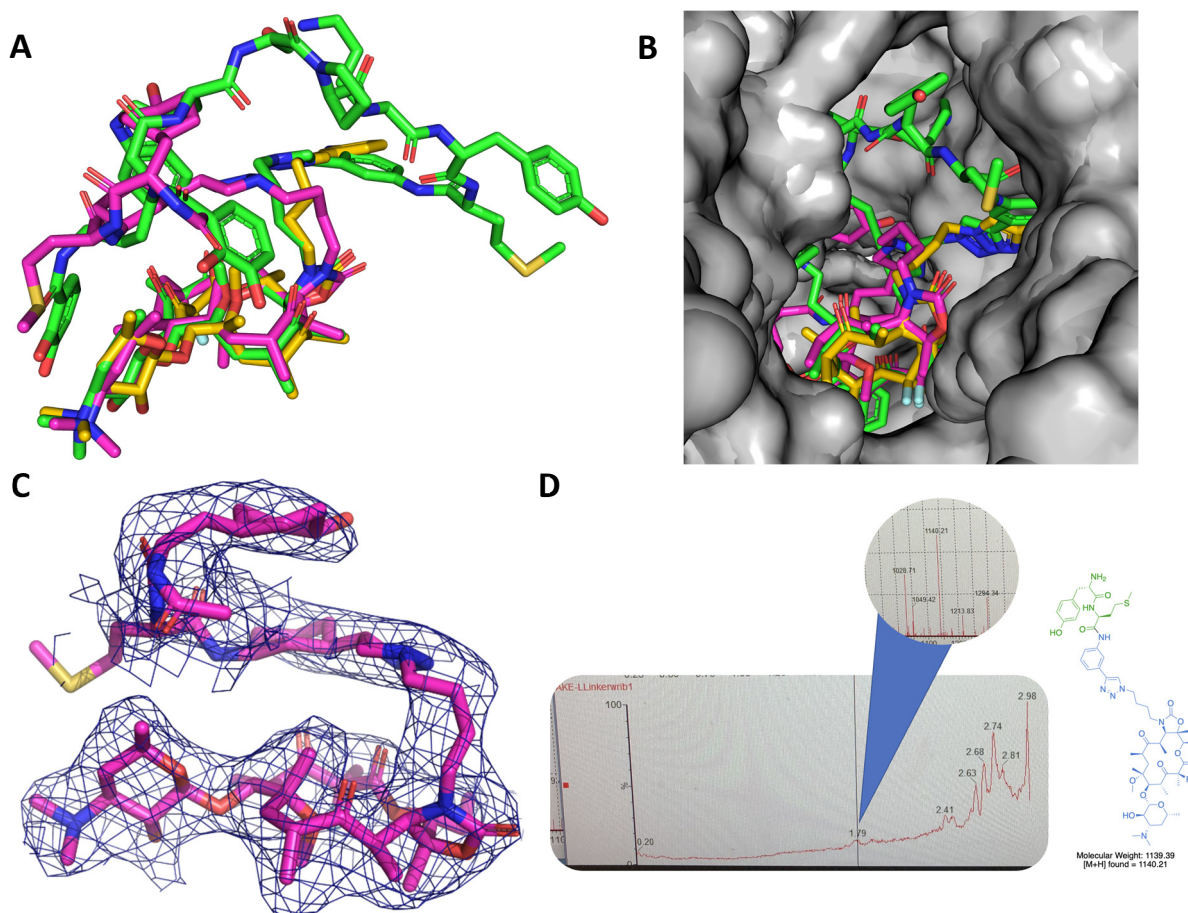deeper inside the tunnel, the L-linker remains by the entrance of the NPET (**Fig. 4.3b**).

Figure 4.3. Ribosome binding of solithromycin conjugates and LCMS. **(A)** Overlay of solithromycin from 4WWW[44] (yellow) with D-linker (green) and L-linker (pink) conjugates, all in the *E. coli* ribosome. The solithromycin macrocycle of all three ligands, aligned at bottom, all adopt the same pose. A portion of the D-linker can be seen extending down the tunnel, at right, before returning to occupy the entrance of the NPET. **(B)** A view down the NPET shows the D-linker solithromycin conjugate obstructing the cavity. The L-linker solithromycin conjugate and solithromycin compounds exclusively bind at the NPET entrance and do not fill down the cavity. **(C)** The 2.25-Å Cryo-EM Coulomb potential density map (contoured at 2.0σ with a carve of 2.0) for the L-linker solithromycin conjugate reveals weak density past the peptide linker. **(D)** HPLC-MS trace analysis of L-linker solithromycin conjugate exhibits possible cleavage following incubation with the ribosome mixture. The [M+H]+ ion found in the minor MS trace peak matches the molecular weight of the truncated compound supported by the Cryo-EM density.

Interestingly, density of the L-linker only supports modeling of the ligand up until the amide bond between the lysine and tyrosine of the peptide linker (**Fig. 4.3c**). While weak density past this point could suggest that the remainder of the molecule forms poor interactions with the ribosome and is unresolved, it is also possible that the molecule undergoes cleavage at this site of the linker, although not where proteolytic cleavage was expected to occur[78]. We hypothesized that the serine and lysine side chains, which respectively act as transesterification

and transamidation liabilities, could be the culprits of autocleavage in the L-linker. As no

proteases were present in the buffer of the vitrified ribosome-SAC mixture, any external linker

cleavage is unlikely. To investigate further, we performed LCMS of the linker compounds with

the 50S *E. coli* ribosome mixture used during EM sample vitrification. In one of the triplicate

samples with the L-linker, we identified a new peak on the LCMS trace which showed the ion

m/z of 1140.21 (**Fig. 4.3d**). This molecular weight matches the [M+H]+ ion expected for the

cleavage based on the observed density of the L-linker molecule. As none of the other

replicates showed this ion, thereby not supporting cleavage of either linker, our results suggest

that the L-linker is cleaving upon incubation with ribosomes. However, further work will be

needed to explore these observations further.

In the case where the lack of significant density for the L-linker solithromycin conjugate

past the carbonyl is indicative of a poorly stabilized linker, rather than linker cleavage, we

hypothesize that the linker may potentially obstruct binding of antibiotics in the neighboring PTC

binding site, such as streptogramin group A (SA) antibiotics. To corroborate this, we obtained a

1.99-Å resolution Cryo-EM structure of solithromycin and virginiamycin M1 (VM1), a naturally

produced SA, bound to the *E. coli* ribosome. We observed that, at the closest point, VM1 comes

within 2.5 Å of the L-linker (**Fig. 4.4**). Although the L-linker conjugate is active in more gram-

negative species than the D-linker, this may highlight a point of consideration when designing

solithromycin analogs, as it may be disadvantageous to block the binding of other antibiotics.
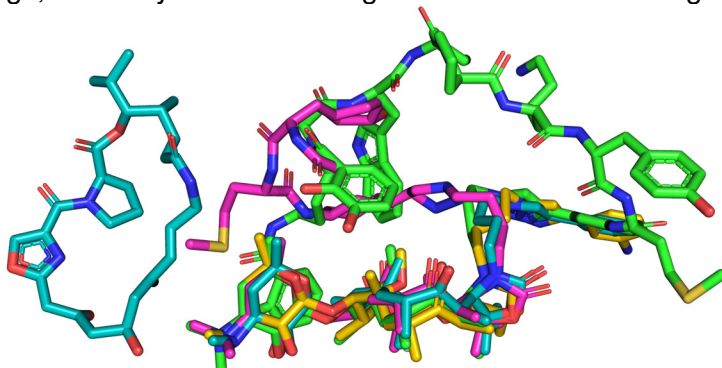

Figure 4.4. Ribosome binding of L-linker. L-linker (pink) could potentially obstruct binding of molecules in the PTC, such as streptogramin group A antibiotics. At the closest point, the methyl of VM1 (teal) comes within 2.5 Å of the L-linker.

While solithromycin is already beyond the traditional rules of what makes a drug-like molecule included in Lipinski's Rules of 5, the ability of these large conjugate molecules to undergo active transport through the cell and bind the ribosome provides opportunity for new beyond Rules of 5 (bRo5) antibiotic designs.

Though the goal of the initial work was to design new SACs which upon exposure to the bacterial periplasmic proteases, this new structural view of the binding of these large molecules suggest that these conjugates can be designed with non-cleavable linkers and still have efficacy in inhibiting ribosomal activity.

Further exploration of shorter, non-cleavable linkers may offer new favorable designs to take advantage of Gram-negative machinery. It is remarkable that such a large molecule as the D-Linker conjugate is able to fit into the NPET and acts as a good illustration of the plasticity of the NPET for future novel antibiotic design.

Hybrid macrolide/oxazolidinone antibiotic molecules

Resistance is developed against antibiotics that often is applied broadly to the entire antibiotic class and can also lead to cross-resistance against antibiotics of the other classes that bind the same site. Covalently linking antibiotics has shown to be a successful method of antibiotic design geared at restoring activity of antibiotics. For example, macrolones are antibiotics synthesized by linking macrolides, which bind at the NPET of the ribosome, to quinolones, which inhibit DNA gyrase. Linking antibiotics of these disparate classes successfully reduced the potential of developed resistance to macrolides and also improved potency to erythromycin-resistant Gram-negative and Gram-positive bacteria[79,80]. It is possible that linking other classes of antibiotics may prove to be successful as well.

We explored linking a macrolide with an oxazolidinone or, in one case, chloramphenicol. These antibiotic classes bind beside each other in the ribosome: the NPET is the binding site of macrolides, and the A-site of the PTC is the binding site of oxazolidinones and chloramphenicol.

We synthesized several hybrid analogs (**Table 4.1, Fig. 4.5a**) and compared their activities to those of azithromycin, tedizolid, and desosamine in pathogenic strains of *S. aureus* as well as in cell-free translation assays (**Fig. 4.5b**). Curiously, we saw a broad trend where SLC analogs that demonstrated improved translation inhibition in vitro exhibited a higher minimum inhibitory concentration (MIC), and vice versa, when compared to azithromycin and tedizolid. For example, of all compounds tested, SLC09 demonstrated the weakest inhibitor activity in vitro but had the lowest MIC. Contrastly, SLC21 demonstrated the improved inhibitor activity in vitro compared to azithromycin but was not active in cells. Perhaps an exception to this trend is SLC30, which inhibited translation in vitro more effectively than tedizolid and desosamine alone but showed no improvements in cellular activity compared to tedizolid. Surprisingly, SLC30 was more active in cells (0.5-0.25 μg/mL) than its unprotected counterpart, SLC31 (4-16 μg/mL). To better understand these results, we then examined the binding poses of our SLC analogs in the *E. coli* ribosome using Cryo-EM.

Table 4.1. Description of hybrid analogs explored via Cryo-EM. Where applicable, the macrolide-like and oxazolidinone-like regions that make up each compound are listed. *Chloramphenicol is in the phenicol family of antibiotics.

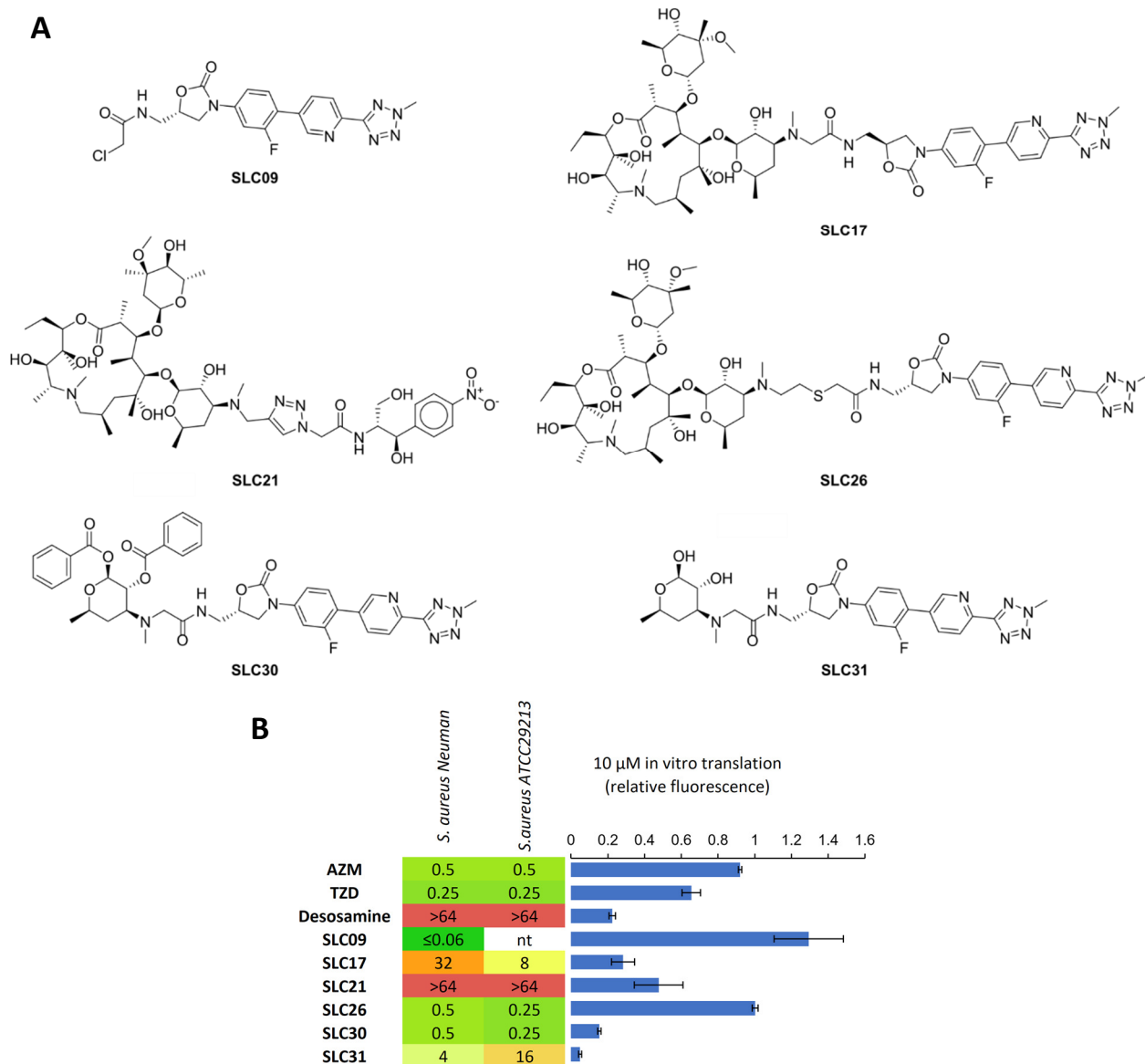| Analog	Macrolide	Oxazolidinone
SLC09	N/A	tedizolid
SLC17	azithromycin	tedizolid
SLC21	azithromycin	chloramphenicol*
SLC26	azithromycin	tedizolid
SLC30	benzoyl-protected desosamine	tedizolid
SLC31	desosamine	tedizolid

Figure 4.5. MIC and in vitro translation activity of SLC compounds. **(A)** Hybrid SLC analogs containing macrolide-like and/or oxazolidinone-like groups. **(B)** Minimum inhibitory concentration (MIC) values in μg/mL for azithromycin (AZM), tedizolid (TZD), desosamine, and SLC analogs against *S. aureus* pathogens. Each MIC was obtained in technical triplicate. Where present, nt indicates the analog was not tested against the strain in question. The bars to the right display in vitro translation that occurs in the presence of 10 μM of each analog, relative to dimethylsulfoxide (DMSO). Error bars denote s.d. (3 technical replicates).

With the exception of SLC21, all of our SLC compounds contain a tedizolid

oxazolidinone region. Several key residues that comprise the binding site for oxazolidinones

have been identified[81]. Of these, the strong hydrogen bonding network made between the

oxazolidinone and G2061, G2505, and A2451 are maintained by all tedizolid-containing SLC

compounds. SLC09, which is a chlorinated tedizolid analog, maintains all the key contacts. Compared to the tedizolid bound to the ribosome of methicillin resistant *S. aureus* (PDB: 6WRS[81]), the additional appendage on SLC09 affords additional hydrogen bonds with G2505 and one alternate conformation of A2062 (**Fig. 4.6a**). This may explain the improvements in MIC we observed for SLC09 in *S. aureus* (≤0.06 μg/mL) compared to tedizolid (0.25 μg/mL).
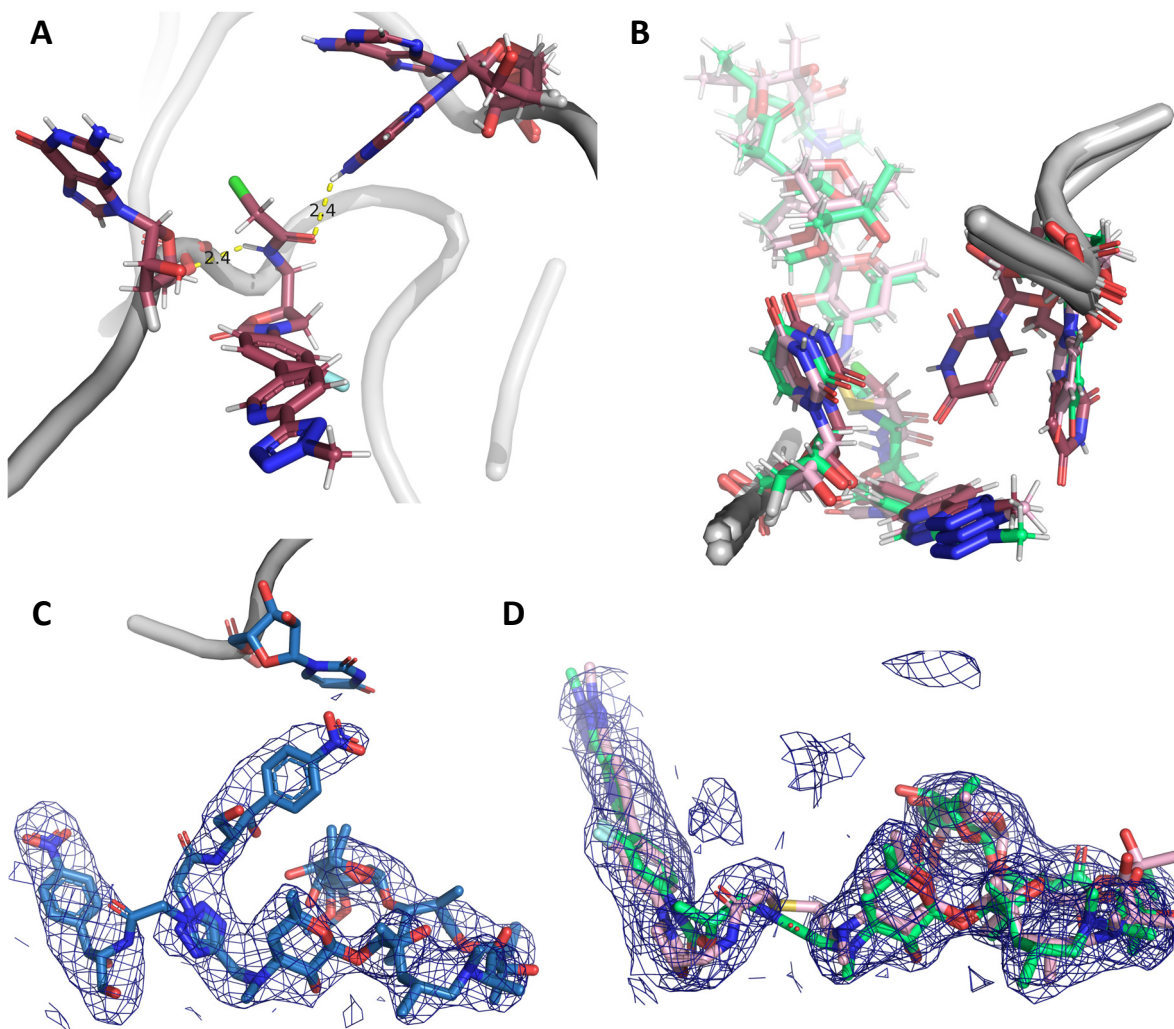

Figure 4.6. Ribosome binding of SLC09 and azithromycin-containing SLC compounds. **(A)** The chlorinated analog of tedizolid, SLC09, exhibits additional hydrogen bonding contacts with G2505 (left) and one conformation of A2062 (right) at the new appendage. **(B)** SLC09 (deep red) exhibits hydrogen bonding potential with U2506 (left) and U2585 (right), which is lost in azithromycin-containing analogs SLC26 (light pink) and SLC17 (bright green). **(C)** The chloramphenicol region of SLC21 adopts two alternate conformations. The 2.32-Å Cryo-EM Coulomb potential density map (contoured at 1.0σ) shows a break in density for one conformation, in which the chloramphenicol region adopts its putative pose. In the alternate pose, the chloramphenicol engages U2586. **(D)** Cryo-EM Coulomb potential density maps (contoured at 1.0σ) show a break in density between the tedizolid and azithromycin regions of SLC26 (light pink; 2.32 Å) and SLC17 (bright green; 2.30 Å).

SLC26, which bares an azithromycin group with a linker in place of the chlorine, closely matches the pose of SLC09. However, contacts between the A-ring and B-ring of the tedizolid region in SLC26 and U2585 and U2506, respectively, are disturbed (**Fig. 4.6b**). This trend is also observed for SLC17, which is akin to SLC26 but with a shorter linker. These residues appear to slightly retreat from the ligand, which could be due to the presence of the bulky azithromycin group, although the connection is unclear. As neither of these residues are recorded as core stabilizers for oxazolidinone efficacy[81], it is possible that loss of these contacts does not significantly affect the activity of these analogs. Therefore, our structural data for SLC17 and SLC26 do not explain the incongruent trends observed in MIC and in vitro translation inhibition of these analogs.

Interestingly, SLC21 exhibits two conformations for the chloramphenicol region. One of these conformations is in the putative binding pocket of chloramphenicol, while the other adopts a binding pose nearly 90 degrees rotated that engages U2586 (**Fig. 4.6c**). While both poses are well supported by the density (2.32-Å resolution), it is possible that this novel pose is the major conformation for SLC21, as there are no breaks in its density. Weak density is also observed at the linking region for the other azithromycin-containing analogs (**Fig. 4.6d**). Despite these interesting structural observations, SLC21 did not exhibit activity in either of the *S. aureus* strains tested. Considering the modest ribosomal inhibition that SLC21 induced in vitro, it is probable the high MIC of this compound is due to poor uptake and/or retention in the cell.

In contrast with these azithromycin-containing analogs, SLC30 and SLC31 contain only the first desosamine sugar of the macrolide. We anticipated that this desosamine would adopt the same pose as we observed in the azithromycin-containing analogs. Unfortunately, the density for SLC30 (2.27-Å resolution) was too weak to support modeling of the ligand's benzyl-protected desosamine (**Fig. 4.7a**). However, the direction in which the molecule bends suggests the sugar would not be in the same position as in the azithromycin-containing analogs. We can

better observe this in SLC31, which adopts a pose akin to SLC30 and whose 2.05-Å resolution

density does not support our prediction for where the sugar would sit (**Fig. 4.7b**).
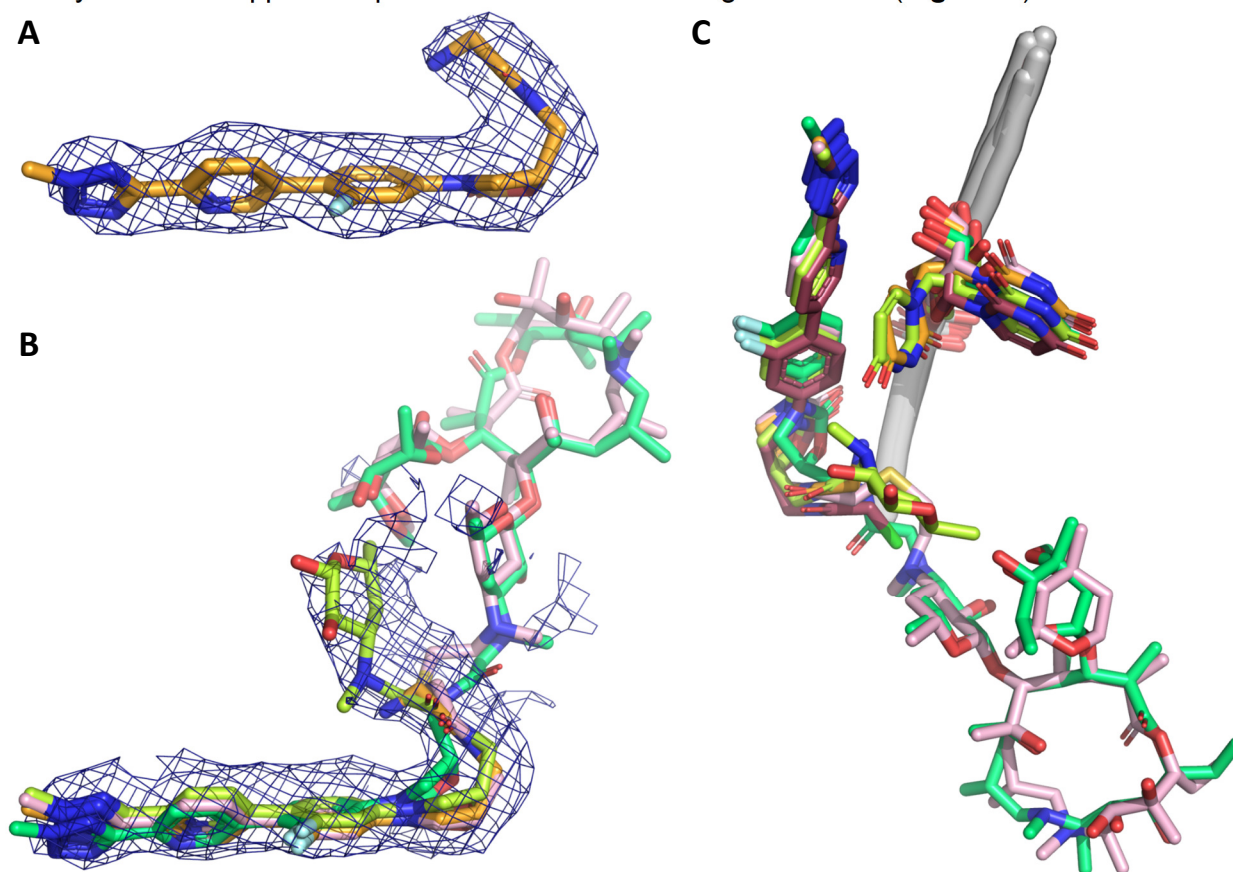

Figure 4.7. Ribosome binding of desosamine-containing SLC compounds. **(A)** The 2.27-Å Cryo-EM Coulomb potential density map (contoured at 1.0σ) does not show any density for the benzyl-protected desosamine of SLC30. **(B)** The desosamine of SLC31 (lime green) does not adopt the same binding pose as in the azithromycin-containing analogs SLC17 (bright green) and SLC26 (light pink). SLC30 (orange) is shown for comparison. The 2.05-Å Cryo-EM Coulomb potential density map (contoured at 1.0σ) is shown for SLC31. **(C)** A2506 adopts a unique, alternate conformation only in the presence of SLC30 (orange) and SLC31 (lime green). Also depicted are SLC09 (deep red), SLC26 (light pink), and SLC17 (bright green).

Taking into consideration the observed activities of these two compounds, our structural

data serve to elucidate the trends seen in MIC and in vitro translation inhibition assays. We

hypothesize that the poor density for SLC30 could be due to either disorder in or instability of

the ligand. In turn, this could contribute to SLC30 being less effective at inhibiting translation in

vitro compared to SLC31, which appears to be better stabilized in the ribosome. These results,

however, do not explain why SLC30 exhibited excellent activity in *S. aureus* (0.5-0.25 µg/mL),

while SLC31 showed moderate activity (4-16 µg/mL). Further experiments will be necessary to

understand the uptake and bioavailability of these analogs in cells. Overall, these structural observations for SLC30 and SLC31 make designing similar analogs in the future more difficult, as the binding pose is not easily predicted. Of final note is that the *E. coli* ribosome with analogs SLC30 and SLC31 exhibits a unique, alternate conformation of A2506 that is not observed in any of the SLC analogs we tested (**Fig. 4.7c**). The significance and impact of this conformational change remains unclear.

Tiamulin and NPET-binding antibiotics

The rapidly growing threat of pathogens bearing multidrug resistance to commonly used antibacterials has revitalized interest in previously abandoned classes of antibiotics, such as pleuromutilins, which inhibit translation at the PTC. Although they share their mechanism of action with many other antibiotics, resistance to pleuromutilins has been shown to develop slowly[82,83], making this an attractive class to reevaluate. Further successes in developing derivatives, such as FDA-approved drugs retapamulin[84] and lefamulin[85], have shown significant strides in decreasing the toxicity and improving the bioavailability of the pleuromutilin class, which has historically had limited clinical use in humans. Interestingly, some pleuromutilin derivatives have been shown to synergize with unconventional binding partners, such as doxycycline[86] and tetracycline[87], which bind in the small subunit of the ribosome. Inspired by this and by our ongoing work studying analogs of the natural synergistic pair SA and SB, we chose to investigate if structurally biology could support the potential of pleuromutilins to synergize with NPET-binding partners.

We first sought to investigate conformational changes in the *E. coli* ribosome with the semisynthetic pleuromutilin derivative tiamulin and VS1, a natural SB. Our high-resolution Cryo-EM model (2.13 Å) reveals most notably that residue A2062 flips down to fit between the two antibiotics, engaging in pi-pi stacking with VS1 (**Fig. 4.8a**). This conformational change in A2062, induced by SA binding, is credited for increasing affinity of SB binding, contributing to

synergy[9]. From this observation with tiamulin and VS1, it is possible that tiamulin may act similarly. However, comparing the pose of A2062 in *E. coli* and *H. marismortui*, we observe conformational change induced by VM2 alone but not by tiamulin alone in *H. marismortui* (**Fig. 4.8a**). Therefore, while tiamulin may still synergize with VS1 when both molecules are present, the mode of action is not clear.
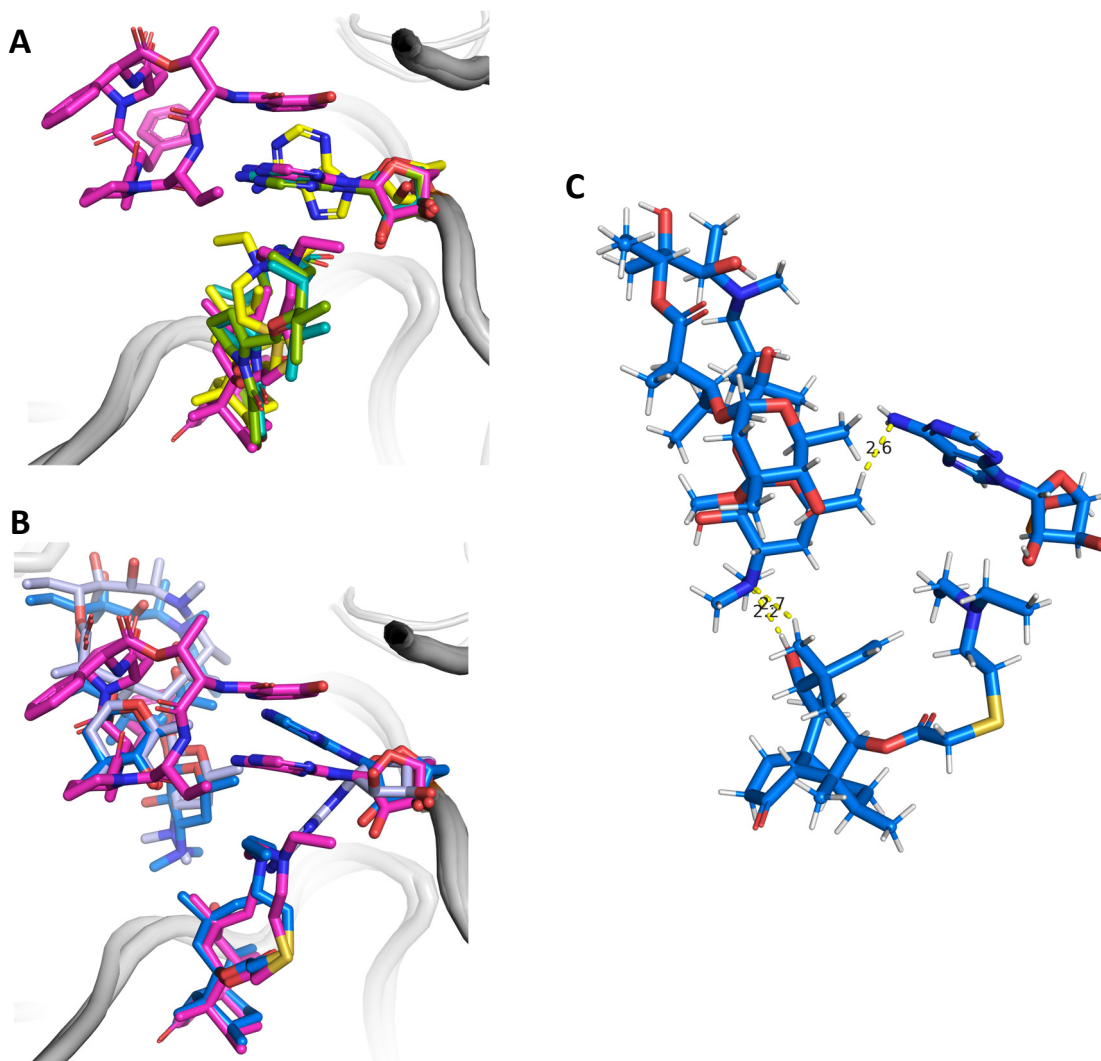
Figure 4.8. Ribosome binding of tiamulin and NPET binders. **(A)** Overlay of the *E. coli* ribosome with tiamulin and VS1 bound (magenta) and with VM2 bound (green; PDB: 6PCQ) and of the *H. marismortui* ribosome with tiamulin bound (yellow; PDB: 3G4S[88]) and with VM2 bound (teal; PDB: 1N8R[33]). Residue A2062 occupies the same position in all cases except for where tiamulin binds the ribosome alone. **(B)** The *E. coli* ribosome with tiamulin and VS1 bound (magenta) and with tiamulin and VS1 bound (blue marine) overlaid with the *H. marismortui* ribosome with azithromycin bound (light blue; PDB: 1M1K[89]). Residue A2062 adopts a unique pose in the presence of both tiamulin and azithromycin that **(C)** allows it to hydrogen bond with azithromycin. Further, the azithromycin and tiamulin molecules bind closely enough to hydrogen bond as well.

We were also curious to see if tiamulin could introduce conformational changes that might induce synergy with non-SB molecules. Therefore, we obtained a Cryo-EM model (2.29 Å) of tiamulin bound with azithromycin, a macrolide. Here, we observed that A2062 adopts a unique pose when compared to the ribosome structures of *E. coli* with tiamulin+VS1 and *H. marismortui* with azithromycin bound alone (**Fig. 4.8b**). A2062 adopts a pose similar to in tiamulin+VS1, although angled approximately away from tiamulin such that it makes hydrogen bonds with azithromycin (**Fig. 4.8c**). Furthermore, tiamulin and azithromycin bind close enough to interact through a network of hydrogen bonds (**Fig. 4.8c**). We hypothesize that these strong interactions could potentiate a synergistic relationship between the two molecules.

Methods

MIC testing

Compounds were evaluated by Microbiologics, Inc. as described in Chapter 1.

In vitro translation assay 10-µM screen

The ability of antibiotic compounds to inhibit the 70S *E. coli* ribosome was performed as described in Chapter 1.

Cryo-EM sample preparation, data collection, and data processing

Cryo-EM samples were prepared as described in Chapter 3. All datasets were collected on FEI Titan Krios electron microscopes (ThermoFisher, operating at 300 kV, located at UCSF, PNCC, or NCCAT). Automated data collection at UCSF and PNCC was facilitated by SerialEM (v3.6)[53]; collection at NCCAT was via Leginon (v.3.4)[54]. All data sets were collected on a K3 (Gatan) Direct Electron Detector (DED) with a Gatan Imaging Filter (Gatan, 20 eV slit) nine-shot beam-image shift approach with coma compensation[55]. Pixel sizes, number of images in dose-fractionated micrographs, dose rates, and defocus ranges varied slightly and are reported in

Tables 4.2-5, along with the final high-resolution limits used. Image stacks were collected in super-resolution mode. Datasets were processed as described in Chapter 1.

Cryo-EM model building and refinement with OPLS3e

Initial *E. coli* ribosome models were obtained as described in Chapter 3. Ligands were by using the SMILES string and a 'final geometry' reference PDB of the nearest homologous antibiotic to the analog. Structures were refined as described in Chapter 1 using versions 1.17 and 1.19 of the PHENIX suite. For all Cryo-EM figures, the full, unsharpened density maps and full PDB models were boxed using phenix.map_box with a selection radius of 20 Å around the ligand(s). Boxed map and model were loaded into PyMol (incentive v.2.4.1) and contoured at 4.0σ, centered around the ligand(s) with a carve of 1.4, unless otherwise specified.

Liquid chromatography-mass spectrometry (LCMS)

Purified 50S ribosomes from *E. coli* strain MRE600 were prepared in 50 mM HEPES pH 7.5, 150 mM potassium acetate, 6 mM magnesium acetate, and 7 mM fresh β-mercaptoethanol (BME) and treated with 60 μM of either L- or D-linker solithromycin conjugate. Stock solutions were mixed and incubated for 8 hours prior to LCMS analysis in triplicate. A control sample was prepared in the same fashion but without ribosomes. Following incubation, samples were filtered using AmiconUltra 0.5 centrifugal filter units to remove the ribosomes from the filtrate. The filtrate was then diluted 50% with 99% acetonitrile/0.9% H_2O/0.1% formic acid and injected onto the LCMS C18 column and analyzed in MassLynx.

Author Contributions

J.P. and D.J.L. prepared samples and collected Cryo-EM data; J.P. calculated Cryo-EM reconstructions; J.P. performed Cryo-EM model refinements; J.P. performed the in vitro translation experiments for streptogramin A analogs; Q.L. executed and optimized the

syntheses of streptogramin A analogs; J.H.B. executed and optimized the syntheses of L- and D-linker solithromycin conjugates; A.K.E. performed LCMS for the L- and D-linker solithromycin conjugates; S.K.Y. executed and optimized the syntheses of hybrid macrolide/oxazolidinone molecules; S.K.Y. performed the in vitro translation experiments for hybrid macrolide/oxazolidinone molecules and complementary compounds; Q.E. initiated exploration of tiamulin bound with NPET-binding antibiotics; J.P. and A.K.E. wrote observations for L- and D-linker solithromycin conjugates; J.P. wrote observations for all other structures; I.B.S. assisted with designing synthetic routes; J.S.F. assisted with experimental design and edited the manuscript.

Extended Data

Table 4.2. Cryo-EM data collection, processing, and model refinement statistics for structures associated with streptogramin A analogs.

	3057	3142	3146
PDB code		8E30	8E36
EMDB		EMD-27852	EMD-27858
EM data collection / processing			
Microscope	FEI Titan Krios	FEI Titan Krios	FEI Titan Krios
Voltage (kV)	300	300	300
Camera	Gatan K3	Gatan K3	Gatan K3
Electron exposure (e-/Å^2)	2.353	76.38	59.59
Defocus range (μm)	0.3 - 0.8	0.3 - 1.0	0.3 - 1.0
Pixel size (Å)	0.8488	0.8261	0.8488
Symmetry imposed	C1	C1	C1
Total number of micrographs	4601	6488	2734
Number of good micrographs	3496	6352	2469
Particles picked from all micrographs	767432	1042915	450369
Particles from good micrographs	577282	1021078	411257
Particles used in final reconstruction	299109	597411	183917
Map resolution (Å)	2.58	1.91	2.38
FSC threshold	0.143	0.143	0.143
High resolution refinement limit (Å)	3.2	3.0	3.0
Refinement			
Initial model used (PDB code)	4YBB	4YBB	4YBB
Model resolution (Å)	2.9	2.2	2.8
FSC threshold	0.5	0.5	0.5
Map sharpening B factor (Å^2)	0	0	0
Model composition			
Total atoms	115950	116064	116040
Hydrogens only	42093	42147	42137
Non-hydrogen atoms	73857	73917	73903
Protein residues	1179	1179	1179
Nucleotide residues	3016	3016	3015
Ligands	1	1	1
B factors (Å^2), mean			
Protein	82.77	68.89	79.5
Nucleotide	98.18	82.98	95.43
Ligand	55.92	62.45	71.85
R.m.s. deviations			
Bond lengths (Å) (# >4sigma)	0.002 (0)	0.002 (0)	0.002 (0)
Bond angles (°) (# >4sigma)	0.292 (2)	0.395 (16)	0.294 (0)
Validation			
MolProbity score	1.33	1.34	1.3
Clash score	2.22	2	2.26
Rotamer outliers (%)	0	0.64	0.32
Ramachandran plot			
Favored (%)	95.27	94.5	95.79
Allowed (%)	4.73	5.33	4.21
Outliers (%)	0	0.17	0
Cβ outliers (%)	0	0	0

Table 4.3. Cryo-EM data collection, processing, and model refinement statistics for structures associated with D- and L-linker solithromycin conjugates and solithromycin+VM1.

	D-linker	L-linker	Soli+VM1
PDB code	8E3L	8E3M	8E3O
EMDB	EMD-27867	EMD-27868	EMD-27869
EM data collection / processing			
Microscope	FEI Titan Krios	FEI Titan Krios	FEI Titan Krios
Voltage (kV)	300	300	300
Camera	Gatan K3	Gatan K3	Gatan K3
Electron exposure (e-/Å^2)	69	58	35.704
Defocus range (µm)	0.4 - 1.0	0.4 - 1.6	0.5 - 1.3
Pixel size (Å)	0.665	0.830	0.648
Symmetry imposed	C1	C1	C1
Total number of micrographs	1864	2584	7721
Number of good micrographs	1763	2558	7502
Particles picked from all micrographs	170246	429354	763795
Particles from good micrographs	160782	425058	741839
Particles used in final reconstruction	105104	250098	401340
Map resolution (Å)	2.35	2.25	1.99
FSC threshold	0.143	0.143	0.143
High resolution refinement limit (Å)	3.5	3.2	2.8
Refinement			
Initial model used (PDB code)			
Model resolution (Å)	2.8	2.7	2.4
FSC threshold	0.5	0.5	0.5
Map sharpening B factor (Å^2)	0	0	0
Model composition			
Total atoms	116117	116034	116037
Hydrogens only	42178	42134	42144
Non-hydrogen atoms	73939	73900	73893
Protein residues	1179	1179	1179
Nucleotide residues	3015	3016	3015
Ligands	1	1	2
B factors (Å^2), mean			
Protein	65.72	64.26	67.19
Nucleotide	80.39	83.49	78.71
Ligand	47.32	90.68	52.62
R.m.s. deviations			
Bond lengths (Å) (# >4sigma)	0.002 (0)	0.003 (16)	0.002 (0)
Bond angles (°) (# >4sigma)	0.313 (0)	0.361 (7)	0.336 (0)
Validation			
MolProbity score	1.2	1.33	1.36
Clash score	1.23	2.01	2.36
Rotamer outliers (%)	0.74	1.27	0.74
Ramachandran plot			
Favored (%)	94.75	95.96	95.1
Allowed (%)	5.16	4.04	4.56
Outliers (%)	0.09	0	0.34
Cβ outliers (%)	0	0	0

Table 4.4. Cryo-EM data collection, processing, and model refinement statistics for structures associated with SLC analogs.

	SLC09	SLC17	SLC21
PDB code	8E44	8E45	8E46
EMDB	EMD-27879	EMD-27880	EMD-27881
EM data collection / processing			
Microscope	FEI Titan Krios	FEI Titan Krios	FEI Titan Krios
Voltage (kV)	300	300	300
Camera	Gatan K3	Gatan K3	Gatan K3
Electron exposure (e-/Å^2)	67	58	58
Defocus range (μm)	0.4 - 1.2	0.5 - 1.3	0.5 - 1.3
Pixel size (Å)	0.8261	0.525	0.525
Symmetry imposed	C1	C1	C1
Total number of micrographs	2202	3342	3699
Number of good micrographs	1855	3037	3586
Particles picked from all micrographs	307504	236284	276279
Particles from good micrographs	259069	214734	267868
Particles used in final reconstruction	133237	109682	103742
Map resolution (Å)	2.53	2.3	2.32
FSC threshold	0.143	0.143	0.143
High resolution refinement limit (Å)	3.0	3.5	3.2
Refinement			
Initial model used (PDB code)	4YBB	4YBB	4YBB
Model resolution (Å)	2.9	2.8	2.8
FSC threshold	0.5	0.5	0.5
Map sharpening B factor (Å^2)	0	0	0
Model composition			
Total atoms	116106	116069	116158
Hydrogens only	42133	42151	42213
Non-hydrogen atoms	73973	73918	73945
Protein residues	1179	1179	1179
Nucleotide residues	3016	3015	3015
Ligands	1	1	1
B factors (Å^2), mean			
Protein	67.71	71.45	70.12
Nucleotide	83.11	86.86	85.26
Ligand	56.79	60.36	57.5
R.m.s. deviations			
Bond lengths (Å) (# >4sigma)	0.002 (0)	0.001 (1)	0.001 (0)
Bond angles (°) (# >4sigma)	0.333 (18)	0.296 (10)	0.296 (2)
Validation			
MolProbity score	1.32	1.18	1.22
Clash score	2.19	1.32	1.36
Rotamer outliers (%)	0.11	0.74	0.53
Ramachandran plot			
Favored (%)	95.36	95.36	94.84
Allowed (%)	4.64	4.47	5.07
Outliers (%)	0	0.17	0.09
Cβ outliers (%)	0	0	0

Table 4.4 continued

	SLC26	SLC30	SLC31
PDB code	8E47	8E48	8E49
EMDB	EMD-27882	EMD-27883	EMD-27884
EM data collection / processing			
Microscope	FEI Titan Krios	FEI Titan Krios	FEI Titan Krios
Voltage (kV)	300	300	300
Camera	Gatan K3	Gatan K3	Gatan K3
Electron exposure (e-/Å^2)	47.2	47.2	45.8
Defocus range (μm)	0.6 - 1.6	0.6 - 1.6	0.6 - 1.6
Pixel size (Å)	0.665	0.665	0.8261
Symmetry imposed	C1	C1	C1
Total number of micrographs	7503	8748	4632
Number of good micrographs	6327	8295	4029
Particles picked from all micrographs	685297	889305	700316
Particles from good micrographs	653246	843396	613563
Particles used in final reconstruction	394223	556086	305897
Map resolution (Å)	2.32	2.27	2.05
FSC threshold	0.143	0.143	0.143
High resolution refinement limit (Å)	3.5	3.5	3.5
Refinement			
Initial model used (PDB code)	4YBB	4YBB	4YBB
Model resolution (Å)	2.6	2.5	2.5
FSC threshold	0.5	0.5	0.5
Map sharpening B factor (Å^2)	0	0	0
Model composition			
Total atoms	116240	116212	116136
Hydrogens only	42209	42171	42150
Non-hydrogen atoms	74031	74041	73986
Protein residues	1179	1179	1179
Nucleotide residues	3016	3016	3016
Ligands	1	1	1
B factors (Å^2), mean			
Protein	64.53	75.79	65.51
Nucleotide	82.95	91.86	79.37
Ligand	50.14	64.22	59.56
R.m.s. deviations			
Bond lengths (Å) (# >4sigma)	0.001 (0)	0.002 (4)	0.002 (0)
Bond angles (°) (# >4sigma)	0.309 (13)	0.474 (27)	0.316 (4)
Validation			
MolProbity score	1.07	1.16	1.17
Clash score	1.08	1.19	1.3
Rotamer outliers (%)	0.96	0.53	0.85
Ramachandran plot			
Favored (%)	96.13	95.36	95.44
Allowed (%)	3.87	4.64	4.56
Outliers (%)	0	0	0
Cβ outliers (%)	0	0	0

Table 4.5. Cryo-EM data collection, processing, and model refinement statistics for structures associated with tiamulin and NPET-binding antibiotics.

	tiamulin+azith	tiamulin+VS1
PDB code	8E42	8E41
EMDB	EMD-27877	EMD-27876
EM data collection / processing		
Microscope	FEI Titan Krios	FEI Titan Krios
Voltage (kV)	300	300
Camera	Gatan K3	Gatan K3
Electron exposure (e-/Å^2)	58	23.45
Defocus range (µm)	0.4 - 1.6	0.5 - 1.3
Pixel size (Å)	0.830	0.8261
Symmetry imposed	C1	C1
Total number of micrographs	2272	2520
Number of good micrographs	2256	2366
Particles picked from all micrographs	394207	389004
Particles from good micrographs	391455	365393
Particles used in final reconstruction	232250	192760
Map resolution (Å)	2.29	2.13
FSC threshold	0.143	0.143
High resolution refinement limit (Å)	3.0	3.0
Refinement		
Initial model used (PDB code)		
Model resolution (Å)	2.7	2.6
FSC threshold	0.5	0.5
Map sharpening *B* factor (Å^2)	0	0
Model composition		
Total atoms	116083	116060
Hydrogens only	42180	42149
Non-hydrogen atoms	73903	73911
Protein residues	1179	1179
Nucleotide residues	3016	3016
Ligands	2	2
B factors (Å^2), mean		
Protein	71.16	72.71
Nucleotide	85.03	86.78
Ligand	61.86	54.62
R.m.s. deviations		
Bond lengths (Å) (# >4sigma)	0.002 (2)	0.002 (1)
Bond angles (°) (# >4sigma)	0.316 (0)	0.302 (0)
Validation		
MolProbity score	1.23	1.32
Clash score	1.92	1.91
Rotamer outliers (%)	0.53	0.85
Ramachandran plot		
Favored (%)	96.04	94.75
Allowed (%)	3.96	5.25
Outliers (%)	0	0
Cβ outliers (%)	0	0

References

1. Wright, P. M., Seiple, I. B. & Myers, A. G. The evolving role of chemical synthesis in antibacterial drug discovery. *Angew. Chem. Int. Ed Engl.* **53**, 8840–8869 (2014).

2. Stogios, P. J. *et al.* Potential for reduction of streptogramin A resistance revealed by structural analysis of acetyltransferase VatA. *Antimicrob. Agents Chemother.* **58**, 7083–7092 (2014).

3. Vazquez, D. The Streptogramin Family of Antibiotics. in *Mechanism of Action* (eds. Gottlieb, D. & Shaw, P. D.) 387–403 (Springer Berlin Heidelberg, 1967).

4. Waglechner, N. & Wright, G. D. Antibiotic resistance: it's bad, but why isn't it worse? *BMC Biol.* **15**, 84 (2017).

5. Seiple, I. B. *et al.* A platform for the discovery of new macrolide antibiotics. *Nature* **533**, 338–345 (2016).

6. Charest, M. G., Lerner, C. D., Brubaker, J. D., Siegel, D. R. & Myers, A. G. A convergent enantioselective route to structurally diverse 6-deoxytetracycline antibiotics. *Science* **308**, 395–398 (2005).

7. Vidaillac, C., Parra-Ruiz, J., Winterfield, P. & Rybak, M. J. In vitro pharmacokinetic/pharmacodynamic activity of NXL103 versus clindamycin and linezolid against clinical Staphylococcus aureus and Streptococcus pyogenes isolates. *Int. J. Antimicrob. Agents* **38**, 301–306 (2011).

8. Wilson, D. N. The A-Z of bacterial translation inhibitors. *Crit. Rev. Biochem. Mol. Biol.* **44**, 393–433 (2009).

9. Noeske, J. *et al.* Synergy of streptogramin antibiotics occurs independently of their effects on translation. *Antimicrob. Agents Chemother.* **58**, 5269–5279 (2014).

10. Hershberger, E., Donabedian, S., Konstantinou, K. & Zervos, M. J. Quinupristin-dalfopristin resistance in gram-positive bacteria: mechanism of resistance and epidemiology. *Clin. Infect. Dis.* **38**, 92–98 (2004).

11. Sharkey, L. K. R. & O'Neill, A. J. Antibiotic Resistance ABC-F Proteins: Bringing Target Protection into the Limelight. *ACS Infect Dis* **4**, 239–246 (2018).

12. Leclercq, R. & Courvalin, P. Bacterial resistance to macrolide, lincosamide, and streptogramin antibiotics by target modification. *Antimicrob. Agents Chemother.* **35**, 1267–1272 (1991).

13. Haroche, J. *et al.* Clonal diversity among streptogramin A-resistant Staphylococcus aureus isolates collected in French hospitals. *J. Clin. Microbiol.* **41**, 586–591 (2003).

14. Werner, G., Cuny, C., Schmitz, F. J. & Witte, W. Methicillin-resistant, quinupristin-dalfopristin-resistant Staphylococcus aureus with reduced sensitivity to glycopeptides. *J. Clin. Microbiol.* **39**, 3586–3590 (2001).

15. Valour, F. *et al.* Pristinamycin in the treatment of MSSA bone and joint infection. *J. Antimicrob. Chemother.* **71**, 1063–1070 (2016).

16. Delgado, G., Jr, Neuhauser, M. M., Bearden, D. T. & Danziger, L. H. Quinupristin-dalfopristin: an overview. *Pharmacotherapy: The Journal of Human Pharmacology and Drug Therapy* **20**, 1469–1485 (2000).

17. Politano, A. D. & Sawyer, R. G. NXL-103, a combination of flopristin and linopristin, for the potential treatment of bacterial infections including community-acquired pneumonia and MRSA. *Curr. Opin. Investig. Drugs* **11**, 225–236 (2010).

18. Li, Q. & Seiple, I. B. Modular, Scalable Synthesis of Group A Streptogramin Antibiotics. *J. Am. Chem. Soc.* **139**, 13304–13307 (2017).

19. Li, Q. & Seiple, I. B. A concise route to virginiamycin M2. *Tetrahedron* **75**, 3309–3318 (2019).

20. Schlessinger, R. H. & Li, Y.-J. Total Synthesis of (−)-Virginiamycin M2 Using Second-Generation Vinylogous Urethane Chemistry. *J. Am. Chem. Soc.* **118**, 3301–3302 (1996).

21. Entwistle, D. A., Jordan, S. I., Montgomery, J. & Pattenden, G. Total synthesis of the virginiamycin antibiotic 14,15-anhydropristinamycin IIB. *J. Chem. Soc. Perkin 1* 1315–1317

(1996).

22. Tavares, F., Lawson, J. P. & Meyers, A. I. Total Synthesis of Streptogramin Antibiotics. (–)-Madumycin II. *J. Am. Chem. Soc.* **118**, 3303–3304 (1996).

23. Ghosh, A. K. & Liu, W. A Convergent, Enantioselective Total Synthesis of Streptogramin Antibiotic (-)-Madumycin II. *J. Org. Chem.* **62**, 7908–7909 (1997).

24. Breuilles, P. & Uguen, D. Total synthesis of pristinamycin IIB. *Tetrahedron Lett.* **39**, 3149–3152 (1998).

25. Entwistle, D. A. Total Synthesis of Oxazole-Based Virginiamycin Antibiotics: 14,15-Anhydropristinamycin IIB. *Synthesis* **1998**, 603–612 (1998).

26. Dvorak, C. A. *et al.* The Synthesis of Streptogramin Antibiotics:(-)-Griseoviridin and Its C-8 Epimer. *Angew. Chem. Int. Ed.* **39**, 1664–1666 (2000).

27. Wu, J. & Panek, J. S. Total synthesis of (-)-virginiamycin M2. *Angew. Chem. Int. Ed Engl.* **49**, 6165–6168 (2010).

28. Wu, J. & Panek, J. S. Total synthesis of (-)-virginiamycin M2: application of crotylsilanes accessed by enantioselective Rh(II) or Cu(I) promoted carbenoid Si-H insertion. *J. Org. Chem.* **76**, 9900–9918 (2011).

29. Afonine, P. V. *et al.* Real-space refinement in PHENIX for cryo-EM and crystallography. *Acta Crystallogr D Struct Biol* **74**, 531–544 (2018).

30. Li, J. *et al.* The VSGB 2.0 model: a next generation energy model for high resolution protein structure modeling. *Proteins* **79**, 2794–2812 (2011).

31. Harms, J. M., Schlünzen, F., Fucini, P., Bartels, H. & Yonath, A. Alterations at the peptidyl transferase centre of the ribosome induced by the synergistic action of the streptogramins dalfopristin and quinupristin. *BMC Biol.* **2**, 4 (2004).

32. Osterman, I. A. *et al.* Madumycin II inhibits peptide bond formation by forcing the peptidyl transferase center into an inactive state. *Nucleic Acids Res.* **45**, 7507–7514 (2017).

33. Hansen, J. L., Moore, P. B. & Steitz, T. A. Structures of five antibiotics bound at the peptidyl

transferase center of the large ribosomal subunit. *J. Mol. Biol.* **330**, 1061–1075 (2003).

34. Tu, D., Blaha, G., Moore, P. B. & Steitz, T. A. Structures of MLSBK antibiotics bound to mutated large ribosomal subunits provide a structural explanation for resistance. *Cell* **121**, 257–270 (2005).

35. Hoang, N. H. *et al.* Regio-selectively reduced streptogramin A analogue, 5,6-dihydrovirginiamycin M1 exhibits improved potency against MRSA. *Lett. Appl. Microbiol.* **57**, 393–398 (2013).

36. Kingston, D. G. I., Kolpak, M. X., LeFevre, J. W. & Borup-Grochtmann, I. Biosynthesis of antibiotics of the virginiamycin family. 3. Biosynthesis of virginiamycin M1. *J. Am. Chem. Soc.* **105**, 5106–5110 (1983).

37. Richter, M. F. *et al.* Predictive compound accumulation rules yield a broad-spectrum antibiotic. *Nature* **545**, 299–304 (2017).

38. Sharkey, L. K. R., Edwards, T. A. & O'Neill, A. J. ABC-F Proteins Mediate Antibiotic Resistance through Ribosomal Protection. *MBio* **7**, e01975 (2016).

39. Radika, K. & Northrop, D. B. Correlation of antibiotic resistance with Vmax/Km ratio of enzymatic modification of aminoglycosides by kanamycin acetyltransferase. *Antimicrob. Agents Chemother.* **25**, 479–482 (1984).

40. Knies, J. L., Cai, F. & Weinreich, D. M. Enzyme Efficiency but Not Thermostability Drives Cefotaxime Resistance Evolution in TEM-1 β-Lactamase. *Mol. Biol. Evol.* **34**, 1040–1054 (2017).

41. Polikanov, Y. S., Steitz, T. A. & Innis, C. A. A proton wire to couple aminoacyl-tRNA accommodation and peptide-bond formation on the ribosome. *Nat. Struct. Mol. Biol.* **21**, 787–793 (2014).

42. Renaud, J.-P. *et al.* Cryo-EM in drug discovery: achievements, limitations and prospects. *Nat. Rev. Drug Discov.* **17**, 471–492 (2018).

43. Wong, W. *et al.* Mefloquine targets the Plasmodium falciparum 80S ribosome to inhibit

protein synthesis. *Nat Microbiol* **2**, 17031 (2017).

44. Llano-Sotelo, B. *et al.* Binding and action of CEM-101, a new fluoroketolide antibiotic that inhibits protein synthesis. *Antimicrob. Agents Chemother.* **54**, 4961–4970 (2010).

45. Tropea, J. E., Cherry, S. & Waugh, D. S. Expression and purification of soluble His(6)-tagged TEV protease. *Methods Mol. Biol.* **498**, 297–307 (2009).

46. Kuhn, M. L., Majorek, K. A., Minor, W. & Anderson, W. F. Broad-substrate screen as a tool to identify substrates for bacterial Gcn5-related N-acetyltransferases with unknown substrate specificity. *Protein Sci.* **22**, 222–230 (2013).

47. Winter, G. xia2: an expert system for macromolecular crystallography data reduction. *Journal of Applied Crystallography* vol. 43 186–190 (2010).

48. Kabsch, W. XDS. *Acta Crystallogr. D Biol. Crystallogr.* **66**, 125–132 (2010).

49. Liebschner, D. *et al.* Macromolecular structure determination using X-rays, neutrons and electrons: recent developments in Phenix. *Acta Crystallogr D Struct Biol* **75**, 861–877 (2019).

50. Emsley, P., Lohkamp, B., Scott, W. G. & Cowtan, K. Features and development of Coot. *Acta Crystallogr. D Biol. Crystallogr.* **66**, 486–501 (2010).

51. Schuwirth, B. S. *et al.* Structures of the bacterial ribosome at 3.5 A resolution. *Science* **310**, 827–834 (2005).

52. Passmore, L. A. & Russo, C. J. Specimen Preparation for High-Resolution Cryo-EM. *Methods Enzymol.* **579**, 51–86 (2016).

53. Mastronarde, D. N. Automated electron microscope tomography using robust prediction of specimen movements. *J. Struct. Biol.* **152**, 36–51 (2005).

54. Suloway, C. *et al.* Automated molecular microscopy: the new Leginon system. *J. Struct. Biol.* **151**, 41–60 (2005).

55. Cheng, A. *et al.* High resolution single particle cryo-electron microscopy using beam-image shift. *J. Struct. Biol.* **204**, 270–275 (2018).

56. Zheng, S. Q. *et al.* MotionCor2: anisotropic correction of beam-induced motion for improved cryo-electron microscopy. *Nature Methods* vol. 14 331–332 (2017).

57. Grant, T., Rohou, A. & Grigorieff, N. TEM, user-friendly software for single-particle image processing. *Elife* **7**, (2018).

58. Pettersen, E. F. *et al.* UCSF Chimera--a visualization system for exploratory research and analysis. *J. Comput. Chem.* **25**, 1605–1612 (2004).

59. Noeske, J. *et al.* High-resolution structure of the Escherichia coli ribosome. *Nat. Struct. Mol. Biol.* **22**, 336–341 (2015).

60. Moriarty, N. W., Grosse-Kunstleve, R. W. & Adams, P. D. electronic Ligand Builder and Optimization Workbench (eLBOW): a tool for ligand coordinate and restraint generation. *Acta Crystallogr. D Biol. Crystallogr.* **65**, 1074–1080 (2009).

61. Roos, K. *et al.* OPLS3e: Extending Force Field Coverage for Drug-Like Small Molecules. *J. Chem. Theory Comput.* **15**, 1863–1874 (2019).

62. Sindhikara, D. *et al.* Improving Accuracy, Diversity, and Speed with Prime Macrocycle Conformational Sampling. *J. Chem. Inf. Model.* **57**, 1881–1894 (2017).

63. Bochevarov, A. D. *et al.* Jaguar: A high-performance quantum chemistry software program with strengths in life and materials sciences. *International Journal of Quantum Chemistry* vol. 113 2110–2142 (2013).

64. Cox, G. *et al.* A Common Platform for Antibiotic Dereplication and Adjuvant Discovery. *Cell Chem Biol* **24**, 98–109 (2017).

65. Barik, S. The Uniqueness of Tryptophan in Biology: Properties, Metabolism, Interactions and Localization in Proteins. *Int. J. Mol. Sci.* **21**, (2020).

66. Situ, A. J. *et al.* Membrane Anchoring of α-Helical Proteins: Role of Tryptophan. *J. Phys. Chem. B* **122**, 1185–1194 (2018).

67. The role of tryptophan side chains in membrane protein anchoring and hydrophobic mismatch. *Biochimica et Biophysica Acta (BBA) - Biomembranes* **1828**, 864–876 (2013).

68. Glassford, I. *et al.* Ribosome-Templated Azide-Alkyne Cycloadditions: Synthesis of Potent Macrolide Antibiotics by In Situ Click Chemistry. *J. Am. Chem. Soc.* **138**, 3136–3144 (2016).

69. Grimme, S. Exploration of Chemical Compound, Conformer, and Reaction Space with Meta-Dynamics Simulations Based on Tight-Binding Quantum Chemical Calculations. *J. Chem. Theory Comput.* **15**, 2847–2862 (2019).

70. Pracht, P., Bohle, F. & Grimme, S. Automated exploration of the low-energy chemical space with fast quantum chemical methods. *Phys. Chem. Chem. Phys.* **22**, 7169–7192 (2020).

71. Frisch, M. J. *et al.* Gaussian 16 (Revision A.03), Gaussian Inc., Wallingford, CT, 2016.

72. Becke, A. D. Density-functional thermochemistry. III. The role of exact exchange. *J. Chem. Phys.* **98**, 5648–5652 (1993).

73. Grimme, S., Antony, J., Ehrlich, S. & Krieg, H. A consistent and accurate ab initio parametrization of density functional dispersion correction (DFT-D) for the 94 elements H-Pu. *J. Chem. Phys.* **132**, 154104 (2010).

74. Grimme, S., Ehrlich, S. & Goerigk, L. Effect of the damping function in dispersion corrected density functional theory. *J. Comput. Chem.* **32**, 1456–1465 (2011).

75. Weigend, F. & Ahlrichs, R. Balanced basis sets of split valence, triple zeta valence and quadruple zeta valence quality for H to Rn: Design and assessment of accuracy. *Phys. Chem. Chem. Phys.* **7**, 3297–3305 (2005).

76. Weigend, F. Accurate Coulomb-fitting basis sets for H to Rn. *Phys. Chem. Chem. Phys.* **8**, 1057–1065 (2006).

77. Wiegand, I., Hilpert, K. & Hancock, R. E. W. Agar and broth dilution methods to determine the minimal inhibitory concentration (MIC) of antimicrobial substances. *Nat. Protoc.* **3**, 163–175 (2008).

78. Boyce, J. H. et al. Platform to Discover Protease-Activated Antibiotics and Application to

Siderophore–Antibiotic Conjugates. *Journal of the American Chemical Society* vol. 142 21310–21321 (2020).

79. 4″-O-(ω-Quinolylamino-alkylamino)propionyl derivatives of selected macrolides with the activity against the key erythromycin resistant respiratory pathogens. *Bioorg. Med. Chem.* **18**, 6559–6568 (2010).

80. Synthesis, activity and pharmacokinetics of novel antibacterial 15-membered ring macrolones. *Eur. J. Med. Chem.* **46**, 3388–3397 (2011).

81. Wright, A. *et al.* Characterization of the Core Ribosomal Binding Region for the Oxazolidone Family of Antibiotics Using Cryo-EM. ACS *Pharmacol Transl Sci* **3**, 425–432 (2020).

82. Thai Le, S. *et al.* The Very First Modification of Pleuromutilin and Lefamulin by Photoinitiated Radical Addition Reactions-Synthesis and Antibacterial Studies. *Pharmaceutics* **13**, (2021).

83. Paukner, S. & Riedl, R. Pleuromutilins: Potent Drugs for Resistant Bugs-Mode of Action and Resistance. *Cold Spring Harb. Perspect. Med.* **7**, (2017).

84. Yan, K. *et al.* Biochemical characterization of the interactions of the novel pleuromutilin derivative retapamulin with bacterial ribosomes. *Antimicrob. Agents Chemother.* **50**, 3875–3881 (2006).

85. Watkins, R. R. & File, T. M. Lefamulin: A Novel Semisynthetic Pleuromutilin Antibiotic for Community-acquired Bacterial Pneumonia. *Clin. Infect. Dis.* **71**, 2757–2762 (2020).

86. Siricilla, S. *et al.* A New Combination of a Pleuromutilin Derivative and Doxycycline for Treatment of Multidrug-Resistant Acinetobacter baumannii. *J. Med. Chem.* **60**, 2869–2878 (2017).

87. Dong, C.-L. *et al.* Synergistic Effect of Pleuromutilins with Other Antimicrobial Agents against and in an Experimental Model. *Front. Pharmacol.* **8**, 553 (2017).

88. Gürel, G., Blaha, G., Moore, P. B. & Steitz, T. A. U2504 determines the species specificity

of the A-site cleft antibiotics: the structures of tiamulin, homoharringtonine, and bruceantin bound to the ribosome. *J. Mol. Biol.* **389**, 146–156 (2009).

89. Hansen, J. L. *et al.* The structures of four macrolide antibiotics bound to the large ribosomal subunit. *Mol. Cell* **10**, 117–128 (2002).

Publishing Agreement

It is the policy of the University to encourage open access and broad distribution of all theses, dissertations, and manuscripts. The Graduate Division will facilitate the distribution of UCSF theses, dissertations, and manuscripts to the UCSF Library for open access and distribution. UCSF will make such theses, dissertations, and manuscripts accessible to the public and will take reasonable steps to preserve these works in perpetuity.

I hereby grant the non-exclusive, perpetual right to The Regents of the University of California to reproduce, publicly display, distribute, preserve, and publish copies of my thesis, dissertation, or manuscript in any form or media, now existing or later derived, including access online for teaching, research, and public service purposes.

DocuSigned by:

Jenna Pellegrino

8C14AE230E1842F...

Author Signature

8/26/2022

Date